

NANOSTRUCTURAL CHARACTERIZATION  
OF GEOPOLYMERS

by

ATOLO TUINUKUAFE

ARMEN AMIRKHANIAN, COMMITTEE CHAIR

PAUL G. ALLISON

GREGORY B. THOMPSON

JIALAI WANG

MANOJ MAHAPATRA

CHARLES A. WEISS JR.

A DISSERTATION

Submitted in partial fulfillment of the requirements  
for the degree of Doctor of Philosophy  
in the Materials Science Program  
in the Graduate School of  
The University of Alabama

TUSCALOOSA, ALABAMA

2019

Copyright Atolo Tuinukuafe 2019  
ALL RIGHTS RESERVED

## ABSTRACT

Three investigations were conducted in this article-style dissertation, all sharing the common goal of achieving improved characterization of geopolymers in a manner that provides nanostructural information. The first study revisited the use of statistical nanoindentation for characterizing the micromechanical properties of heterogeneous materials and explores the limitations of the method for future applications with geopolymers. In the second investigation, a novel method was developed for quantitatively analyzing the microstructure of geopolymers by using electrical resistivity measurements. The method was found to provide insight into the nanoscale porosity. The third investigation utilized atom probe tomography (APT) to observe the effect of elevated temperature on the nanostructure of a fly ash geopolymer. Complimentary analysis techniques from the first two investigations were used to support the findings from APT. The outcomes of this dissertation are additional insight into the nanostructure of geopolymers, as well as several new characterization tools that may see broader use for other cementitious materials in future research.

## DEDICATION

*To Leilani, Anna-lisia, and JR Tonga,*

*If I've learned anything about statistics, it's that anything is possible.*

## ACKNOWLEDGMENTS

I'm not sure if I remembered what a histogram was when I moved to Tuscaloosa. Seeing as histograms are a motif of this dissertation, I owe many thanks to all of the people who always believed in my abilities to learn and grow. I was blessed to grow up in a family of scientists, teachers, writers and perhaps most importantly a talented chef. The idea of doing research and even getting a Ph.D. was probably planted in my mind a long time ago but Dr. Jacob Henschen was the first to water that seed. Other friends from Valpo who deserve thanks for their support are Dr. Carmine Polito and David Smith. Thanks to Dr. Giannini and Dr. Allison for giving me the opportunity of a lifetime here at UA.

Dr. Armen Amirkhanian must have thought I was lost cause when I almost lit my hand on fire in lab right after he arrived at UA. I'm glad he was willing to at least imagine that I had potential, and help me go to multiple international conferences to present my/our crazy ideas. I will miss entertaining him with all of my formation factor efforts that proved to be futile. This gratitude extends to the rest of my committee as well. Thank you Dr. Weiss for encouraging me to tell a good story. To Dr. Thompson, Dr. Wang, Dr. Allison and even Dr. Mahapatra perhaps; I hope that at least one of you will find at least one of the analysis techniques that I used in my dissertation to be useful in future work. That is the least I could do to thank you all for your support.

This work would not have been possible without the help or insightful feedback of the following graduate students: Tyler Kaub, Rhett, Yi Fang, Mary Kellogg, Matt Fetner, Dallin Barton, Thomas Koenig, and many others. I was always inspired to work harder and longer by my friends in SERC 2024, especially Sumedh Sharma, Farhan Chowdhury, Daniel Valentim, Qifan Nie, Sahar, Shanglian Zhou, Gabi Willis, Kobir, Tu<sup>2</sup>, Shane

Crawford, Visa, Saied Hayati, and the ghost of Stephanie Wood. I was fortunate to have some amazing undergraduate help as well from Jon, Marcelino Diaz, Yixin Liu, Spencer Oldfield, and Kaley Collins. Thanks to Gbenro for taking on the challenge of teaching CE 262 this summer, I would not have finished otherwise.

Dr. Sid Bhattacharya and Dr. Feng Yan were gracious enough to help perform complimentary ICP and AFM tests respectively. Scientists like Marco Sebastiani, Robert Thomas, and Peter Felfer deserve thanks for openly sharing data and information. Thanks to Dr. Ideker for organizing the 2017 Corvallis workshops and short course, where I was introduced to inspirational researchers like Claire White, Doug Hooten, and Karen Scrivener. Many of the ideas in this dissertation may not have been facilitated without that experience.

Thanks to Frederick Jenny for deciding to write a book for fun just so we could continue our friendship in competition. To Jonathan Cappola, I never imagined myself being friends with someone who reads textbooks for fun. Now I find it hard to imagine what my life would have been like without you. The same and much much more can be said for Dr. Ashton Greer who gave me courage and a reason to fight. My other friends in Tuscaloosa: Luke, Averil, Jayla, Jessica, Monica and Kevin Vermillion, Natalie, Daniel Hayes, Alex Robinson, Brandt, the rest of the tri team, and DCBC were essential in preserving my sanity outside of the office/lab. Finally, I have to thank my family in Tonga for their unconditional love and support. Malo au'pito, I wish I could've learned to speak more Tongan instead of MATLAB.

## CONTENTS

ABSTRACT . . . . .	ii
DEDICATION . . . . .	iii
ACKNOWLEDGMENTS . . . . .	iv
LIST OF TABLES . . . . .	ix
LIST OF FIGURES . . . . .	x
CHAPTER 1 PROLOGUE . . . . .	1
CHAPTER 2 REVISITING THE STATISTICAL NANOINDENTATION TECHNIQUE . . . . .	3
2.1 Introduction . . . . .	3
2.1.1 The original method from Constantinides et al. . . . .	4
2.1.2 Critical aspects of indentation mechanics . . . . .	7
2.1.3 Critical aspects of statistical deconvolution . . . . .	15
2.1.4 Summary . . . . .	18
2.2 Methodology . . . . .	19
2.2.1 Statistical analysis of high-speed nanoindentation data . . . . .	19
2.2.2 Evaluating the effect of nanoindentation data filtering . . . . .	21
2.2.3 Phase verification . . . . .	24
2.3 Results . . . . .	25
2.3.1 Clustering of high-speed nanoindentation data . . . . .	25
2.3.2 Clustering of nanoindentation data with filtering for self-similarity . .	30

2.3.3	Clustering of nanoindentation data filtered for self-similarity and structural compliance . . . . .	36
2.3.4	Phase verification . . . . .	40
2.4	Discussion . . . . .	44
2.4.1	Li <sub>x</sub> Mn <sub>2</sub> O <sub>4</sub> -based cathode materials . . . . .	44
2.4.2	Al-Si ceramics . . . . .	45
2.4.3	Ordinary portland cement . . . . .	48
2.5	Conclusions . . . . .	51
CHAPTER 3 QUALITY ASSESSMENT OF GEOPOLYMERS USING THE FORMATION FACTOR . . . . .		53
3.1	Introduction . . . . .	53
3.2	Methodology . . . . .	56
3.2.1	Specimen preparation . . . . .	56
3.2.2	Measuring free alkalinity . . . . .	57
3.2.3	Measuring formation factor . . . . .	60
3.2.4	Complimentary characterization . . . . .	64
3.3	Results and Discussion . . . . .	65
3.3.1	Free alkali measurement . . . . .	65
3.3.2	Formation factor measurement . . . . .	70
3.3.3	Complimentary characterization . . . . .	73
3.4	Conclusions . . . . .	80
CHAPTER 4 THE EFFECT OF ELEVATED TEMPERATURE ON THE NANOSTRUCTURE OF A FLY ASH GEOPOLYMER . . . . .		81
4.1	Introduction . . . . .	81
4.1.1	Geopolymer molecular structure . . . . .	81
4.1.2	Atom probe tomography . . . . .	83

4.2	Methodology . . . . .	84
4.2.1	Atom probe tomography . . . . .	85
4.2.2	Free alkalinity . . . . .	85
4.2.3	Nanoindentation . . . . .	86
4.3	Results and Discussion . . . . .	87
4.3.1	Atom probe tomography . . . . .	87
4.3.2	Free alkalinity . . . . .	99
4.3.3	Nanoindentation . . . . .	102
4.4	Conclusions . . . . .	109
	CHAPTER 5 EPILOGUE . . . . .	110
	REFERENCES . . . . .	111
	APPENDIX A CODE FOR INDENTATION DATA ANALYSIS . . . . .	123
	APPENDIX B GRID INDENTATION REGIONS OF FLY ASH GEOPOLYMER SAMPLES . . . . .	140

## LIST OF TABLES

2.1	Symbology used in statistical algorithms after [16] . . . . .	5
2.2	Type I/II cement composition from XRF . . . . .	22
2.3	Grid indentation preprocessing filter efficiencies . . . . .	30
2.4	Summary of filtered CSM nanoindentation data deconvolution using belief-based clustering. . . . .	36
2.5	Summary of high speed nanoindentation data deconvolution using belief-based clustering. . . . .	36
3.1	Mixture compositions by weight fraction of constituents. . . . .	56
3.2	Metakaolin composition from manufacturer. . . . .	57
3.3	Composition of silicate solutions. . . . .	57
3.4	Summary of data from formation factor calculation. . . . .	71
4.1	Oxide composition of Bowen fly ash from XRF. . . . .	84
4.2	Count of ranged ions in each APT sample run with multi-atomic ions decomposed. . . . .	99
4.3	Summary of FGP nanoindentation data deconvolution. . . . .	103

## LIST OF FIGURES

2.1	Effect of surface roughness on indentation. . . . .	8
2.2	Sources of structural compliance, after Jakes et al. . . . .	9
2.3	Cases where the continuum analysis is valid or invalid. . . . .	11
2.4	Example of a self-similar indent with additional sources of structural compliance. . . . .	20
2.5	Example of a dissimilar test with a high coefficient of determination. . . . .	23
2.6	Flowchart of CSM grid indentation data processing. . . . .	24
2.7	GMM selection and cluster assignments for the high-speed indented 0% SoC sample. . . . .	27
2.8	GMM selection and cluster assignments for the high-speed indented 100% SoC sample. . . . .	28
2.9	GMM selection and cluster assignments for the high-speed indented OPC 0.36 sample. . . . .	29
2.10	Representative AFM scans of Al-Si samples . . . . .	31
2.11	GMM selection and cluster assignments for the Al-Si 9:1 after filter 1. . . . .	33
2.12	GMM selection and cluster assignments for Al-Si 2:1 sample after filter 1. . . . .	34
2.13	GMM selection and cluster assignments for OPC 0.5 after filter 1. . . . .	35
2.14	GMM selection and cluster assignments for Al-Si 9:1 sample after filter 2 . . . . .	37
2.15	GMM selection and cluster assignments for Al-Si 2:1 sample after filter 2 . . . . .	38
2.16	GMM selection and cluster assignments for OPC 0.5 after filter 2 . . . . .	39
2.17	SEM-EDS analysis of Al-Si 9:1 sample. . . . .	41
2.18	SEM-EDS analysis of Al-Si 2:1 sample. . . . .	42

2.19	CEMHYD3D model output for OPC 0.36 sample . . . . .	43
2.20	CEMHYD3D model output for OPC 0.5 sample . . . . .	43
3.1	Illustration of formation factor components for a saturated porous microstructure. . . . .	54
3.2	Isothermal calorimetry of Na and K mixtures at 20°C . . . . .	57
3.3	Setup for measuring the effective bulk resistivity. . . . .	61
3.4	Schematic of the method used to account for alkali leaching. . . . .	62
3.5	Comparison of pore solution conductivity calculation methods . . . . .	64
3.6	Comparison of water and ethylene glycol as solvents for alkali leaching at various temperatures. . . . .	66
3.7	Free alkali measured for different volumes of water as a solvent. . . . .	67
3.8	Free alkali measurement with different particle sizes and leaching durations. .	68
3.9	Comparison of ICP-OES and titration measurements of free alkalis using GP HWE and espresso methods. . . . .	69
3.10	Trace elements quantified by ICP-OES for GP HWE and espresso leaching methods. . . . .	70
3.11	Free alkali content of geopolymers as determined by the espresso method. . .	71
3.12	Formation factor measurements for fully saturated geopolymer pastes. . . . .	72
3.13	Formation factors calculated without accounting for alkali leaching during saturation and storage. . . . .	73
3.14	UPV measurements for in-situ geopolymer samples. . . . .	74
3.15	SEM micrographs of geopolymer fracture surfaces at 1,000x magnification. .	75
3.16	SEM micrographs of geopolymer fracture surfaces at 10,000x magnification. .	76
3.17	SEM micrographs of geopolymer fracture surfaces at 100,000x magnification.	78
3.18	Histograms of the equivalent diameter of 50 particles in each image. . . . .	78
3.19	High magnification SEM comparison of Na and K geopolymers. . . . .	79
4.1	Schematic illustration Na-geopolymer molecular framework from [73] . . . . .	82

4.2	Schematic illustration of atom probe tomography technique (www.cameca.com). . . . .	84
4.3	Mass spectra of unheated APT sample runs. . . . .	89
4.4	Mass spectra of heated APT sample runs. . . . .	90
4.5	Histograms of K and Al concentrations throughout samples with a 3 nm voxel size. . . . .	92
4.6	Cluster analysis of potassium in unheated samples. . . . .	93
4.7	Cluster analysis of potassium in unheated samples. . . . .	94
4.8	Cluster analysis of potassium in heated samples. . . . .	96
4.9	Histograms of K and Al concentrations throughout samples with a 3 nm voxel size. . . . .	98
4.10	Histograms of K and Al concentrations throughout samples with a 3 nm voxel size. . . . .	98
4.11	Free alkali content of the FGP after various temperature exposures. . . . .	101
4.12	Grid indentation data analysis for the as-cast FGP sample. . . . .	104
4.13	Grid indentation data analysis for FGP heated at 200° for 2 hrs. . . . .	105
4.14	Grid indentation data analysis for FGP exposed to flame for 10 minutes as in [71], reaching 650°. . . . .	106
4.15	Indentation data for randomly selected tests from Cluster 1 (i.e. reacted phase) of each sample. . . . .	107
B.1	Grid indentation region of unheated FGP. . . . .	140
B.2	Grid indentation region of 200°C heated FGP. . . . .	141
B.3	Grid indentation region of flame heated FGP. . . . .	141

## **CHAPTER 1**

### **PROLOGUE**

This dissertation is comprised of three studies investigating the use of both new and existing characterization techniques for geopolymer cements. Geopolymer cements are an appealing alternative to ordinary portland cement (OPC) because of their potential to reduce greenhouse gas emissions, improved fire-resistance, and advantages for other niche applications. By furthering the understanding of geopolymers, their suitability for industry applications can be better assessed.

In the first study of this body of work, the use of statistical nanoindentation is revisited. The validity and limitations of the technique are investigated using an assortment of composite materials other than geopolymers. From this work, a more reliable method for later use with geopolymers may be identified.

The second investigation seeks to develop a convenient method for quantitative evaluation of geopolymer microstructures using electrical resistivity measurements. In the process of this investigation, a suitable method for quantifying the free alkali content of geopolymers is also pursued. The resulting experimental framework may be a more informative and economical alternative to electron microscopy for comparing geopolymer microstructures. This method could have future potential as a quality control method for geopolymer cement applications.

The final study examines the novel use of atom probe tomography (APT) for geopolymers before and after heat exposure. Statistical nanoindentation is employed as a complimentary technique here, using the insights from the first investigation to improve

the validity of the method. The method for measuring free alkalis proposed in the second study is also used here to support the APT results. The outcome of this study is an enhanced understanding of the nanostructural role of alkalis in geopolymers.

In addition to advancing the knowledge of geopolymer systems, the characterization of geopolymers in this work may provide insight into how the characterization techniques themselves can be improved for more reliable use with other materials with highly heterogeneous microstructures, such as other cementitious systems.

## CHAPTER 2

### REVISITING THE STATISTICAL NANOINDENTATION TECHNIQUE

#### 2.1 Introduction

Nanoindentation allows for the micromechanical properties of materials to be measured through indentation performed at a sub-micron level. This small scale investigation technique is very appealing for materials with heterogeneous microstructures as means of evaluating the properties of individual phases of the microstructure. By doing so for all of the microstructure constituents, an improved multi-scale mechanical understanding of the material can be established [16].

Data from a single indent test can provide the elastic modulus ( $E$ ) and hardness ( $H$ ) of the material based on the most commonly used Oliver and Pharr calculations (Eq. 2.1 and 2.2) [63]

$$H = \frac{L_{\max}}{A} \quad (2.1)$$

$$E = \frac{\sqrt{\pi}}{2} \frac{S}{\sqrt{A}} \quad (2.2)$$

where  $L_{\max}$  is the maximum load,  $A$  is the contact area at the point of loading, and  $S$  is the initial unloading stiffness. However, these equations were developed under the assumption of a bulk homogeneous and isotropic material as a continuum analysis.

To examine the entire microstructure of a heterogeneous material, large arrays or grids of indents are performed. Grid indentation enables the mapping of micromechanical properties as a qualitative analysis [55, 106]. For quantitative analysis of grid indentation,

a statistical nanoindentation method was proposed by Constantinides et al. [16, 17] to distinguish the individual phases probed by grid indentation.

The original statistical analysis, which is fully reviewed in the following section 2.1.1, fits a theoretical probability density function to the experimental data with component Gaussians representing each phase. The mean, standard deviation, and volumes of the assigned Gaussians are assumed to quantify the different phases. Constantinides et al. proposed that this method “circumvents” the interaction between phases in the microstructure and that the continuum analysis is applicable when a small enough indent depth is used [16]. These critical assumptions are revisited in this introduction and experimental work. Other researchers have investigated critical aspects of Constantinides’ original statistical nanoindentation, but have focused more specifically on the application of the method for cementitious materials [23, 37, 49, 59, 90].

### **2.1.1 The original method from Constantinides et al.**

Regarding the individual indentation technique, Constantinides et al. refer to the analogy of thin-film materials where substantial literature on nanoindentation was available. Although more recent literature regarding the influence of a substrate material with different mechanical properties was discussed, the authors concluded that the 1/10th approximation originally proposed Buckle (simply stating that indent depths should be less than 1/10th of the thin-film thickness in order to avoid substrate influence [13]) was sufficient enough to apply the continuum indentation analysis to more complex heterogeneous materials [16].

The variable assignments used by Constantinides et al. and repeated here are listed in Table 2.1 for reference. Assuming that  $h \ll D$  satisfies the criteria for the continuum analysis to be applied to a single indentation test, with a homogeneous representative volume element (RVE, i.e. volume of influence in the material) to satisfy self-similarity, statistical nanoindentation can be performed as follows by [16]:  $N$  indentation tests are conducted in a large grid format on the sample with spacing  $l$ , where  $l\sqrt{N} \gg D$  to avoid

Table 2.1: Symbology used in statistical algorithms after [16]

Symbol	Definition
RVE	representative volume element, or volume of influence for the indent test
$h$	indentation depth
$a$	indenter tip radius
$D$	characteristic microstructural feature length scale
$d$	characteristic size of the largest heterogeneity within the RVE
$J$	phase number
$n$	number of phases
$N$	number of indentation tests in grid
$N_J$	number of indentations on material phase $J$
$f_J$	frequency of a mechanically distinct phase, $J$ , tested in the grid
$x$	the selected mechanical property, elastic modulus $M$ or hardness $H$ , of a given indent
$p_J(x)$	assumed Gaussian distribution of $x$ for phase $J$
$u_J$	mean $x$ for phase $J$ according to the assigned Gaussian
$s_J$	standard deviation of $x$ for phase $J$ according to the assigned Gaussian
$P(x)$	theoretical probability density function for $x$ across the sample
$P_i$	discrete indentation values
$m$	number of bins used to construct a histogram
$x_i$	mechanical property value for a given bin, $i$

statistical bias of phases. For the large grid of  $N$  indentation tests, the frequency of each phase in the microstructure,  $f_J$ , is:

$$f_J = \frac{N_J}{N}, \quad \text{where} \quad \sum_{J=1}^n N_J = N \quad (2.3)$$

The distribution of  $x$  for each phase is assumed to be a normal or Gaussian distribution:

$$p_J(x) = \frac{1}{\sqrt{2\pi s_J^2}} \exp -\frac{(x - \mu_J)^2}{2s_J^2} \quad (2.4)$$

Where the mean and standard deviation for each phase is given by:

$$\mu_J = \frac{1}{N_J} \sum_{k=1}^{N_J} x_k \quad (2.5)$$

$$s_J^2 = \frac{1}{N_J - 1} \sum_{k=1}^{N_J} (x_k - \mu_J)^2 \quad (2.6)$$

For a homogeneous single phase material,  $n = 1$ ,  $\mu_J$ , and  $s_J^2$  accurately describe the

material properties in a statistical sense. However, when the assignment of normal distributions is extended to multiple phases,  $J = 1 : n$ , it must be assumed that the phases do not interact mechanically [16]. Constantinides et al. then propose that the overall frequency distribution for the mechanical property  $x$  can be described by the following theoretical probability density function (PDF):

$$P(x) = \sum_{J=1}^n f_J p_J(x), \quad \text{where} \quad \sum_{J=1}^n f_J = 1 \quad (2.7)$$

In equation 2.7 above,  $f_J$ ,  $\mu_J$ , and  $s_J$  must be solved for, which leaves  $3n - 1$  unknowns. The equation (2.7) can be determined through a process of minimizing the mean square error (MSE) between the experimental data and the theoretical PDF  $P(x_i)$ . The discrete experimental observations  $P^i$  are essentially assembled into a histogram with an assigned number of bins  $m$ . The following function essentially fits the theoretical PDF (Eq. 2.7) to the experimental histogram:

$$\min \text{MSE} = \sum_{i=1}^m \frac{(P^i - P(x_i))^2}{m} \quad (2.8)$$

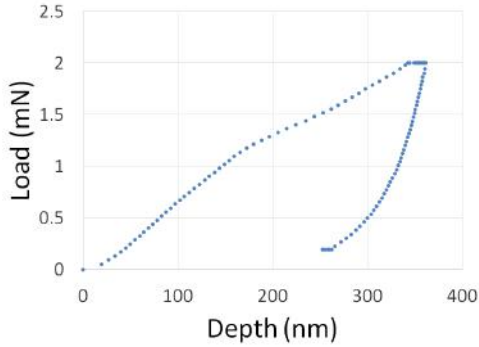
Using this deconvolution algorithm, the number of phases  $n$  must be known or assumed, often with the aid of X-ray diffraction or microscopy. The advantage of using a cumulative distribution function (CDF) instead of a PDF here is that no bin width needs to be assigned [76, 93], though this does not eliminate any “noise” from the data [49] and eliminates the inherent low-pass filtering aspect of using the PDF. In the original statistical nanoindentation method revisited here, the locally optimum solution for Eq. 2.8 was manually selected [49], though this was not explicitly stated in [16].

## 2.1.2 Critical aspects of indentation mechanics

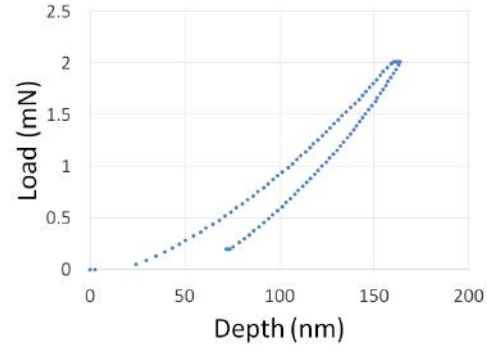
### Surface roughness

The ASTM E2546-15 [28] specification for instrumented indentation states the specimen surface finish and flatness is critical for reliable test results, however no surface roughness criteria are provided. With respect to statistical nanoindentation of portland cement (often referred to as ordinary portland cement, OPC), Miller et al. proposed that the minimum indentation depth,  $h$ , should be at least five times greater than the root-mean-squared (RMS) surface roughness measured using atomic force microscopy (AFM) over a scan area equal to  $200h^2$  [51]. Because hydrated portland cement is inherently porous, Ttrik et al. questioned the feasibility of the Miller's surface roughness criteria and hypothesized that it is only attained through Miller's extensive polishing procedure where particles from the specimen are possibly removed then repacked into the porosity of the material to yield an ultimately flatter surface [90].

Regardless of the measured surface roughness or polishing procedure, insufficient surface flatness will cause aberrant test results, which will generally be apparent in the load-displacement plot. An example of this is shown in Fig. 2.1a. Considering the porous nature of some materials, such as cementitious materials, there will inevitably be aberrant tests pertaining to porous regions or areas sloping towards a porous region so the surface should be prepared in a way that generally minimizes the aberrant tests as suggested by ASTM E2546-15 [28] while not disturbing the natural microstructure of the material. With the assumption that aberrant tests due to surface roughness or porosity are discarded prior to mapping or statistical analysis of the results, one can assume that it generally does not influence the processed results and simply reduces the number of valid test results. With better surface preparation, the amount of useful data obtained from grid indentation is increased and in effect increases the sample size,  $N$ , without additional tests.



(a) Example of an aberrant test in a sample with poor surface flatness.



(b) Example of a valid test in a flat surface.

Figure 2.1: Effect of surface roughness on indentation.

### Influence of microstructure

Considering the highly heterogeneous microstructure of portland cement systems again, Trtik, Lura, and Münch used focused ion beam nanotomography (FIB-nt) to make the argument that there is generally not a homogenous interaction volume present for nanoindentation [49, 90]. In defense of their proposed nanoindentation technique, Ulm et al. argued that there are sufficiently homogeneous regions of cement microstructure and that Buckle’s rule of thumb for phase separability holds true [94]. Both research groups refer to microscopy to support their argument and therefore either argument may be correct in different scenarios where the microscopy is representative of the indented microstructure. However, there is sufficient evidence from scanning electron microscopes (SEM) X-ray energy dispersive spectroscopy (EDS) to conclude that nanoparticulate heterogeneity can be present in the RVE of indents in OPC [14, 37]. This phenomena does not explain why statistical nanoindentation can result in a ”noisy” and widespread experimental distribution for more homogeneous composite phases though, such as the Ti/TiB composite in the validation experiments from [16] (e.g. see Fig. 7c of [16]).

For a more complete understanding, other mechanisms of microstructural influence should be considered besides a heterogeneous RVE. There are several microstructural scenarios where the assumptions made by Oliver and Pharr’s continuum analysis and that

set forth by ASTM E2546-15 are invalid due to an additional source of structural compliance, as discussed by Jakes et al. [39].

The departures from the continuum analysis noted by Jakes et al. include: flexure on the indent scale, which was observed for the cell structure of wood based specimens (Fig. 2.2a), indents near a phase boundary or edge (Fig. 2.2b), or a layered specimen (Fig. 2.2c). As discussed previously, Constantinides et al. did acknowledge the possibility of substrate effects preventing the isolation of obtaining individual phase properties by applying Buckle’s rule of thumb. While this assumption may be true sometimes in heterogeneous composites, the authors acknowledged that it will inevitably fail in some instances [16]. The question then remains — when is the continuum analysis valid for indentation of a heterogeneous microstructure?

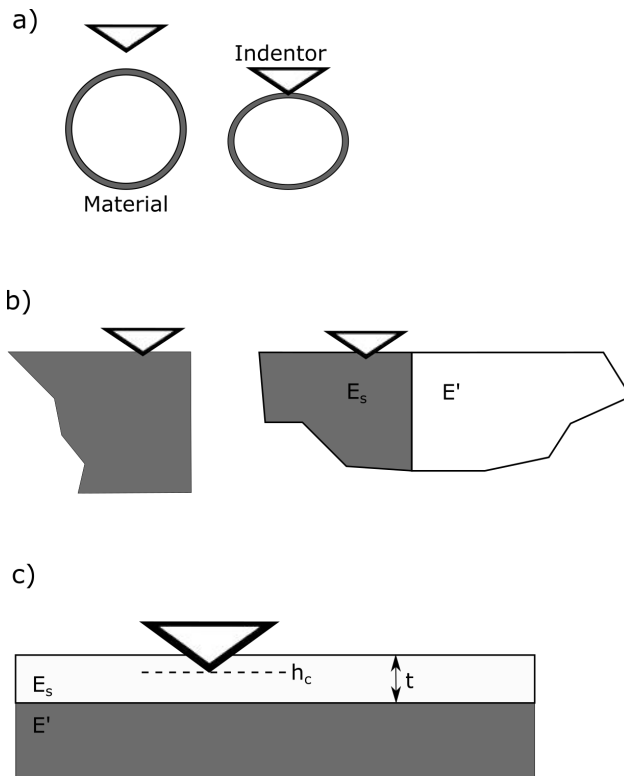


Figure 2.2: Sources of structural compliance, after Jakes et al. [39] a) Elastic structural deformation on the specimen scale. b) Elastic heterogeneity due to a free edge (left) or dissimilar neighboring material (right). c) Layers with heterogeneous properties.

To answer this question, the scenarios are considered where there will be additional

structural compliance and the continuum analysis will not be valid (excluding the possibility of a flexible material). A more recent examination of superhard thin film coatings ( $H > 80$  GPa) on various substrates found that Buckle's rule was not applicable with a far weaker substrate [97]. This finding could be interpreted to also suggest that Buckle's rule does not apply when the substrate happens to be a porous region or void, which is certainly a possibility in cement microstructure.

Following this logic, there are two sources of structural compliance not addressed by the use of Buckle's rule. These sources are present for indents in horizontal proximity of a phase boundary or pore space (Fig. 2.3a and b) and indents with underlying porosity (Fig. 2.3c). The discarded indents into porosity may also place a bias in the distribution of neighboring phases or more porous phases such as ettringite in OPC.

In spite of any assumptions, an indent with a substrate influence is always a possibility in heterogeneous microstructures. The probabilities of the microstructural influences on indents discussed in this section and depicted in Fig. 2.3 and 2.2, likely increase with the level of complexity or scale of heterogeneity in the microstructure. Furthermore, a heterogeneous RVE that other researchers have identified as a potential issue, particularly for OPC [23, 37, 49, 90], is still plausible.

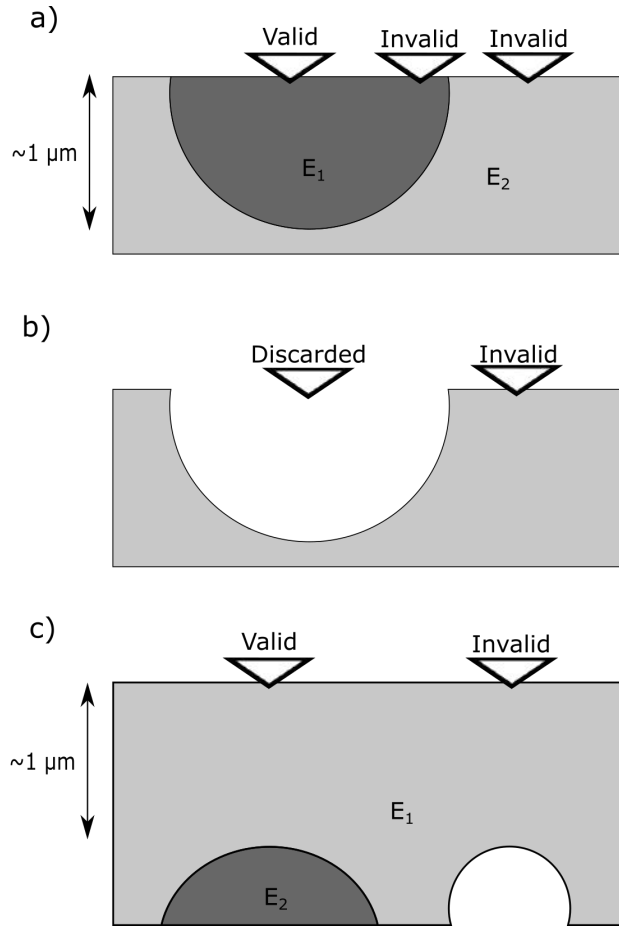


Figure 2.3: Cases where the continuum analysis is valid or invalid: a) valid case within at least a  $1\mu\text{m}^3$  volume but invalid cases near either side of the phase boundary, b) discarded or aborted indent test within a pore and an invalid test near the edge, c) valid indent in media at least  $1\mu\text{m}$  above a boundary with a phase of comparable modulus and the invalid case for an indent above a pore space even if it is separated by at least  $1\mu\text{m}$  from the surface. This example considers an indent depth of 100 nm

## Indentation method

Typically, basic indents with 0.5-2mN load control are performed with a trapezoidal loading sequence [18, 93] in order to achieve the appropriately small indent depth. The appropriate load for a material can be determined through a trial and error process to obtain the desired depth [18]. For composite materials, this method will yield different depths of indentation  $h$  for different phases  $N_J$ . There is, however, another indentation method that achieves a continuous stiffness measurement (CSM) by oscillating the tip

during the loading phase, rather than only measuring the stiffness upon unloading as in the basic method.

For the basic indentation method, self-similarity principles are employed exclusively to judge the quality of indents by checking for a linear trend in the plot of load versus  $h^2$ , or the presence of a quadratic trend in the load-displacement plot [15]. This approach can identify fractures (or “pop-in” events) or surface roughness effects, but it does not consider additional sources of structural compliance. The discrepancy here lies in the equation used to calculate the depth (Eq. 2.9) which relies on the stiffness upon unloading.

$$h = h_{\max} - 0.75 \frac{L_{\max}}{S} \quad (2.9)$$

Eq. 2.9 essentially assumes that there is a constant stiffness of the material across the entire indentation so that the depth can be interpolated as a function of the load. As discussed in the previous section, this is not always the case for indents in heterogeneous composites. Therefore, the self similarity approach proposed in the original statistical nanoindentation method cannot be used to confirm whether the continuum analysis applies since it relies on equivalent assumptions. Considering that researchers have continued to use the basic indentation method for statistical nanoindentation [38, 48, 102], it has yet to be shown whether this fundamental oversight is an issue.

When the continuum analysis is assumed based on self similarity, the resulting E and H values are liable to be influenced in cases where Buckle’s rule is violated, an inevitability as stated by Constantinides et al. [16], or when any of the other sources of structural compliance (Fig. 2.3 and 2.2). As early as 1999, Knapp et al. had used finite element modeling and CSM indentation to provide data demonstrating that the substrate can influence the modulus determination from basic indentation of thin films even though self similarity is preserved (see fig. 10 and 11 in [41]). Considering that there was ample literature using the CSM indentation method released prior to the inception of statistical

nanoindentation [44], it is a point of curiosity as to why the CSM technique was not originally considered for statistical nanoindentation.

The erroneous tests obtained during grid indentation due to additional sources of structural compliance could easily be identified by using the CSM technique, or simply performing multiple loading cycles, to obtain stiffness measurements at different indentation depths [39]. In 1991, Stone, Yoder and Sproul (SYS) [85] used CSM to derive an alternative method for determining the mechanical properties of thin films, which yielded consistent results for thin films regardless of thickness. Their method effectively circumvented the need to assume Buckle’s rule. Based on the work of SYS, Jakes et al. derived the following equation to account for structural compliance.

$$\frac{L^{1/2}}{S} = (C_m + C_s)L^{1/2} + J_O^{1/2} \quad (2.10)$$

Where  $C_m$  and  $C_s$  are the machine and structure compliance respectively and  $J_O$  is the Joslin-Oliver parameter [40] defined by,

$$J_O = \frac{H}{E_{\text{eff}}^2} \quad (2.11)$$

When no indentation size effect is present,  $J_O$  can be determined as the intercept from a so-called “SYS plot” of  $L^{1/2}/S$  vs.  $L^{1/2}$  on the x-axis. In this plot, the slope represents the combined compliance, and the intercept defines  $J_O$ . Fig. 2.4 shows an example of a CSM indentation subject to additional structural compliance (taken from the Al-Si 9:1 dataset presented in the body of this work). The indent satisfies self-similarity (Fig. 2.4), but the shallower depths of indentation appear to be affected by a substrate or edge influence.

Jakes et al. were able to correct for edge effects in timber microstructures by using this relationship. Using this approach for composite materials is difficult, however, since substrate constituents may themselves be subject to additional structural compliance.

Therefore, only indents with minimal structural compliance should be used in the analysis [3]. Another drawback of the SYS correction for compliance when considering extensive grid indentation is the need to determine the contact area of each indent *a posteriori* via microscopy.

Even though corrected values for the mechanical properties of an indent containing additional structural compliance cannot readily be obtained, the SYS plot provides a method of assessment. Amanieu et al. were able to use the SYS plot as a filtering method for statistical nanoindentation of two phase materials [3]. Prior to filtering, they observed a significant scatter of indents in between the two phases in the experimental PDFs. After filtering, however, distinct peaks in the PDF are apparent for the two phases [3].

While filtering based on the SYS plot could be readily automated, the same results could also be attainable simply by examining the CSM data in a plot of stiffness-depth. This would also extend to the plots of modulus or hardness-depth since they depend on stiffness. In fact, Das et al. used the CSM technique for statistical nanoindentation of an alkali-activated fly ash (AAFA) cement and used the plot of modulus vs. depth to assess indentation quality [21]. Their resulting PDF displayed four distinct peaks corresponding to different phases. The potential of using CSM as a filtering method is especially appealing when the variability of the AAFA material is considered. Das et al. were still able to show arguably clearer peaks in the PDF than Constantinides et al. did for a considerably less complex or variable Ti composite material using their proposed basic indentation method.

Several notable technological advancements in nanoindentation methods have been made since statistical nanoindentation was introduced. Nanoindentation equipment is now available with a dynamic contact module (DCM) loading apparatus. The DCM offers a higher resolution of force measurement, but sacrifices the ability to perform higher indentation loads. This is preferable for thin-film materials, as well as composites with limited regions of heterogeneity that are often the subject for statistical nanoindentation.

The DCM technology also enables high-speed or “express” indentation testing to be performed. With this method indents to low depths (i.e. 100 nm) can be performed in one second. This technique has been used to provide high resolution mapping of mechanical properties of various materials, and it has also provided dramatically increased sample sizes for statistical nanoindentation [36, 56, 76]. It should be noted that in spite of the higher resolution modulus maps produced using high-speed indentation, clear phase boundaries are not shown where there are distinct boundaries in the corresponding microscopy [36, 56, 76]. This is likely due to an artifact of structural compliance near edges where phases interact, as described in section 2.1.2. Reiterating section 2.1.1, the statistical nanoindentation procedure assumes that there is no interaction between phases and thus high speed indentation may provide limited benefits to statistical nanoindentation (even when spacing requirements are met)[16].

SEM-EDS has also become more readily available since the conception of statistical nanoindentation. Many authors have coupled grid indentation with SEM-EDS mapping for qualitative chemical analysis of the corresponding phases in the microstructure [37, 55, 106]. It was not until recently that grid indents were quantitatively correlated to chemistry via automated SEM-EDS spot scans of every indent in a grid [102]. While this procedure is incredibly useful for designating indented phases and eliminating indents from potentially impure phases, the measured mechanical properties of “pure” phases could still be influenced by the microstructural effects discussed in section 2.1.2.

### **2.1.3 Critical aspects of statistical deconvolution**

In a recent review, Luo et al. concluded that statistical nanoindentation involved “questionable statistical analysis methods” [48], broadly referring to the method proposed by Constantinides et al. [16] discussed in section 2.1.1. Regarding OPC, Lura et al. demonstrated the numerical instability of curve fitting by minimizing MSE following Eq. 2.8, which resulted in the manual selection of a locally optimum solution that may not be the global optimum [49]. Considering the global optimum is unobtainable in a reasonable

amount of time and that there is no clear method for determining which local optimum to select, the method is qualitative at best and an alternative deconvolution algorithm is desirable.

While the curve fitting approach converges towards the elusive “best-fit”, the alternative maximum likelihood approach attempts to calculate the most probable or likely Gaussian mixture model (GMM) [31]. The likelihood of the GMM (analogous to the theoretical PDF in the original method) is often expressed in log form, as shown in Eq. 2.12. The likelihood is increased through  $q$  iterations of Expectation Maximization (EM) until there is minimal improvement in likelihood and the solution has effectively converged.

$$l = \sum_{k=1}^N \log\left(\sum_{J=1}^n f_J P(x_k)\right) \quad (2.12)$$

The expectation or E-step of EM can be summarize by Eq. 2.13, where a responsibility value  $r_{kJ}$  is calculated. The responsibility  $r_{kJ}$  essentially represents the probability that a given indentation datum  $x$  belongs to a given phase  $J$ , which is still assumed to have a Gaussian distribution as in the original method. The mean,  $\mu_J$ , and covariance,  $\sum_J$ , of  $p_J(x)$  are fixed during the E-step.

$$r_{kJ} = \frac{f_J p_J(x_k | \mu_J, \sum_J)}{\sum_{J=1}^n f_J p_J(x_k | \mu_J, \sum_J)} \quad (2.13)$$

The maximization of M-step of EM uses the  $r_{kJ}$  values to update the assigned phase distributions described by  $N_J$ ,  $\mu_J$ , and  $\sum_J$ . For the 1-D scenario considered in the body of this study,  $\sum_J$  is equivalent to the variance.  $\sum_J$  describes an ellipsoid for 2-D cases [31, 102].

$$N_J = \sum_{k=1}^N r_{kJ} \quad (2.14)$$

$$f_J = \frac{N_J}{N} \quad (2.15)$$

$$\mu_J = \frac{\sum_{k=1}^N r_{kJ} x_k}{N_J} \quad (2.16)$$

$$\sum_J = \sum_{k=1}^N r_{kJ} (x_k - \mu_J)^\top (x_k - \mu_J) \quad (2.17)$$

The apparent issues with this approach are the assumed number of phases,  $J$ , and the possibility of “over-fitting” or converging on a solution that is more probable than can be reasonably accepted based on the sample size  $N$  [31]. To address these issues, the Bayesian Information Criterion (BIC)[74] can be maximized instead of log-likelihood to determine the best model by accounting for  $N$  and repeating the EM procedure for different numbers of phases  $J$  and selecting the value of  $J$  that results in the lowest BIC.

$$\text{BIC} = 2l + n \log N \quad (2.18)$$

This maximum likelihood approach to deconvolution with the constraints of the BIC has been successfully applied to statistical nanoindentation of cementitious materials to obtain consistent results without user bias [37, 88, 102]. The equations presented so far can be expanded for multivariate analysis even though only the univariate forms are shown here for simplicity. Although this method enables consistent solutions to be obtained, it is Bayesian in nature and the assigned phases are inherently probabilistic as “soft” cluster assignments rather than classifications since no prior information is provided (i.e. flat prior, unsupervised model) [10, 31]. The more accurate terminology for this approach to statistical deconvolution could be belief-based clustering since it better describes the Bayesian nature of this method in that the probability of the statistical accuracy of clusters (i.e. phases) is now being determined [10], instead of “fitting” an estimated statistical distribution to the data as in the original algorithms.

If the number of phases,  $N_J$ , and mean,  $\mu_J$ , of each were known a priori, then more reliable semi-supervised clustering could be performed. The prior knowledge would allow the clustering algorithm to place less weight on spurious indents not pertaining to the

known indents. However, prior knowledge is rarely available, leaving the possibility that erroneous indents due to microstructural influences discussed in section 2.1.2 could effectively convolute the deconvolution. As mentioned earlier, Wilson et al. used quantitative SEM-EDS to construct multivariate models for cementitious materials, effectively informing the Gaussian mixture model with chemical labeling for each phase [102]. Alternatively, ensuring that only indents of valid continuity are input to the statistical analysis could also allow the unsupervised belief-based clustering method to be used reliably.

#### 2.1.4 Summary

Researchers have previously expressed concerns about aspects of statistical nanoindentation such as surface roughness, prolific heterogeneity contaminating the RVE (e.g. OPC [38, 48, 102]), “noisy” data, or the statistical methods themselves [48]. It seems intuitive that larger sample sizes would provide a better signal to noise ratio [49] and potentially improve the technique. The overarching theme in the literature, however, is the vastly overlooked assumption that the continuum analysis applies to indents in a heterogeneous microstructure without interaction of phases.

In this study, data from high speed nanoindentation are used with the improved statistical analysis (belief-based clustering) to investigate the role of sample size. In contrast, the influence of microstructure is investigated by using DCM-CSM indentation and filtering prior to statistical analysis to ensure that the continuum analysis is valid, similar to the method demonstrated by Amanieu et al [3]. However, Amanieu et al. also suggested that larger sample sizes would increase signal to noise. This is true if filtering for continuity is still performed, but the stiffness at multiple depths of indentation has not yet been in a high-speed method. The present study investigates whether the limiting factor for statistical nanoindentation is not the sample size,  $N$ , but rather the fundamental assumption that each indentation exhibits continuity. By exploring the limitations of the assumptions made in the statistical nanoindentation method, it may be reconciled for

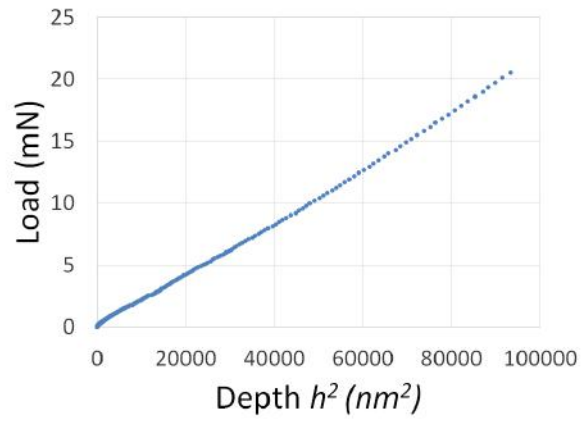
select applications.

## 2.2 Methodology

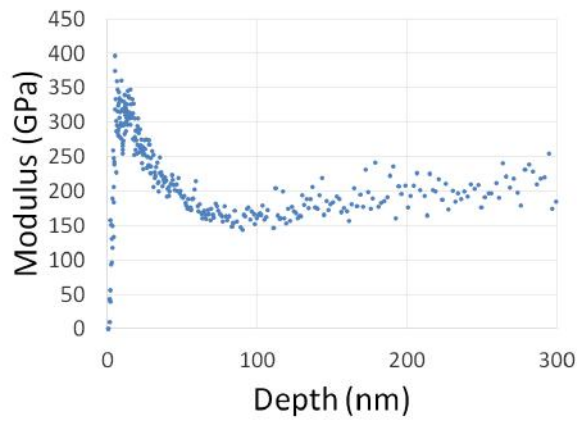
### 2.2.1 Statistical analysis of high-speed nanoindentation data

The high speed nanoindentation method performs one indent per second to a depth of 100 nm and uses the basic load vs. displacement curve to determine the modulus and hardness from the continuum analysis [36, 56, 63, 76]. In this section, high speed nanoindentation from [56, 57, 76] were re-analyzed using belief-based clustering to determine GMMs for the reported modulus values. The BIC for model orders (i.e. number of phases  $J$ ) 1-5 were calculated, and clustering was performed for the model with the lowest BIC. The Matlab program used to perform the clustering is included in the appendix.

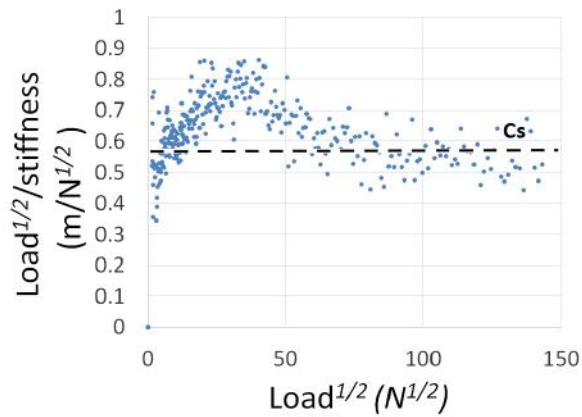
The first two datasets were originally obtained from  $\text{Li}_x\text{Mn}_2\text{O}_4$ -based cathode materials at different states of charge (SoC). The grid indentation yielded 817 and 861 successful indents (out of 900) for 0% and 100% SoC samples respectively. Successful indents are defined here as tests that were not automatically aborted for any reason, e.g. porosity. Testing was completed in less than an hour using an indent spacing of 2 microns [57]. The third dataset was obtained from 15 separate 50x50 indentation grids performed on an OPC sample ( $w/c = 36$ ) also using 2 micron spacing [76]. For this sample, 33,134 successful tests were provided from the 37,500 total tests performed.



(a) Plot confirming self-similarity of the indent



(b) Modulus across depth of CSM indentation



(c) SYS plot with a dashed line indicating a level compliance

Figure 2.4: Example of a self-similar indent with additional sources of structural compliance.

## 2.2.2 Evaluating the effect of nanoindentation data filtering

### Sample preparation

Alumina-silica (Al-Si) composites of 9:1 and 2:1 mass fractions were made by sintering compacted powder pellets of 9 mm diameter and 3 mm thickness. The powders used were commercially available with the  $\text{Al}_2\text{O}_3$  powder (source: Allied High Tech Products, Rancho Dominguez, CA) of an average particle size of  $1\mu\text{m}$  and the  $\text{SiO}_2$  powder (source: Alfa Aesar, War Hall, MA) of an average particle size of  $44\mu\text{m}$ . Steps were taken during the compaction process to ensure that maximum theoretical density could be reached for the samples without damaging the die press. Due to the restrictions from the particle size of the silica, the predicted theoretical densification leveled out at approximately 70% [19]. Pressureless sintering was carried out at  $1800^\circ\text{C}$  for 5 hours, and the finished samples were later cast into epoxy to support the samples during polishing and indentation.

The Al-Si samples were polished successively with 120, 400, 600, 800, and 1200 grit SiC sanding paper followed by  $6\mu\text{m}$ ,  $3\mu\text{m}$ , and  $1\mu\text{m}$  diamond suspension on felt cloth. The final polishing steps used  $0.3\mu\text{m}$  and  $0.05\mu\text{m}$  alumina suspensions. Samples were sonicated in an ethanol bath after each polish step. After sonication, the samples were assessed under an optical microscope to determine whether to proceed to the next polishing step. Ultimately, each polishing step was performed for 5 minutes with only one round necessary for each. To verify the quality of this procedure, atomic force microscopy (AFM) was performed in three  $20\times 20\mu\text{m}$  regions for each sample to determine the RMS value as suggested by [51]. A Park System XE70 AFM was used with a scan rate of 0.5 Hz on a two pass route.

An OPC specimen was also prepared for CSM nanoindentation using a w/c ratio of 0.5. The higher w/c was selected to promote the formation of hydration products and limit the content of unreacted clinker phases since the continuum analysis is a sound assumption for unreacted clinker phases [96], and the objective was to assess whether statistical nanoindentation can reliably measure properties of hydration products. The

sample was moist cured for 56 days before a fractured section was cast in epoxy.

The OPC 0.5 sample was dry polished to 1200 grit as outlined above, then polished with  $6\mu\text{m}$  and  $3\mu\text{m}$  diamond suspension for two rounds of 5 min each with sonication in between. The sample was then polished for 6 hours at  $1\mu\text{m}$  as recommended by Miller et al. [51]. Although this may disturb the natural porosity of the microstructure according to some researchers [90], and mentioned earlier, this polishing procedure was selected to further again maximize the probability of indenting a homogenous medium of hydration products (albeit possibly recompiled), rather than porosity.

Table 2.2: Type I/II cement composition from XRF

Oxide:	$SiO_2$	$Al_2O_3$	$Fe_2O_3$	$MgO$	$CaO$	$Na_2O$	$K_2O$	LOI
% wt.	21.78	6.10	3.24	0.83	66.9	0.10	0.57	2.58

## Nanoindentation

Nanoindentation was conducted using an Agilent Technologies G200 Nanoindenter with a diamond Berkovich indenter tip. The loading configuration made use of the enhanced Dynamic Contact Module II (DCM) functionality which allows for a displacement resolution of 0.2 pm and a force resolution of 3 nN while also maintaining a lower noise floor than standard indentation methods. CSM indentation was performed with a harmonic displacement target of 1 nm and a frequency of 75 Hz.

Al-Si 9:1, Al-Si 2:1 and OPC 0.5 samples were all indented to a depth of 300 nm with  $10\mu\text{m}$  indent spacing. Indents were performed in 20 x 20 grids for each sample. For the Al-Si samples, a poisson ratio of 0.28 was assumed according to literature regarding mullite properties [43]. The poisson ratio for the OPC sample was assumed to be 0.24 [53].

## Data analysis

Prior to statistical deconvolution of the grid indentation results, invalid tests were filtered out in two phases using a method similar to the “selective indentation” procedure

originally proposed by Amanieu et al. [3]. The Matlab programs written to import indentation test data, perform filtering and deconvolution/clustering are all included in the appendix for complete details, but can be summarized as follows.

The first filter stage assesses the self-similarity of indents as originally suggested for statistical nanoindentation [93]. Indents where  $L$  vs.  $h^2$  is non-linear are discarded by the filter step. For the purposes of this filter,  $R^2 > 0.996$  was observed to be a satisfactory requirement for linearity. It should be noted that this differs slightly from the parabolic criteria used by Amanieu et al. [3]. It should also be noted that this automated measure of linearity is likely more stringent than the visual assessments performed manually in prior statistical nanoindentation studies. Figure 2.5 displays an example of a dissimilar indent that may have passed visual assessment if only the load vs. displacement plot were judged.

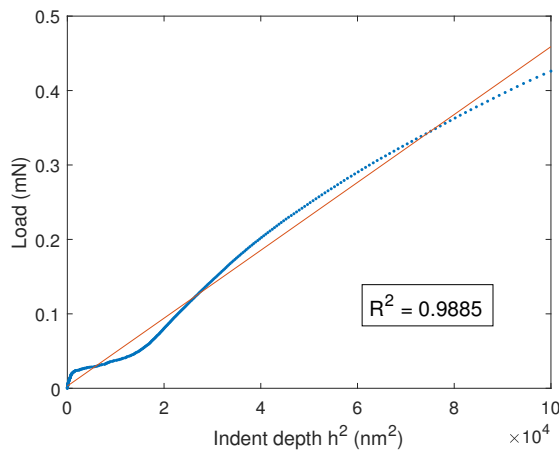


Figure 2.5: Example of a dissimilar test with a high coefficient of determination.

Indents determined to be self-similar by the first filter were then assessed for structural compliance by the second filter. Identical to the second stage described in more detail by [3], this filter measured the structural compliance,  $C_s$ , from the slope of the “SYS plot” for the indentation data from a certain depth range (Eq. 2.10). The depth range proposed by Amanieu et al. with sound reasoning was 45 - 75 nm and this was used for the Al-Si samples. For the OPC sample, however, the depth range used for analysis was 45 - 245 nm

since the RVE for OPC must be larger to accommodate for the nanogranular nature, which is observed for indent depths of 100-300 nm [18]. Indents where  $C_s < 4.0 \times 10^{-6}$  were discarded by this filter, as suggested by Amanieu et al. based on empirical results from fused silica [3]. For indents deemed to be non-compliant by the filter ( $C_s < 4.0 \times 10^{-6}$ ), the continuum analysis is valid and the modulus was averaged over the selected depth range.

The moduli of indents that only passed the first filter stage were also averaged over the same depth range to provide results for a comparison showing the effect of the compliance filter. The filtered moduli results from each sample were then analyzed using belief-based clustering as described earlier. Fig. 2.6 shows a flowchart summarizing the data processing process.

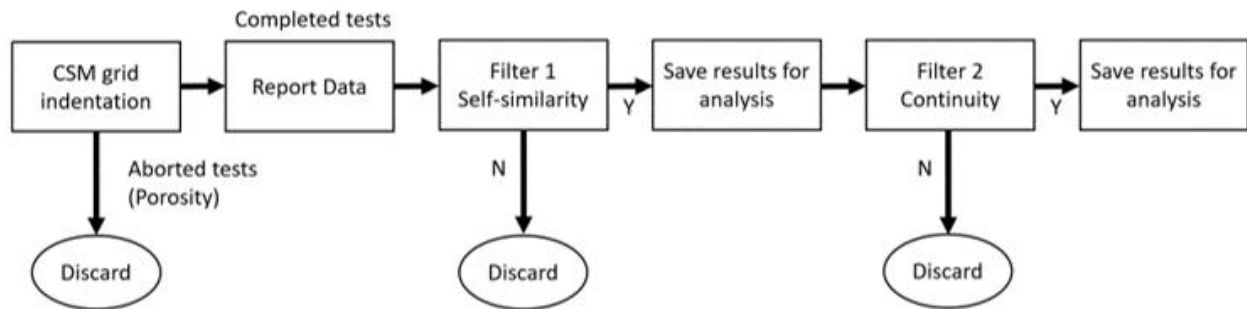


Figure 2.6: Flowchart of CSM grid indentation data processing.

### 2.2.3 Phase verification

In order to determine the phases present in each sample and estimate the volume fractions of the phases, the following microscopy methods and models were used.

After indentation tests were completed, the Al-Si ceramic samples were gold sputtered before being placed into a JEOL-7000 SEM equipped with an Oxford EDX for chemical analysis and qualitative determination of the average characteristic lengths of the phase distributions in both mixtures. Imaging was performed using an accelerating voltage of 20keV at a working distance of 10 mm. EDS maps of indentation areas were obtained for both ceramic samples along with isolated spectra at points located within distinct phase constituents in both mixtures.

The NIST CEMHYD3D model [9] was used to model the microstructure of the OPC 0.5 sample tested in this study and also the OPC 0.36 sample from Sebastiani et al. [76]. The number of hydration cycles performed by the model were 600 and 1200 for the OPC 0.36 and 0.5 samples respectively to account for the different curing durations prior to nanoindentation. The cement for both samples was approximated as CCRL cement 133 for the model input. The input files for the CEMHYD3D v3.0 code are included in the appendix along with the Matlab program used for plotting a cross-section of each microstructure.

## 2.3 Results

### 2.3.1 Clustering of high-speed nanoindentation data

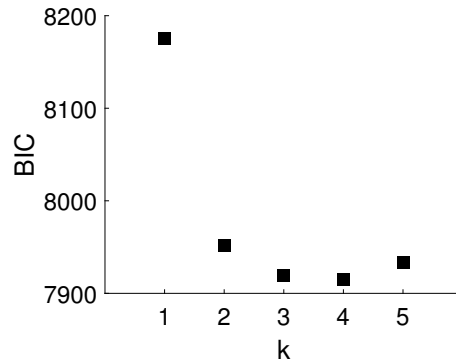
Results of Gaussian mixture modelling and clustering of the 0% and 100% SoC  $\text{Li}_x\text{Mn}_2\text{O}_4$ -based composite datasets are shown in Fig. 2.7 and 2.8 respectively. For the 0% SoC sample, the BIC indicates that four clusters (i.e. phases) provide the most probable GMM. The posterior probability of the mean of each of these clusters lies around 80%, suggesting that their assignment is probable although significance is not implied by the PDF.

The 100% SoC sample dataset was determined to have three clusters according to BIC. The posterior probability of these cluster assignments appears to be more likely compared to the four clusters assigned to the 0% SoC sample. This observation may be attributed to more pronounced clustering of the data, and/or the the removal of an additional cluster to share likelihood with.

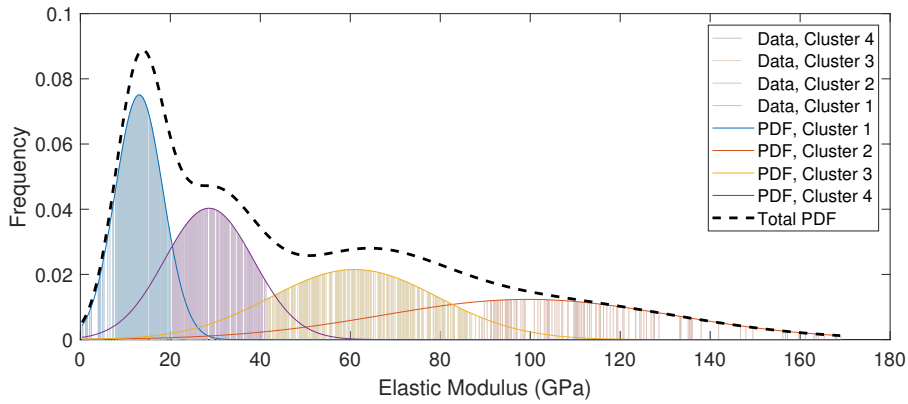
Fig. 2.9 details the analysis of the OPC 0.36 sample dataset. Although the BIC for the OPC 0.36 data was technically lowest for three clusters,  $k=3$ , the authors originally used  $k=4$  in their CDF deconvolution [76] so  $k=4$  is used here as well since the BIC is only marginally higher than that of  $k=3$ . The distributions assigned to each cluster overlap greatly in the PDF of Fig. 2.9. When the posteriors are considered it is apparent that the

means of clusters 3 and 4 are more likely assigned to cluster 1 (Fig.2.9 c). The most probable posterior in this GMM is in fact the cluster attributed to modulus values  $>60$  GPa or  $<10$  GPa, likely corresponding to unhydrated or porous phases respectively.

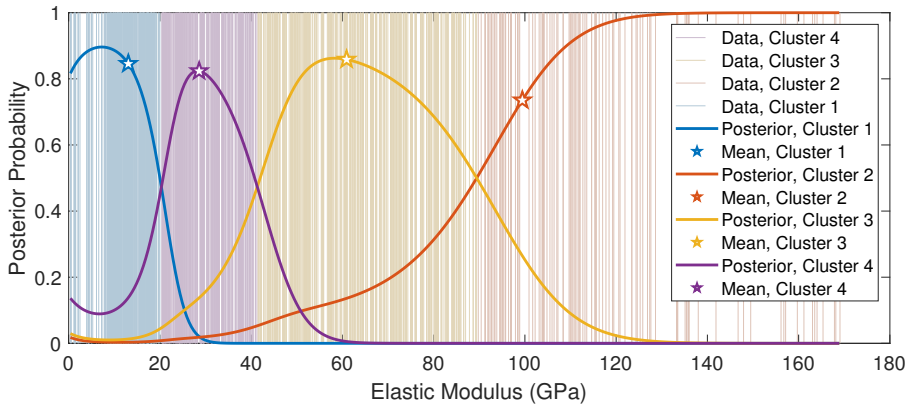
An apparent issue with this large OPC 0.36 dataset is the largeness itself (33,134 indents). The BIC does not penalize higher model orders when the sample size is increased [88]. This may effectively allow the data to be “over-fit” in the sense that additional phases may be assigned to intermediate clusters to improve the overall likelihood. For an example of this, roughly half of the data in the Gaussian distribution of cluster 4 in Fig. 2.9 is more likely to belong to cluster 1. The same is true for a greater portion of cluster 3. The number of data in these seemingly unnecessary clusters is too great for the maximum likelihood algorithm to disregard, however.



(a) BIC for different models

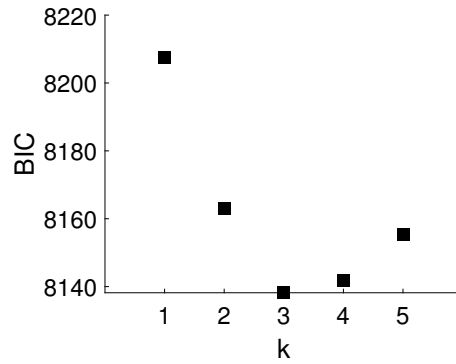


(b) Probability density function of cluster assignments

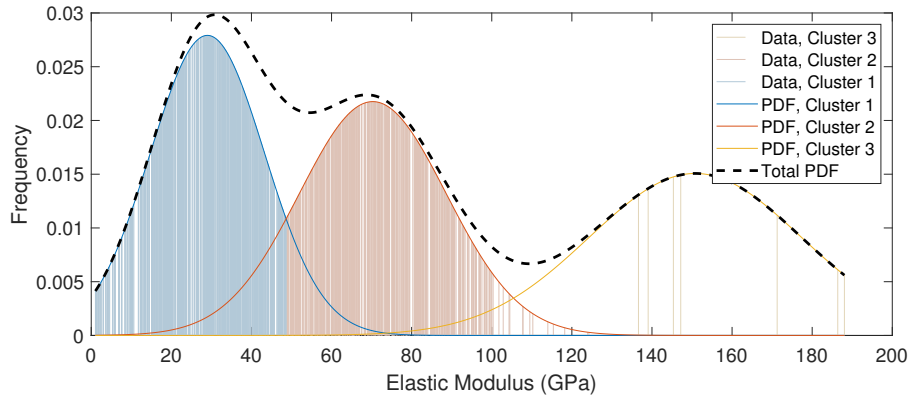


(c) Posterior probability of cluster assignments

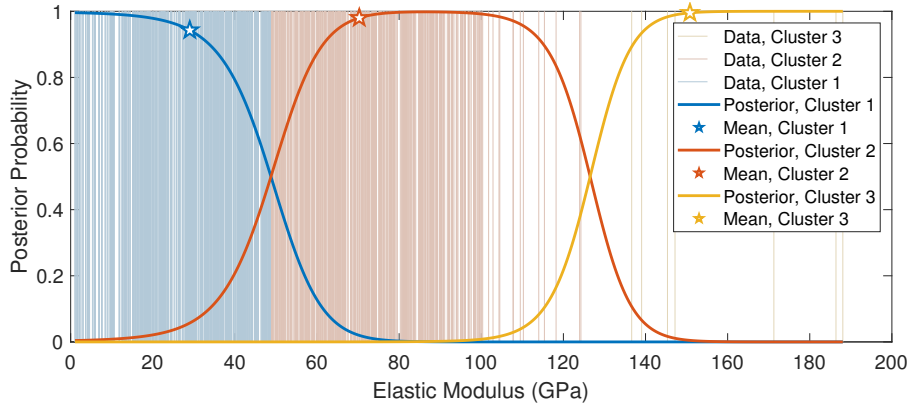
Figure 2.7: GMM selection and cluster assignments for the high-speed indented 0% SoC sample. Vertical lines represent individual test results and may appear as solid fill where data are abundant.



(a) BIC for different models

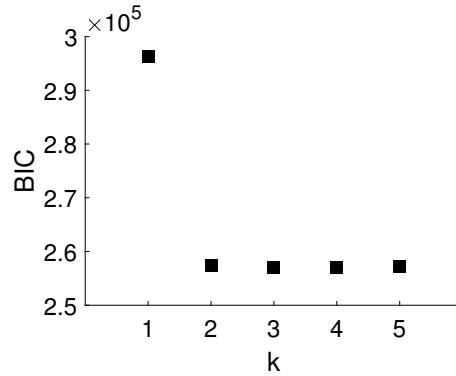


(b) Probability density function of cluster assignments

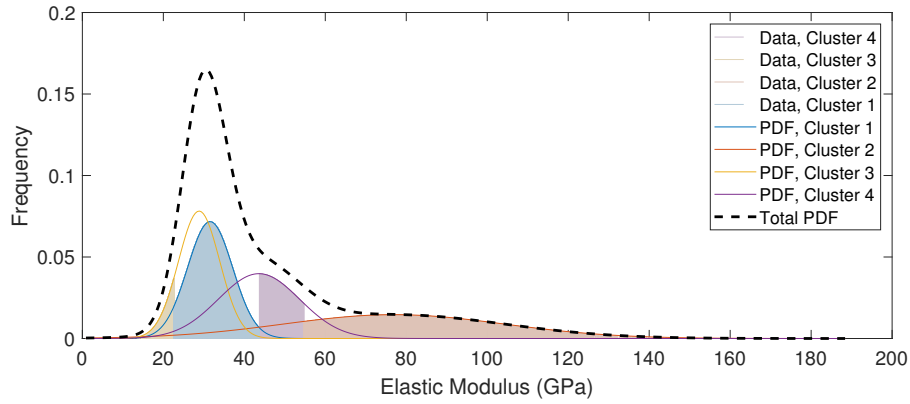


(c) Posterior probability of cluster assignments

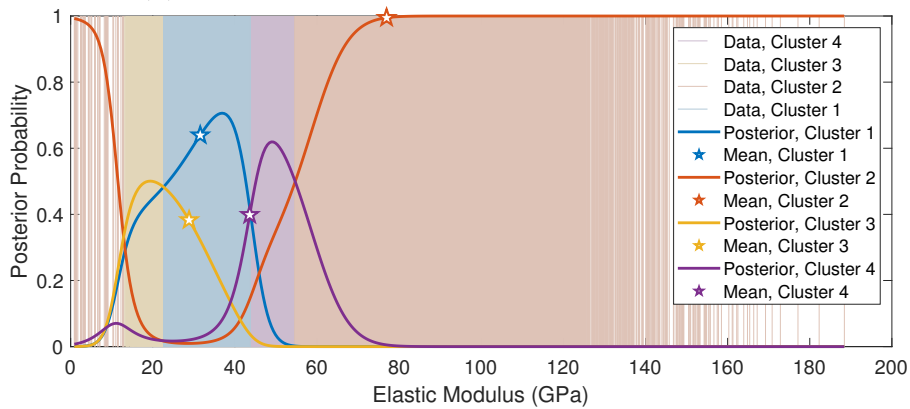
Figure 2.8: GMM selection and cluster assignments for the high-speed indented 100% SoC sample. Vertical lines represent individual test results and may appear as solid fill where data are abundant.



(a) BIC for different models



(b) Probability density function of cluster assignments



(c) Posterior probability of cluster assignments

Figure 2.9: GMM selection and cluster assignments for the high-speed indented OPC 0.36 sample. Vertical lines represent individual test results and may appear as solid fill where data are abundant.

### 2.3.2 Clustering of nanoindentation data with filtering for self-similarity

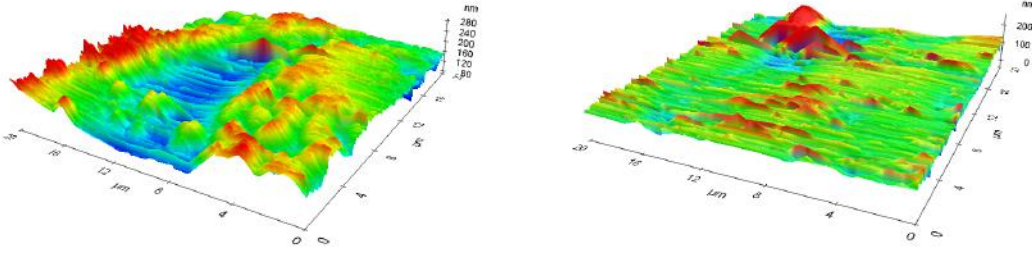
In this section, GMM and clustering is presented for the Al-Si ceramics and OPC 0.5 sample datasets after filter stage 1 was performed to remove aberrant and dissimilar tests. These results are considered to be what the traditional statistical nanoindentation [16] results would be, although the automated preprocessing of data may be more stringent than the manual validation of data quality originally proposed, as mentioned earlier in the methods. Table 2.3 shows the efficiency of each filter phase, suggesting that indeed the algorithmic filtering does in fact eliminate more tests than stated for original statistical nanoindentation studies [16].

Table 2.3: Grid indentation preprocessing filter efficiencies

Sample	Completed tests, $N$	Filter 1		Filter 2	
		# of tests passed	% passing	# of tests passed	% passing
Al-Si 9:1	400	147	37%	40	10%
Al-Si 2:1	399	295	74%	31	8%
OPC 0.5	391	135	34%	20	5%

The Al-Si 2:1 sample yielded about twice as many self-similar tests than the Al-Si 9:1 and OPC 0.5 samples (Table 2.3). This discrepancy could be attributed to the different surface roughness of each sample, as seen in the topography of the Al:Si samples determined from AFM (Fig. 2.10). Possible relief between phases in the Al-Si 9:1 sample can be observed while the Al-Si 2:1 sample containing one dominant mullite phase (as discussed later) provides a flatter surface. The surface roughness can diminish the yield of valid results, and these results may also suggest that the heterogeneity of the microstructure influences the surface roughness.

However, both of these samples satisfied the proposed RMS requirements for statistical nanoindentation [51]. Close examination of Fig. 2.10 indicates that flat surfaces are present throughout the sample, except where there is suspected relief between phases. Should an indent land in an area of topographic relief, it is highly likely that this is the location of a phase boundary therefore providing a heterogeneous RVE. As previously



(a) Al-Si 9:1

(b) Al-Si 2:1

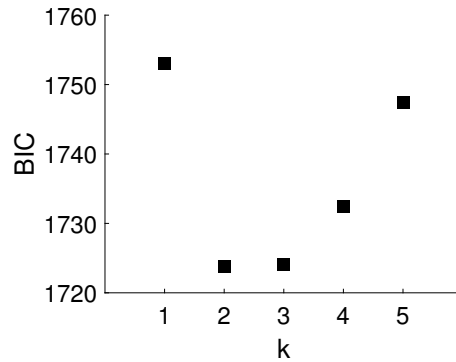
Figure 2.10: Representative AFM scans of Al-Si samples

remarked, the possibility of a heterogeneous RVE may not only be encountered at visible surface boundaries of phases, but also at various depths for locations where Buckle’s rule inevitably does not hold true. Therefore it is reasonable to assume that the heterogeneity of phases in the microstructure of each sample, which will be presented in section 2.3.4, dictates the yield of self-similar test results when an acceptable surface roughness is present. Nevertheless, both filter stages are highly effective in eliminating tests that are liable of influence from the microstructure (Table 2.3).

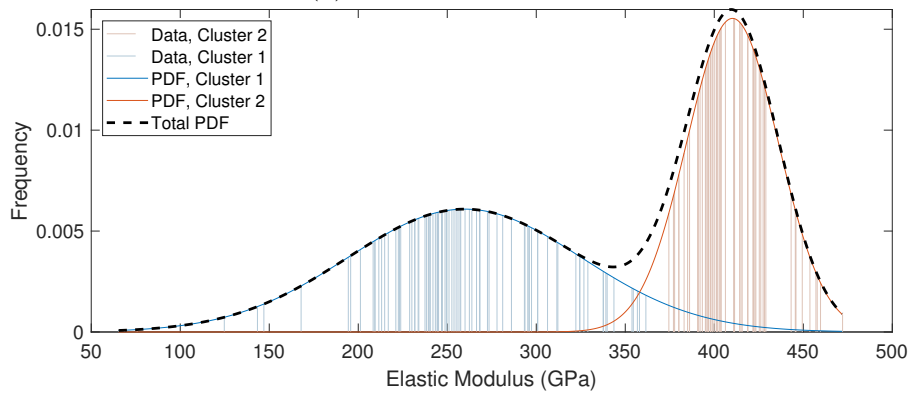
The BIC indicates  $k=2$  for the Al-Si 9:1 sample (Fig. 2.11), whereas  $k=3$  is suggested for the Al-Si 2:1 sample (Fig. 2.12). The model order of  $k=3$  was also a likely candidate for the Al-Si 9:1 sample, however. Posterior probabilities of all cluster assignments in both samples are generally higher than 95%, which suggests that the assigned GMM provides a high likelihood for all of the clustered data. This differs from the results of the high speed datasets where the probability of some clusters was reduced in order to increase the overall likelihood of the GMM.

For the OPC 0.5 sample, no separate clusters were assigned according to the BIC, as shown in Fig. 2.13. It should be noted that one outlier test with modulus  $>90$  GPa was excluded from this dataset, since it would simply be assigned a separate erroneous cluster

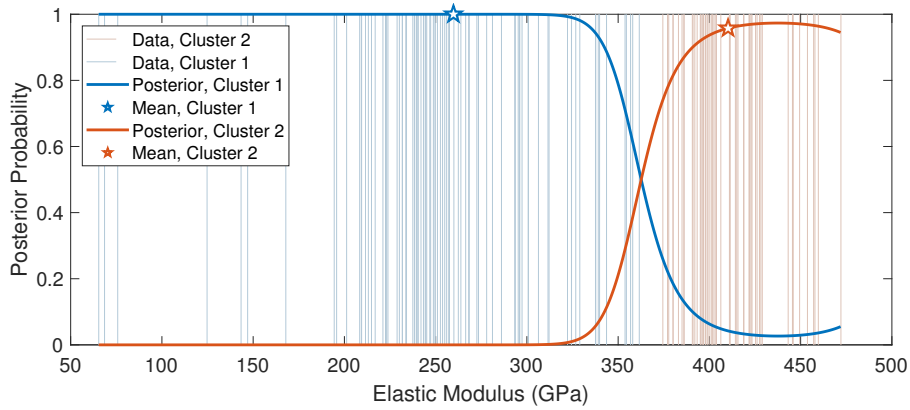
in the GMM. The lack of data  $>60$  GPa can be attributed to the higher w/c ratio used, as will be discussed later.



(a) BIC for different models

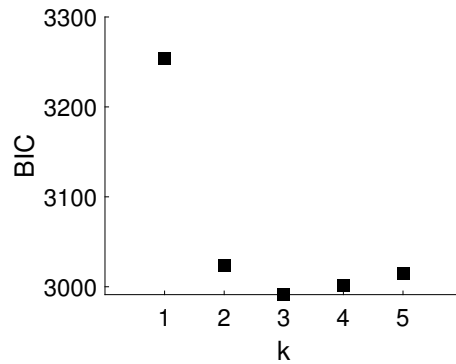


(b) Probability density function of cluster assignments

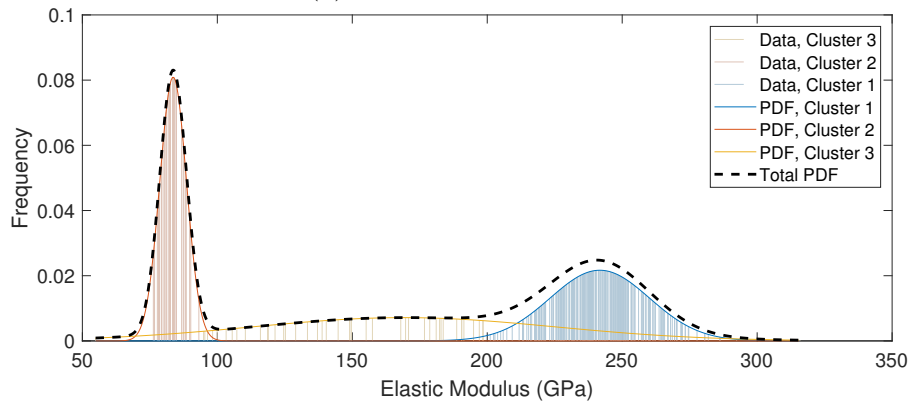


(c) Posterior probability of cluster assignments

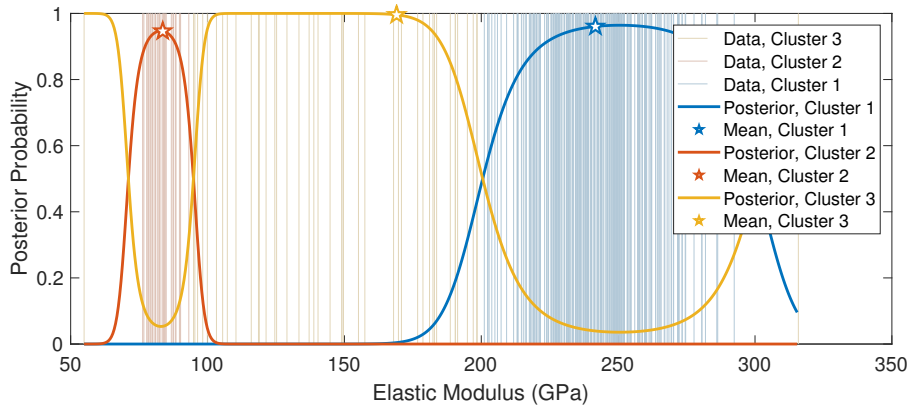
Figure 2.11: GMM selection and cluster assignments for the Al-Si 9:1 after filter 1. Vertical lines represent individual test results and may appear as solid fill where data are abundant.



(a) BIC for different models

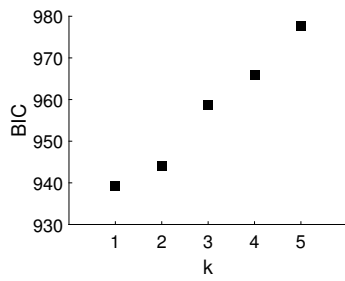


(b) Probability density function of cluster assignments

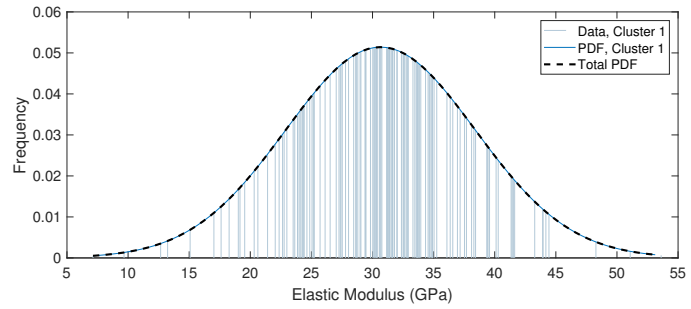


(c) Posterior probability of cluster assignments

Figure 2.12: GMM selection and cluster assignments for Al-Si 2:1 sample after filter 1. Vertical lines represent individual test results and may appear as solid fill where data are abundant.



(a) BIC for different models



(b) Probability density function of cluster assignments

Figure 2.13: GMM selection and cluster assignments for OPC 0.5 after filter 1. Vertical lines represent individual test results and may appear as solid fill where data are abundant.

### 2.3.3 Clustering of nanoindentation data filtered for self-similarity and structural compliance

After filter stage 2, where the indents with additional structural compliance are discarded, 10% or fewer data of the indents performed remain (Table 2.3). The number of tests is still roughly a magnitude of order higher than  $k$ , so the statistical analysis may still offer some insight [10, 31].

The BIC strongly indicates that  $k=2$  for the Al-Si 9:1 sample. Fig. 2.14 shows this improvement due to the additional filtering, including the increased posterior probability of the clusters. Fig. 2.15 shows the determination of four clusters for the Al-Si 2:1 sample, all of which appear to be significant.

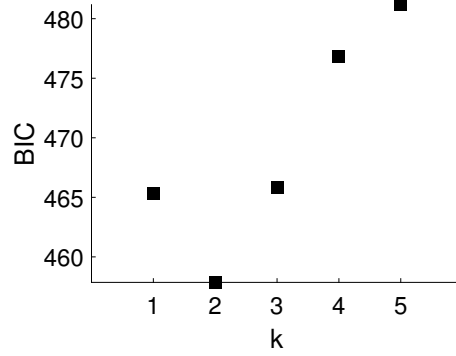
While the original results for the OPC 0.5 sample did not have any apparent clusters, the compliance filtered data yield the lowest BIC for  $k=2$  followed by  $k=4$  (Fig. 2.16). The posterior probability of the two clusters in the selected GMM are nearly 1.

Table 2.4: Summary of filtered CSM nanoindentation data deconvolution using belief-based clustering.

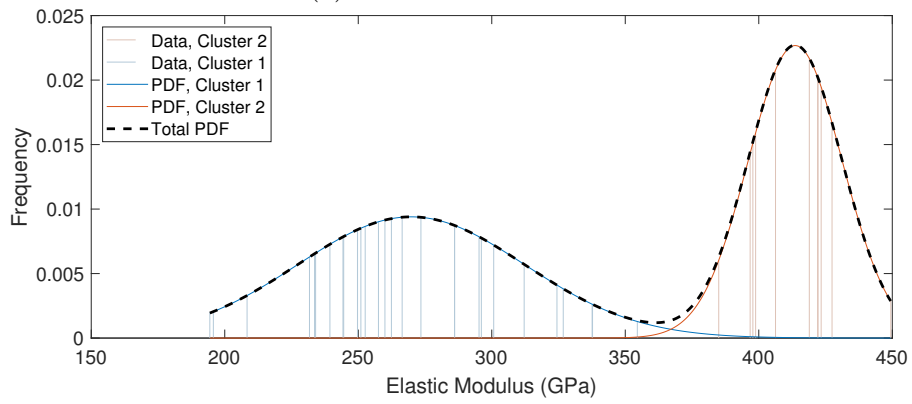
Filter	Cluster: Sample	1			2			3			4		
		$\mu$	$\sigma^2$	$f_J$	$\mu$	$\sigma^2$	$f_J$	$\mu$	$\sigma^2$	$f_J$	$\mu$	$\sigma^2$	$f_J$
1	Al-Si 9:1	259.75	65.54	0.61	410.24	25.68	0.39	169.08	55.88	0.20			
	Al-Si 2:1	241.70	18.40	0.70	83.64	4.93	0.10						
	OPC 0.5	30.65	7.76	1.00									
2	Al-Si 9:1	269.81	42.45	0.73	413.64	17.59	0.27	241.28	10.37	0.40	129.88	12.77	0.16
	Al-Si 2:1	80.42	2.37	0.23	198.81	10.20	0.22						
	OPC 0.5	44.23	6.80	0.27	34.14	2.41	0.73						

Table 2.5: Summary of high speed nanoindentation data deconvolution using belief-based clustering.

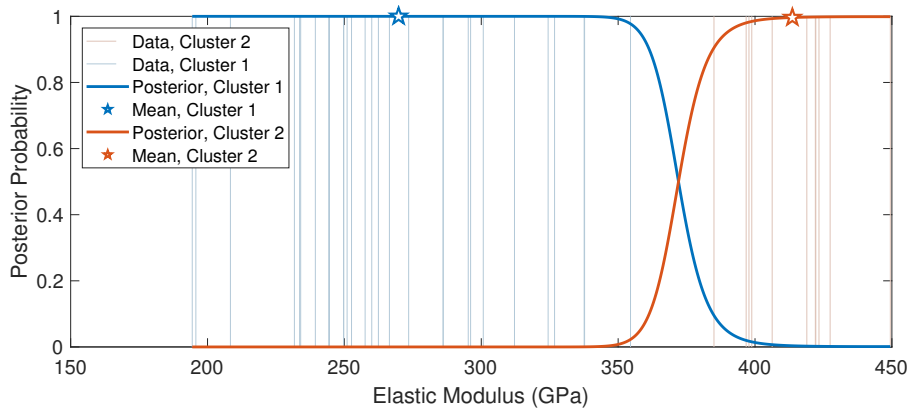
Sample	Cluster: Sample size, $N$	1			2			3			4		
		$\mu$	$\sigma^2$	$f_J$	$\mu$	$\sigma^2$	$f_J$	$\mu$	$\sigma^2$	$f_J$	$\mu$	$\sigma^2$	$f_J$
SoC 0%	817	13.08	5.31	0.23	99.43	32.34	0.19	60.92	18.56	0.34	28.60	9.90	0.24
SoC 100%	861	29.01	14.29	0.50	70.29	18.34	0.49	150.82	26.47	0.01			
OPC 0.36	33,134	31.55	5.56	0.49	76.94	27.29	0.17	28.84	5.10	0.26	43.61	10.03	0.08



(a) BIC for different models

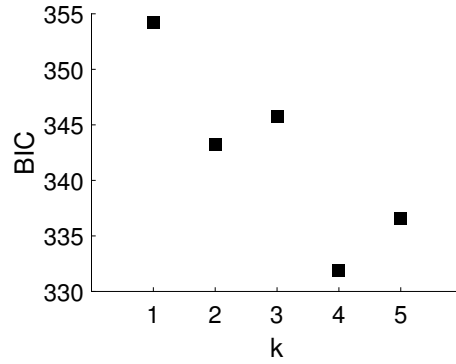


(b) Probability density function of cluster assignments

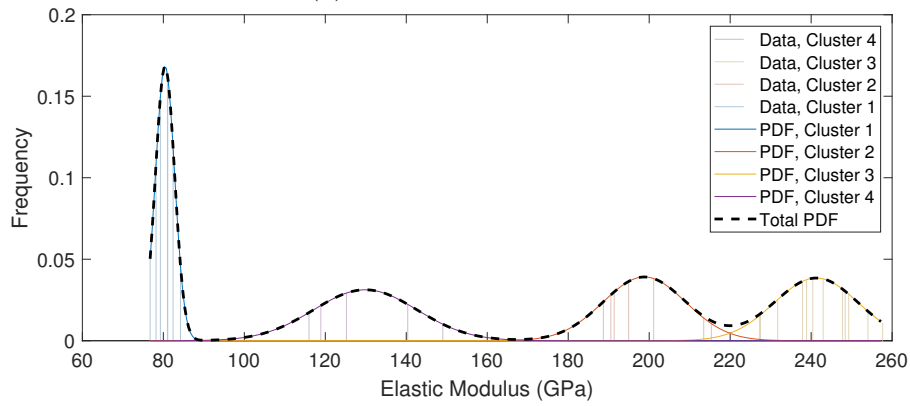


(c) Posterior probability of cluster assignments

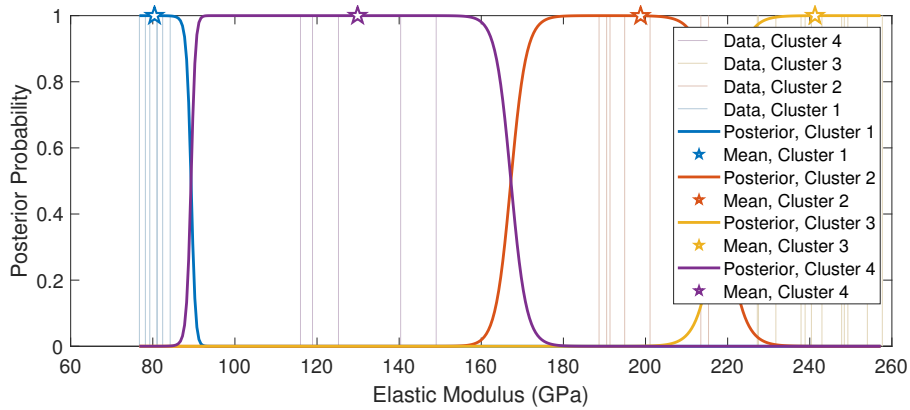
Figure 2.14: GMM selection and cluster assignments for Al-Si 9:1 sample after filter 2



(a) BIC for different models

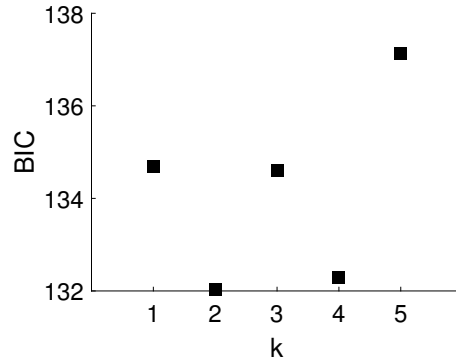


(b) Probability density function of cluster assignments

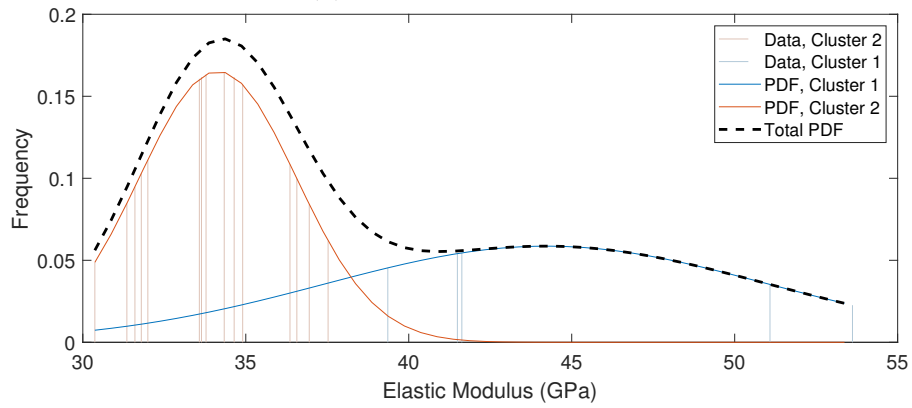


(c) Posterior probability of cluster assignments

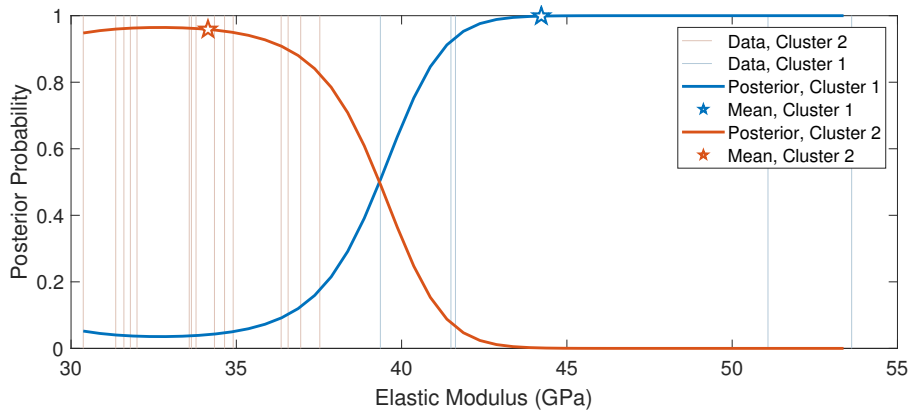
Figure 2.15: GMM selection and cluster assignments for Al-Si 2:1 sample after filter 2



(a) BIC for different models



(b) Probability density function of cluster assignments



(c) Posterior probability of cluster assignments

Figure 2.16: GMM selection and cluster assignments for OPC 0.5 after filter 2

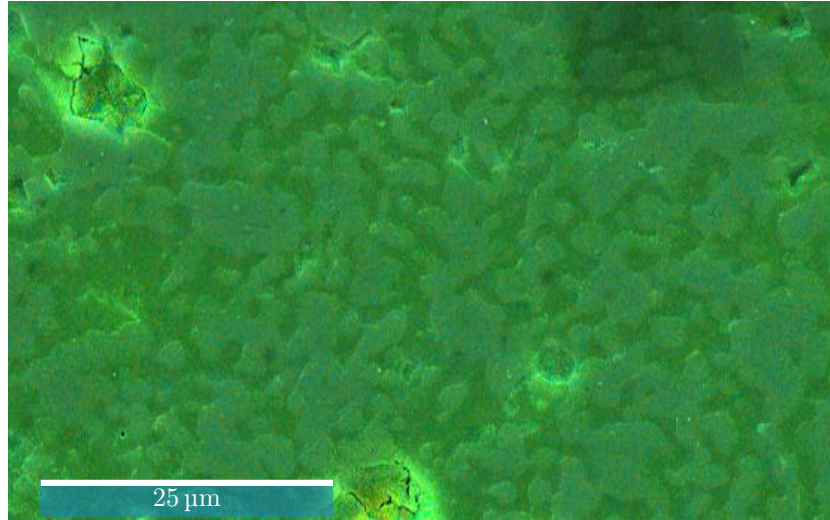
### 2.3.4 Phase verification

Phase verifications were performed for all of the samples except the  $\text{Li}_x\text{Mn}_2\text{O}_4$ -based cathode material datasets that were obtained from [57]. The verifications were performed in the methods deemed best for qualitative discussion, rather than overall quantitative accuracy.

The SEM-EDS analysis of the Al-Si 9:1 sample is shown in Fig. 2.17. The microstructure appears to have two distinct phases of different Al/Si. According to the phase diagram of Toroprov and Galakhov [86], the sintering process should have produced  $\text{Al}_2\text{O}_3$  agglomerated by an Al-rich mullite phase [29]. EDS spot scans of phase, spectra for which are included in the appendix, show agreement with the phases suggested by the literature. EDS mapping of the microstructure was used to produce a segmented image of the phases (Fig. 2.17 e) suggesting volume fractions of 55%  $\text{Al}_2\text{O}_3$ , 45% mullite, and 3% porosity.

The composition of the Al-Si 2:1 theoretically should have been predominantly mullite with an excess solid solution. Fig. 2.18 seems to confirm crystalline needles formed during the sintering process and were agglomerated by the excess solution with higher Si proportions. EDS spot scans (see appendix) for the phases also showed agreement with literature. The estimated volume fraction of mullite produced was 72% with 28% solid solution (Fig. 2.18 e)

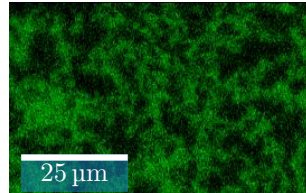
The OPC sample phases were estimated using the NIST model to obtain clear phase distinctions as seen in Fig. 2.19 and 2.20 for the 0.36 and 0.5 w/c samples respectively. The results support the expected behavior that the higher w/c ratio of 0.5 with a lower curing duration did result in slightly more calcium silicate hydrate (C-S-H) formation at the cost of additional porosity. Different densities of C-S-H formed were not distinguished in the modelling approach since the more porous products are likely to be filtered out based on prior microscopic analysis and testing [23]. The calcium hydroxide (CH) content of both OPC samples is reported to be similar in the models.



(a) Overall intensity map



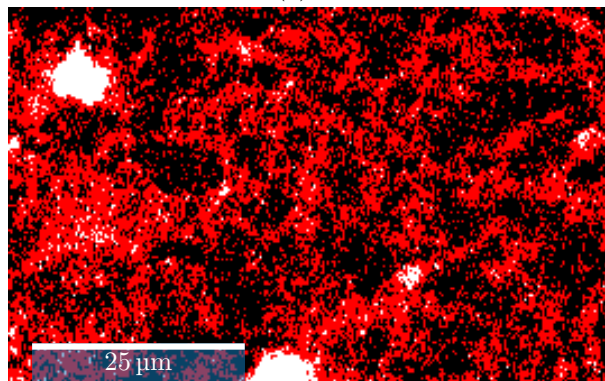
(b) Aluminum



(c) Silicon

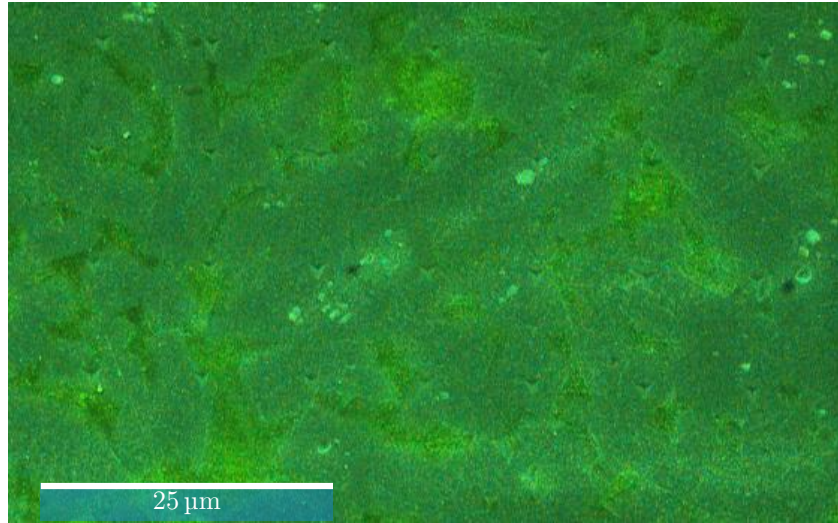


(d) Oxygen

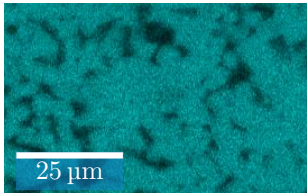


(e) Segmented image: 55%  $\text{Al}_2\text{O}_3$  (black), 45% mullite (red), and 3% porosity (white)

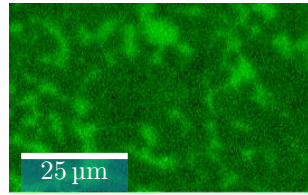
Figure 2.17: SEM-EDS analysis of Al-Si 9:1 sample.



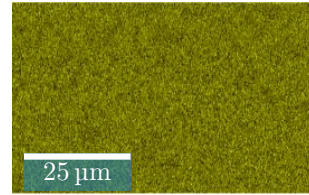
(a) Overall intensity map



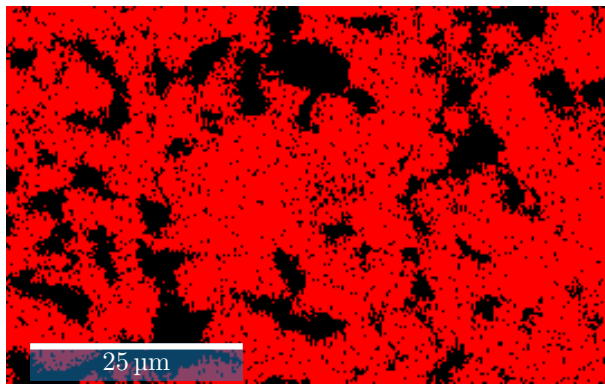
(b) Aluminum



(c) Silicon



(d) Oxygen



(e) Segmented image: 72% mullite (red) and 28% solid solution (black)

Figure 2.18: SEM-EDS analysis of Al-Si 2:1 sample.

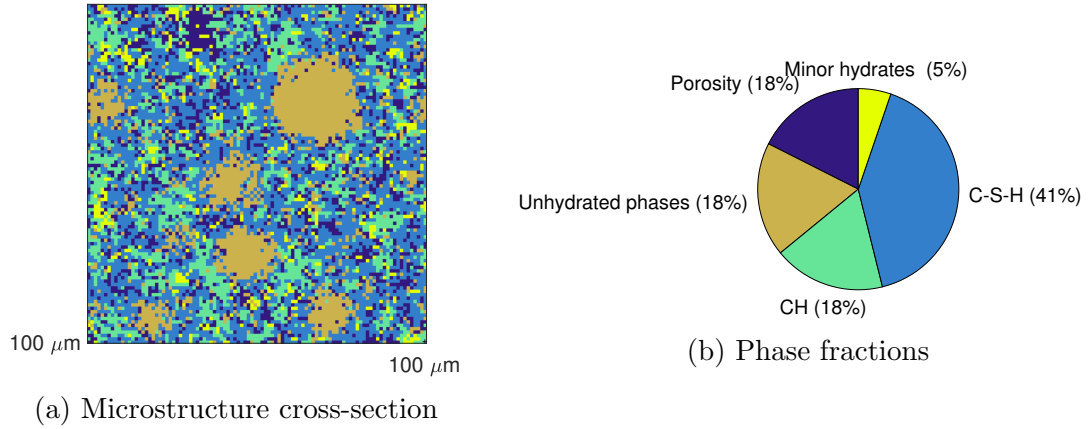


Figure 2.19: CEMHYD3D model output for OPC 0.36 sample

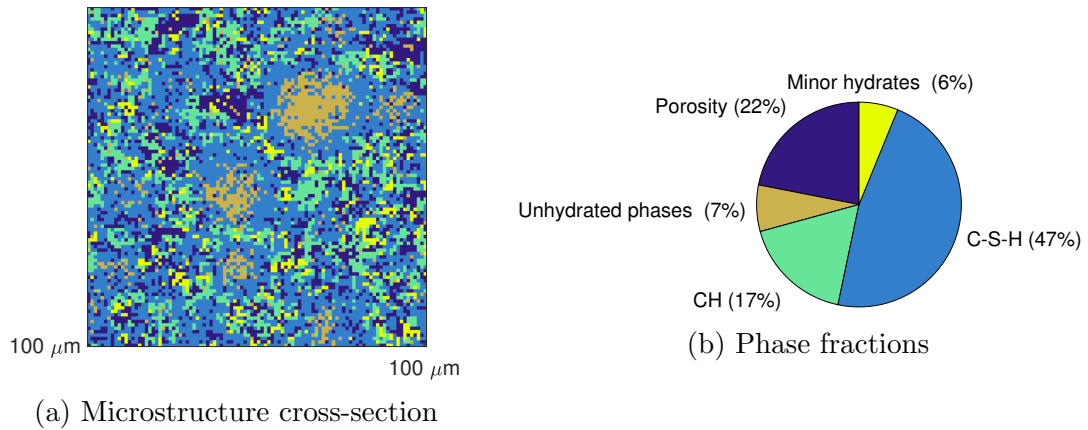


Figure 2.20: CEMHYD3D model output for OPC 0.5 sample

## 2.4 Discussion

### 2.4.1 $\text{Li}_x\text{Mn}_2\text{O}_4$ -based cathode materials

The data obtained by Mughal et al. [56, 57] were re-analyzed in this study. The samples were comprised of  $\text{Li}_x\text{Mn}_2\text{O}_4$  particles embedded in an epoxy matrix with some polyvinylidene fluoride and carbon black constituents [3, 56]. Theoretically, this should have corresponded to two primary phases although the crystal orientation can influence the indentation response of the  $\text{Li}_x\text{Mn}_2\text{O}_4$  phase [3]. Based on the literature, the  $\text{Li}_x\text{Mn}_2\text{O}_4$  phase should have a modulus of approximately 87 GPa or 104 GPa For 0% and 100% SoC respectively, though reported values range between 80-200 GPa [2, 56]. The primarily epoxy matrix could be expected to have a modulus  $<10$  GPa [3].

The results for the 0% and 100% SoC samples both report an intermediate phase or two between the moduli values for the anticipated phases. These intermediate phases could be attributed to the additional structural compliance encountered at indents near phase boundaries, especially since the epoxy matrix was significantly weaker than the  $\text{Li}_x\text{Mn}_2\text{O}_4$  phases. The gradients near phase boundaries observed in the grid indentation maps presented by Mughal et al. [56] support this theory. These high speed nanoindentation datasets not only neglect to account for potential sources of structural compliance, but they also have not been methodically checked for self-similarity. The results of this analysis suggest that increasing the number of indents,  $N$ , does not actually improve the signal-to-noise ratio if indentation quality is not assured.

It should be noted, however, that a difference can be observed between the results for the 0% and 100% SoC samples. Of the four phases determined for 0% SoC, the one centered around 100 GPa most likely corresponds to the  $\text{Li}_x\text{Mn}_2\text{O}_4$  phase (Fig. 2.7). For 100% SoC, where  $k=3$ , the phase around 150 GPa is the more likely candidate to contain indents attributed to the  $\text{Li}_x\text{Mn}_2\text{O}_4$  phase (Fig. 2.8). While this roughly correlates to the strength gain expected for the higher SoC [2, 56], the 150 GPa phase contains only several tests. This indicates that the entire  $\text{Li}_x\text{Mn}_2\text{O}_4$  phase may not have adhered to the

structural change. Upon further inspection of the grid indentation maps presented in Fig. 1 of [56], it can be confirmed visually that the higher moduli values are all localized in one larger particle of  $\text{Li}_x\text{Mn}_2\text{O}_4$ . This observation is likely attributed to different levels of lithiation of particles, which has been found to affect stiffness measurements [2]. The packing of  $\text{Li}_x\text{Mn}_2\text{O}_4$  particles also appears to be somewhat denser in the SoC 0% sample. Porosity within the particles, as revealed by FIB-SEM microscopy [3], could also have diminished the indentation response of the SoC 100%.

Nevertheless, these results suggest that some information can be gleaned from statistical nanoindentation concerning changes in a single phase property for samples of the same intrinsic microstructure, even without preprocessing of the data. A main assumption of this capability is that the influence of the microstructure remains relatively constant for both samples, while the properties of a single phase are altered. This is only a qualitative observation in this case, however, and is more appropriately interpreted from the grid indentation maps originally presented by Mughal et al. [56]. Higher resolution maps obtained in a rapid manner are the primary reason to perform high speed nanoindentation [36], so the qualitative contributions of the statistical analysis may be redundant.

#### **2.4.2 Al-Si ceramics**

According to the microscopic analysis, the Al-Si 9:1 sample is comprised of two distinct phases that should exhibit different mechanical properties. Fittingly, the statistical analysis suggests that two phases are present, both with and without compliance based filtering. The clusters are centered around Gaussian peaks/means of 410 GPa and 260-270 GPa (Table 2.4), likely corresponding to the  $\text{Al}_2\text{O}_3$  and mullite phases respectively. These values agree with moduli presented in literature for each phase, although the mullite phase is higher than the documented value of near 240 GPa [43]. Nanoindentation has previously reported higher values for mullite, however, and the higher Al content in this sample may also increase the strength [11, 29].

While the cluster means for the Al-Si 9:1 sample remain relatively constant before and after compliance filtering, the volume fraction of the phases is altered. The  $\text{Al}_2\text{O}_3$  phase is only 27% after compliance filtering, compared to 39% beforehand (Table 2.4). Considering the microscopic analysis, which suggested 55%  $\text{Al}_2\text{O}_3$ , there is an apparent bias against this phase concerning valid indents where continuity is preserved. Because of relatively limited sampling and resolution, grid indentation is not the most accurate method of measuring volume fractions. However, these results support the notion that grid indentation can be coupled with preprocessing and an unbiased statistical analysis to accurately determine phase properties.

Prior to compliance filtering of the Al-Si 2:1 dataset, three phases were determined (Fig. 2.11). Two clusters centered around 240 and 80 GPa likely correspond to mullite and a higher Si content phase respectively [43, 65]. The third cluster is spread in between these clusters and could be interpreted as an erroneous intermediate phase that is comprised of indents with additional structural compliance. The compliance filtered results suggest four phases, however. Similar to the initial results, there are two clusters around 240 and 80 GPa but there are now two intermediate phases around 200 and 130 GPa. These intermediate phases are unlikely to be the result of additional structural compliance. The variability of these phases seems to be a more appropriate explanation for these separate mechanical phases.

Although the microscopic analysis and literature suggest two primary phases for the Al:Si 2:1 sample, the formation and assemblage of these phases present greater complexity. The mullite needles formed in these samples would likely yield varying indentation responses based on orientation. The excess solution phase also may vary due to variable composition since it is an undefined sintering byproduct. These are all possible explanations for additional mechanical phases determined by the statistical analysis.

As seen in the Al-Si 9:1 sample, the volume fractions of the Al-Si 2:1 sample results suggest that there is bias in the mechanical response of certain phases. The primary

mullite phase of 72% vol. according to the microscopic analysis, is reduced to a mere 40% in the fully filtered nanoindentation results. There appears to be a trend with both Al-Si samples where stronger phases are more likely to provide an invalid indentation response. If the thin-film analogy exploited in the original statistical nanoindentation technique were appropriate, the substrate influence (i.e. structural compliance) would be just as likely for the weaker phases. The bias observed in these results further suggests that the thin-film analogy cannot fully explain the influence of a heterogeneous microstructure on nanoindentation responses. Interaction between phases cannot be dismissed for microstructures with the level of heterogeneity seen in the samples discussed here.

The need for compliance filtering in order to employ the continuum analysis may be fundamentally clear, yet the results shown for the Al-Si samples without compliance filtering show better agreement with the volume fractions determined from microscopy. This is particularly evident for the Al-Si 2:1 sample, where 70% of indents were attributed to the mullite phase by the clustering algorithm (Fig. 2.12, Table 2.4), which agrees with the 72% determined by microscopy (Fig. 2.18). This corroborates with the original validation of the method where the anticipated volume fractions were obtained in the statistical analysis of the indentation grid [16]. Moreover, agreement between microscopy and statistical nanoindentation volume fractions was even accomplished for an alkali activated fly ash cement by Das et al. [21].

However, this finding should not come as a surprise since the original method specified that each indent should be a statistically independent event over an appropriately spaced grid over a representative area. By applying a filter for indent quality, the statistical representation of the grid is greatly disturbed. This does not outweigh the importance of ensuring indent quality, but perhaps for certain microstructures (of limited heterogeneity), the assigned Gaussian distributions can effectively account for the additional structural compliance that a given phase may exhibit.

Why then do the  $\text{Li}_x\text{Mn}_2\text{O}_4$  composites not also replicate these results in achieving

remotely accurate volume fractions of phases? As suggested earlier, a likely cause for the erroneous phases in the high speed nanoindentation data could be the lack of a filter for even the self-similarity of indents. The Gaussian distribution may accommodate compliance or interaction between phases to some extent, although the original method explicitly assumes no interaction [16], but dissimilar indentation data cannot provide relevant data. While filtering the indentation data can improve the reliability of the data, the statistical significance, especially regarding phase volume fractions is greatly diminished. These limitations are important to consider when applying the statistical nanoindentation technique.

### 2.4.3 Ordinary portland cement

The OPC 0.36 high speed nanoindentation dataset was originally deconvoluted using the CDF and a minimum square error algorithm in [76]. Four phases were found to provide the most stable deconvolution and were assigned to three C-S-H phases of varying densities and a clinker phase [76]. The belief-based clustering employed here also supports the selection of a four phase GMM (Fig. 2.9). The assigned clusters differ here, however, with clusters identified around 29, 32, 44, and 77 GPa. Even though there was substantial content of unhydrated clinker in the microstructure ([76] and Fig. 2.19), the clustering algorithm did not allocate a cluster to values  $>100$  GPa that are characteristic of clinker phases [96]. Given the high signal-to-noise ratio of the dataset [76], one would expect the unbiased statistical algorithm to at least make the distinction of hydrated and unhydrated products from this dataset.

High speed nanoindentation may be able to provide an unprecedented number of data with impressively well *fitting* statistical deconvolutions, but as stated earlier, the signal-to-noise ratio may not actually improve. A rising concern then is that perhaps some of the various clusters assigned to the OPC 0.36 dataset are simply erroneous phases, as seen with the  $\text{Li}_x\text{Mn}_2\text{O}_4$  samples. Ranging densities of C-S-H are a convenient explanation for the various phases with valid support in literature [37, 87], but this may not be the

true cause for the according indentation responses. This theory is easily confirmed by considering that over 90% of indents were attributed to the proposed C-S-H phases in the original CDF analysis of the dataset [76]. The microstructure modelled for the OPC 0.36 sample suggests that the total C-S-H content is very unlikely to exceed 50%. Furthermore, the hydration model affirms that calcium hydroxide (CH) is a significant product, which happens to have a modulus close to 42 GPa [34]. The conversion of calcium hydroxide (CH) to calcium carbonate would also potentially conflict with the proposed ultra-high density C-S-H phase with a reported modulus near 80 GPa [34]. The clustering of the OPC 0.36 dataset (Fig. 2.9) does, however, agree with some accuracy to the phase dominance of high density (HD)C-S-H and CH (Fig. 2.19) with reported moduli near 32 and 44 GPa respectively [34, 102]. Despite coincidental agreements of moduli, the confidence of these cluster assignments is quite low (Fig. 2.9).

The recent use of quantitative SEM-EDS coupled with grid indentation addresses the dilemma of discerning phase assignments in cementitious materials [102], which is obviously a pitfall of the grid indentation method even with an extremely large sample size, as demonstrated by the OPC 0.36 dataset. The study by Wilson et al. does not account for the possibility of additional structural compliance, however. This study is the first to methodically do so with the OPC 0.5 sample. Prior to compliance filtering, the statistical analysis cannot infer any separate clusters in the OPC 0.5 dataset ( $k=1$ ). The mean is 30.65 GPa, coincidentally in the range often reported for HD C-S-H [102]. As by design of the experiment and supported by the microstructural model, the lack of unhydrated clinker in the sample likely plays a role in the results of a singular phase. The automated self-similarity filter may have also eliminated phases strongly influenced by remnant clinker particles.

When compliance filtering is applied to the OPC 0.5 sample, the range of the dataset is narrowed further. The filter discarded all indents with moduli  $<30$  GPa. A possible explanation could be that the tests were too greatly influenced by porosity and therefore

did not satisfy continuity. This supports the assumption made earlier to neglect the differentiation of low and high density C-S-H products in the model, based on similar findings previously made by Davydov et al. [23]. Two clusters centered around 34 and 44 GPa are proposed in this GMM. These moduli likely correlate to C-S-H and CH phases respectively (with the possibility of the CH phase being intermingled [14, 102]) considering their dominant presence in the microstructure, as observed in the model image of Fig. 2.20. Although the posteriors of the cluster assignments are quite high (Fig. 2.16), a complimentary method like quantitative SEM-EDS would still be necessary to confirm these phase assignments [102].

While complimentary microscopic analyses are useful for determining the indented phases, especially for OPC [53, 102], the underlying microstructure is not observed. This literal oversight was emphasized by the 3D FID-nt analysis and discussion from Trtik, Lura, and Münch [49, 90]. The results of the CSM indented OPC 0.5 sample demonstrate that only 5% of grid indents can be considered continuous. The yield of this test is not efficient or impressive, but it does show that grid indentation can be used to obtain reliable moduli values for OPC. The caveat here is that porous phases and relatively stronger and less prominent phase like clinker are discarded from the dataset, and only the most voluminous phases are retained and reported. Conveniently, the reliably measured phases of grid indentation of OPC were found to correspond to the main hydration products that are often of interest. In this way, the argument made by Ulm et al. for the presence of continuous volumes of hydration products in OPC microstructures is proven to be true to a limited extent [94]. Statistical nanoindentation with preprocessed results based on CSM data could be a viable method for assessing the properties of the dominant C-S-H/CH phases in OPC.

## 2.5 Conclusions

When analyzing unfiltered high speed nanoindentation data, erroneous clusters with no clear phase assignment were observed. This is likely due to additional sources of structural compliance from the heterogeneous microstructure, effectively proving that a larger sample size does not necessarily improve the accuracy or “signal-to-noise” ratio of the results. The belief based clustering method is unbiased and has no method for identifying erroneous clusters. Hence, it is necessary to ensure that only valid indentation data is being input to the statistical analysis. The results of this study generally suggest that the “noise” and wide data range observed in statistical nanoindentation results [48] are likely associated with indentation tests not conforming to the assumption of continuum mechanics.

By filtering the grid indentation results for self-similarity in an automated fashion, the statistical nanoindentation method was shown to provide reasonable and useful results for Al-Si ceramic samples. No clear phase distinction was provided for the OPC 0.5 sample at this filter level. To a certain extent of microstructure heterogeneity and phase contrast, the Gaussian distributions applied to prospective phases in statistical nanoindentation may accommodate for the influence of the microstructure. This would explain the original validation of the method. With the modifications of automated data pre-processing and belief-based clustering algorithms, the original statistical nanoindentation method appears to be valid for the Al-Si samples while hydration products could not be discerned in the OPC 0.5 sample. This method may be suitable for discerning phases of substantially different moduli if the phase(s) of interest is not notably effected by compliance.

Clearer distinctions of phases/clusters was achieved by further filtering of datasets to eliminate tests affected by additional sources of structural compliance. The complexity of the Al-Si and OPC microstructures examined in this study yielded less than 10% of performed indents after this filter. The low sample size remaining therefore diminishes the significance of the results, although “noise” (i.e. discontinuous tests) is eliminated.

However, separate phases of hydration products were successfully suggested for the OPC

0.5 sample after this additional filter and the clarity of phase distinctions in the Al-Si samples improved slightly.

In order to obtain reliable phase properties, even larger arrays of indents are recommended for future work if compliance filtering is to be performed. Both filter stages were also observed to present some bias against lower moduli values, where porosity may have been present. Phases with higher moduli relative to neighboring phases were also observed to be subject to bias in the data filters. All of the limitations discussed in this paper should be considered before performing statistical nanoindentation for a composite material.

## CHAPTER 3

### QUALITY ASSESSMENT OF GEOPOLYMERS USING THE FORMATION FACTOR

#### 3.1 Introduction

According to the study by Heath et al., geopolymers produced from calcined clays can result in 40% less CO<sub>2</sub> emissions compared to ordinary portland cement (OPC), though other environmental impacts of geopolymer production may increase relative to OPC [35]. Commercial adoption of geopolymer based “E-Crete<sup>TM</sup>” in Australia has demonstrated the feasibility of geopolymer binders for reducing the CO<sub>2</sub> footprint of concrete [95]. However, there is no standardized test method specifically designed to evaluate the durability of these alternative cements, which limits their implementation [95].

Durability concerns for geopolymers in concrete include the possibility of efflorescence or subflorescence [104, 105], carbonation [68], and the ingress of chloride ions for reinforced concrete applications. The diffusivity of ions in the saturated microstructure can be seen as a common enabler of these possible degradation mechanisms [54, 64, 105]. A method of quantifying this diffusivity of ions, as well as the availability of excess alkali ions in geopolymer microstructures can provide useful insight into the durability and overall quality of the material.

The diffusivity is a function of the porosity of the microstructure and can be interpreted from the flow of electrical current [32]. Derived from Archie’s law, the formation factor describes a fundamental material property of non-conductive porous

media saturated with a conductive fluid [81]. The formation factor,  $F$ , can be calculated from the following equation,

$$F = \frac{\rho}{\rho_o} = \frac{1}{\phi\beta} \quad (3.1)$$

where  $\rho$  is the effective bulk resistivity,  $\rho_o$  is the pore solution resistivity,  $\phi$  is the volume fraction of saturated porosity, and  $\beta$  is a connectivity factor describing the “tortuosity” of the pore network [32]. These components of the formation factor measurement are illustrated in Fig. 3.1.

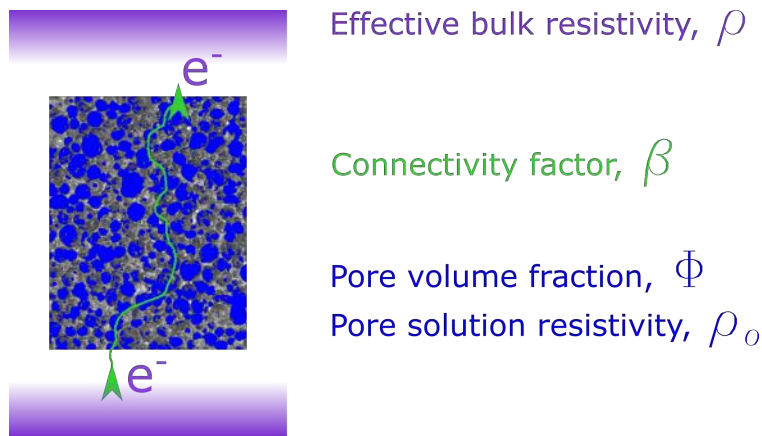


Figure 3.1: Illustration of formation factor components for a saturated porous microstructure.

In this study, a method for determining the formation factor of geopolymers is presented. The method requires measuring the bulk resistivity of a geopolymer specimen in a saturated condition while simultaneously knowing the pore solution resistivity. The concern of pore solution alkalinity leaching during saturation in solution must be addressed in this process since it can dramatically influence formation factor measurement [46, 82].

Contrary to OPC systems, the sodium or potassium aluminosilicate hydrate (N-A-S-H or K-A-S-H) reaction products in geopolymers based on low calcium precursors such as metakaolin or class F fly ash do not directly incorporate water into the molecular structure and instead confine it to the pore solution [66, 100]. The geopolymer pore solution is of high alkalinity, with comparable initial pH to that of OPC [46]. The pore solution

alkalinity of cement is conventionally determined through a pore water extraction method where cement samples are compressed at high-pressures to express the pore solution followed by chemical analysis of the extracted solution [5]. However, Lloyd et al. found that pore water extraction may lead to underestimation of the alkali content of low-Ca geopolymer pore solutions [46].

A likely explanation for why the pore water extraction method underestimates the alkali concentration in geopolymer pore solutions is because of alkali binding. Nuclear magnetic resonance (NMR) studies of Na and K ions in geopolymers indicate that aqueous alkali ions can be weakly bound to the aluminosilicate matrix in disordered configurations [73, 79]. Yet long-term leaching studies report that these weakly bound alkali are capable of diffusing [61], which suggests that they can also contribute to the bulk electrical measurement of a saturated geopolymer specimen. Therefore, a leaching procedure may be more appropriate for quantifying the alkali ions in geopolymer pore solutions that influence the electrical properties.

In this study, the ions assumed to be capable of conducting electricity through the pore solution are referred to as free alkalis. The free alkalis are to be quantified using a leaching procedure in order to estimate the pore solution conductivity and calculate the formation factor. Allahverdi et al. recently proposed a convenient leaching procedure for determining the free alkali content of geopolymers [1]. However, the work presented by Allahverdi et al. offered no information on the determination or effectiveness of their proposed leaching procedure [1]. Hence, the first part of this study explores different aspects of alkali leaching in geopolymers in order to determine an improved procedure for measuring all free alkalis.

Once a reliable method for measuring free alkalis is obtained, the formation factor measurement becomes feasible. Specimens can be saturated in a known volume of water so that the concentration of alkalis leached can be determined at the time of resistivity measurement. The average internal alkali concentration and temperature during the bulk

resistivity measurement can then be used to calculate the conductivity of the pore solution [77]. The objective of this study is a formation factor method that can quantitatively describe the microstructure of geopolymers. The accuracy of this quantitative method can be gauged to some degree by qualitative observations from microscopy [12].

## 3.2 Methodology

### 3.2.1 Specimen preparation

Metakaolin geopolymers were prepared with input molar ratios of 2.5, 0.9, and 15 for Si/Al,  $M$ /Al, and H/ $M$  (where  $M$  is Na or K). Both K and Na mixtures were produced with these ratios. The activator solutions were prepared 24 hours prior to mixing to allow equilibrium and ambient temperature to be reached. Due to limited workability, vibration was used to enhance the mixing of metakaolin with the activator solution. Cylinders 52 mm in diameter and 102 mm in height were cast and consolidated using vibration as well. The specimens rested until 90 minutes after initial mixing and were then placed in either 60°C or 80°C ovens for 48 or 24 hours respectively. Isothermal calorimetry performed at 20°C (Fig. 3.2) suggested that these durations could provide effectively complete polycondensation of the geopolymers. Moreover, the higher curing temperatures further accelerate the reaction processes [52].

Table 3.1: Mixture compositions by weight fraction of constituents.

$M$	Metakaolin	$M$ -Silicate Solution	Anhydrous $M$ -OH	Additional H <sub>2</sub> O	Curing Temperatures (°C)
Na	0.40	0.20	0.11	0.29	60, 80
K	0.39	0.36	0.07	0.18	60, 80

Table 3.2: Metakaolin composition from manufacturer.

Oxide	% wt.
SiO <sub>2</sub>	51.0 - 52.4
Al <sub>2</sub> O <sub>3</sub>	42.1 - 44.3
Fe <sub>2</sub> O <sub>3</sub>	0.30 - 0.50
TiO <sub>2</sub>	1.56 - 2.50

Table 3.3: Composition of silicate solutions.

<i>M</i>	SiO <sub>2</sub>	Na <sub>2</sub> O	H <sub>2</sub> O
Na	0.29	0.09	0.62
K	0.24	0.15	0.61

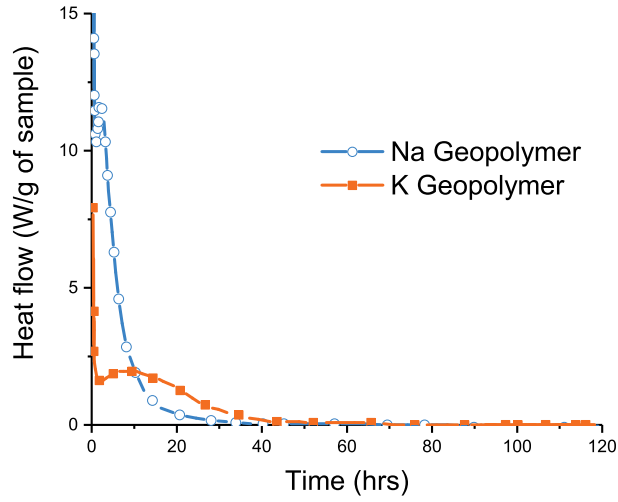


Figure 3.2: Isothermal calorimetry of Na and K mixtures at 20°C. Initial dissolution peak was not fully measured.

### 3.2.2 Measuring free alkalinity

#### Titration

An acid-base titration procedure was used to analyze the alkalinity of samples throughout this study. While Allahverdi et al. used 0.1 N HCl and phenolphthalein as an indicator to perform the acid-base titration [1], the present study uses 0.05 M HCl and methyl orange as an indicator. The lower concentration titrant was chosen to improve precision, along

with a Grade A buret. The slightly acidic endpoint determined using the methyl orange indicator ensures that all of the alkalis present are quantified, regardless of whether carbonation occurs [24].

### **Factors influencing free alkali leaching**

The method proposed by Allahverdi et al. was used as a starting point to develop an improved leaching procedure. First, the choice of deionised water or ethylene glycol as a solvent was considered. Then other factors such as particle size, leaching time, solvent volume, and solvent temperature were evaluated. Based on the results of these trials, a revised method was designed.

### **Geopolymer specific leaching procedure**

In the improved method resulting from the prior section, 1g of dry crushed paste sample passing a 150  $\mu\text{m}$  sieve is weighed to the nearest 0.0001 g as  $w$ . The sample is stirred (using a magnetic stir bar) in 40 mL of deionized water for 20 min at a temperature of 60°C in a sealed flask. The filter apparatus is comprised of a buchner funnel with filter paper and a vacuum line attached to the flask below. Prior to adding the sample, the filter paper is wetted with exactly 10 mL of deionized water. The entire leaching solution is then poured over the filter to remove the sample particles. The volume of filtrate  $V_f$  is recorded before 5 mL of the filtrate is precision pipetted into a flask for titration along with a sufficient amount of deionized water (approximately 30 mL) and methyl orange indicator (2-3 drops). The pipetted volume,  $V_p$ , can be increased for samples with lower free alkali contents to maintain accurate titration measurements. The total volume of acid consumed during titration is recorded as  $V_a$ . The concentration of acid should be calibrated and recorded as  $C_{HCl}$  prior to testing. The free alkalinity,  $n$ , in mol/g of crushed dry sample is calculated using Eq. 3.2.

$$n = \frac{C_{HCl} \times V_a \times \frac{V_f}{V_p} \times \frac{40mL}{V_f - 10mL} \times \frac{1L}{1000mL}}{w} \quad (3.2)$$

By accounting for any solution retained on the sample or filter paper, Eq. 3.2 provides additional precision in calculating the leached alkali in solution prior to filtering. For clarity, this procedure is referred to as the geopolymer (GP) hot water extraction (HWE) method since there are several other HWE methods used for OPC that use different parameters [67].

### **Comparison to the Espresso Method**

The espresso leaching procedure was originally proposed by Fournier et al. for determining the pore solution alkalinity of OPC specimens [30]. A recent review of pore solution measurement techniques for OPC suggests that the espresso method is highly repeatable regardless of initial sample water content, unlike pore water extraction that requires a sufficient volume of pore water [67]. This attribute is desirable for geopolymers, which can contain limited pore water in an in-situ state [66]. The GP HWE method, designed specifically for geopolymers following section 3.2.2, was compared to the following adaptation of the espresso method in order to determine if the espresso method is also suitable for geopolymers.

The implementation of the espresso method used in this study was modified slightly to accommodate a smaller sample of cement paste, rather than a larger sample from concrete containing aggregate. Near 1.0000 g of dried particles <150  $\mu\text{m}$  were collected and weighed as  $w$ . The sample was then placed in the same filter setup as described earlier for the GP HWE method. A graduated cylinder was used to measure 80 ml of boiling deionized water which was then carefully poured over the sample in the filter apparatus. The use of the attached vacuum line was found to be necessary for the repeatability of this espresso procedure as was noted the original method as well [30]. The volume of filtrate,

$V_f$ , was then measured (in mL) before precision pipetting at least a 5 mL aliquot,  $V_p$ , for titration to determine the alkali concentration. Aliquots from both the espresso and GP HWE methods were also taken for analysis via inductively coupled plasma optical emission spectrometry (ICP-OES) to validate the titration results and method. The free alkali content,  $n$ , in mol/g of dry sample is calculated from titration by Eq. 3.3.

$$n = \frac{C_{HCl} \times V_a \times \frac{V_f}{V_p} \times \frac{1L}{1000mL}}{w} \quad (3.3)$$

### 3.2.3 Measuring formation factor

#### **Bulk resistivity: $\rho$**

After demoulding specimens, 5-10mm thick slices of the 52 mm diameter cylinders were slowly cut using a diamond grinding blade. The thin specimen geometry was found necessary to mitigate cracking during saturation. The specimens were then saturated in 100 mL of deionized water by keeping them in a chamber above 95% vacuum for at least 3 hours, which was found to be long enough for air bubbles to cease emerging from the specimens-signifying complete saturation. Specimens remained saturated for 18-24 hours to allow for the pore solution alkalinity to decrease and approach an equilibrium with the storage solution. Specimens were removed from storage solutions, and the geometry, mass, and temperature were recorded immediately prior to impedance measurement. The bulk impedance of specimens was measured using an HP 4194A AC Impedance Analyzer and two stainless steel plate electrodes with sponges saturated in a sodium hydroxide solution, as shown in Fig. 3.3. Only the resistance at 1 kHz was used for further calculations since this is the frequency used by certain commercial products designed for analyzing concrete. It was especially necessary to subtract the resistance of the sponges from the bulk measurement due to the low resistance of the relatively thin geopolymer paste specimens [84]. The bulk resistivity,  $\rho$ , was calculated from the bulk impedance measurement using the geometric correction factor  $k = \frac{A}{L}$ , where  $A$  and  $L$  are the cross-sectional area and

length of the specimen respectively [83].

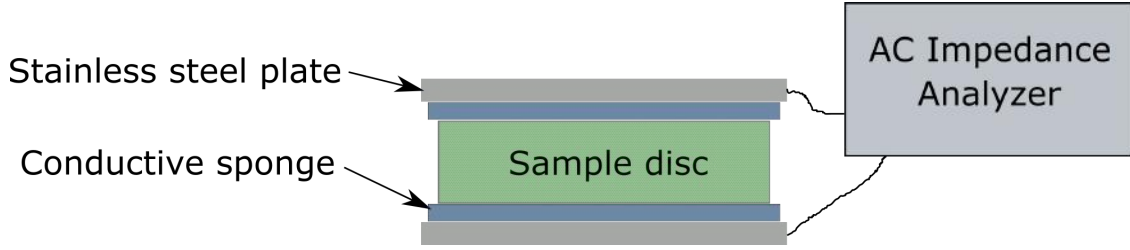


Figure 3.3: Setup for measuring the effective bulk resistivity.

### Pore solution resistivity: $\rho_o$

In order to determine the pore solution resistivity at the time of bulk sample measurement, the average pore solution concentration was determined from the initial free alkalinity of the geopolymer and the alkalinity of the storage solution in which the bulk sample was saturated. This approach is illustrated in the schematic of Fig. 3.4 and is mathematically represented by Eq. 3.4 and 3.5. First, the espresso leaching procedure described earlier and in [30] was employed to determine the initial free alkalinity inside the sample,  $n_i$ , of the geopolymers. Following sample removal and measurements, the alkali concentration of the storage solution,  $C_{out}$ , was determined using the titration procedure described earlier. The moles of alkali leached during sample saturation and storage,  $n_{out}$ , can then be calculated as,

$$n_{out} = C_{out}V_c \quad (3.4)$$

Where  $V_c$  is the final volume of solution in the storage container. The average pore solution concentration at the time of bulk impedance measurement,  $C_{avg}$ , is then calculated from Eq. 3.5 as,

$$C_{avg} = \frac{n_i - n_{out}}{V_{pore}} \quad (3.5)$$

Where  $V_{pore}$  is the total volume of porosity, as determined from the mass of water evaporated from the fully saturated sample upon drying at 60°C until no change in mass was observed.

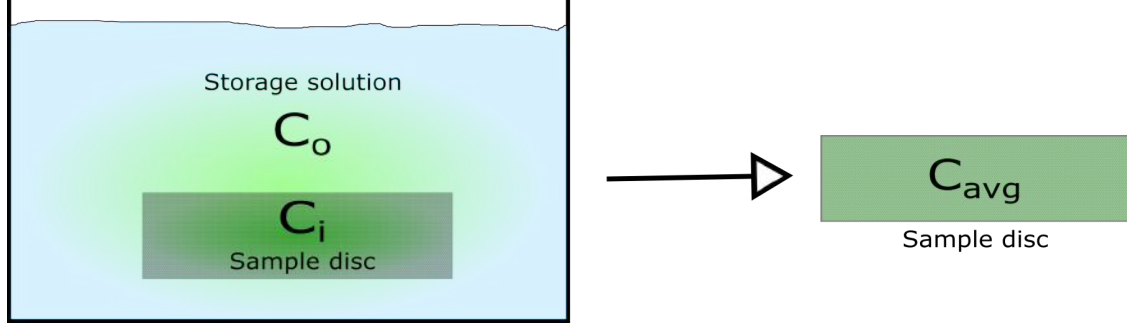


Figure 3.4: Schematic of the method used to account for alkali leaching.

The model from Shcherbakov and Artekima [77], based mainly on the experimental data gathered by Gilliam et al. [33], was used to calculate the pore solution conductivity based on the measured temperature,  $T$ , and concentration,  $C_{avg}$ , pertaining to the bulk impedance measurement. Following the work of Shcherbakov and Artekima [77], the maximum electrical conductivity in S/cm,  $\kappa_{max}$ , for a given temperature can be calculated along with the corresponding concentration,  $C_{max}$ , using the following equations:

$$\begin{aligned} \text{KOH: } C_{max} &= 5.16 + 4.04 \times 10^{-2}T - 2.64 \times 10^{-8}T^4 + 1.28 \times 10^{-12}T^6 \\ \text{NaOH: } C_{max} &= 3.68 + 4.04 \times 10^{-2}T - 2.64 \times 10^{-8}T^4 + 1.28 \times 10^{-12}T^6 \end{aligned} \quad (3.6)$$

$$\begin{aligned} \text{KOH: } \kappa_{max} &= 0.370 + 8.50 \times 10^{-3}T + 7.94 \times 10^{-5}T^2 - 4.27 \times 10^{-7}T^3 + 1.27 \times 10^{-9}T^4 \\ \text{NaOH: } \kappa_{max} &= 0.176 + 8.50 \times 10^{-3}T + 7.94 \times 10^{-5}T^2 - 4.27 \times 10^{-7}T^3 + 1.27 \times 10^{-9}T^4 \end{aligned} \quad (3.7)$$

For this study, the concentration of interest is  $C_{avg}$  so  $C = C_{avg}$ . The values of concentration,  $C$ , normalized by  $C_{max}$  can accurately predict the electrical conductivity,  $\kappa$

through the following relationship [77],

$$\frac{\kappa}{\kappa_{max}} = 2.38 \left( \frac{C}{C_{max}} \right) - 1.76 \left( \frac{C}{C_{max}} \right)^2 + 0.37 \left( \frac{C}{C_{max}} \right)^3 \quad (3.8)$$

This relationship is valid for concentrations greater than 0.1 M [77]. The electrical conductivity,  $\kappa$ , is then converted from S/cm to the pore solution resistivity,  $\rho_o$  in  $\Omega/m$ .

This approach is a viable alternative to the algorithms based on ionic strength that are conventionally used to estimate pore solution resistivity of concrete [80], especially since the systems investigated in this study include either K or Na almost exclusively in the pore solution. Due to the high alkalinity of geopolymer pore solutions, the electrical impedance is greatly affected by temperature as Melar et al. previously observed [50]. The model from [77] provides an advantage over the ionic strength calculation by inherently accounting for temperature. The model eliminates the need for an additional temperature correction that requires assumed or experimentally determined coefficients to describe the temperature dependence of the electrical measurement [20].

Moreover, the calculation of solution conductivity based only on the ionic strength does not account for the experimental bounds of conductivity (Fig. 3.5) because a viscosity factor was not included in the calculation. This could be an issue for geopolymers with pore solution concentrations approaching the respective concentration of potassium or sodium that yields the maximum conductivity ( $C/C_{max} = 1$  in Fig. 3.5). Although the low-Ca geopolymers investigated in this study did not contain such high pore solution concentrations based on free alkali leaching, this phenomenon may be present for geopolymers (or other alkali-activated materials) with precursors containing higher Ca content (e.g. slag) since they have been found to have significantly higher alkalinity pore solutions because of preferential incorporation of Ca ions [46].

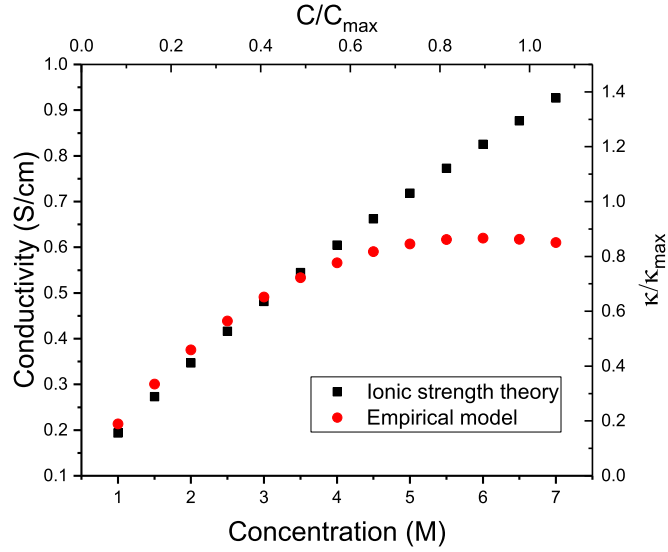


Figure 3.5: Comparison of pore solution conductivity calculation based on ionic strength [80] or the empirical model [77]

### 3.2.4 Complimentary characterization

#### Ultrasonic pulse velocity

To estimate the in-situ strength of each geopolymer type, the ultrasonic pulse velocity (UPV) of end-cut cylinders from each type was measured using Pundit Lab+ (Proceq) equipment. Cylinder ends were cut with a diamond grinding blade to provide a flat contact surface.

#### Scanning electron microscopy

Small fracture specimens were obtained from the dried disc specimens previously used for the formation factor measurement. A 10 nm layer of gold was sputtered onto the surface to prevent charging during scanning electron microscopy (SEM) [7]. The fracture surfaces of each geopolymer type were observed in a ThermoScientific Apreos SEM with an accelerating voltage of 20 keV.

### 3.3 Results and Discussion

#### 3.3.1 Free alkali measurement

The objective of this part of the study was to determine a suitable leaching procedure for measuring the free, readily leachable alkali content of a geopolymer to be used later in estimating the pore solution concentration. The method proposed by Allahverdi et al. [1] was used as a starting point from which the optimization of different aspects were investigated. Sodium geopolymer cured at 60°C was used for this section since more free alkali ions may be observed for sodium than potassium [46].

The method used by Allahverdi et al. used ethylene glycol as a solvent at ambient temperature. To investigate the effect of the solvent type and temperature, the use of deionized water as a leaching solvent was compared to ethylene glycol at temperatures of 20°C, 40°C, and 60°C, and the results are shown in Fig. 3.6. It is clear that using deionized water and a temperature of 60°C offers a significant increase in leached alkalis during the 15 min duration. Based on these results, deionized water was selected as an alternative solvent since it is more economical and effective. Because of these advantages, deionized water is also a common solvent in leaching methods used for OPC [67]. Following the results presented in Fig. 3.6, 60°C was selected as the temperature since higher temperatures lead to excessive evaporation during the leaching duration.

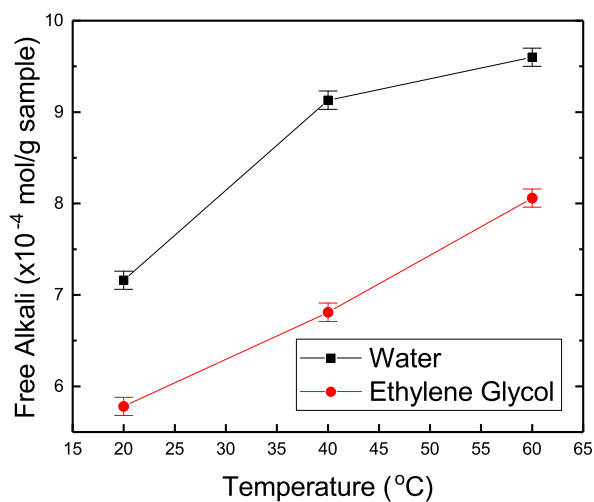


Figure 3.6: Comparison of water and ethylene glycol as solvents for alkali leaching at various temperatures. The particle size, volume of solvent, and leaching time were <90 micron, 20 mL, and 15 min., respectively, as in the method proposed by [1]. Error bars denote variability associated with the titration method.

The volume of solvent used was investigated next. Figure 3.7 displays the results of leaching performed with 20 mL, 40 mL, and 60 mL volumes for a full 60 minutes. In Fig. 3.7, 60 mL is seen to increase the leached alkali content by an insignificant amount. Considering the results of long term leaching studies [61, 79] that found alkalis to continually leach until near exhaustion if provided replenished volumes of deionized water, it is preferable to limit the volume in this case in order to prevent excessive leaching of alkalis that are more incorporated in the aluminosilicate matrix of the geopolymer. These more incorporated alkalis would not likely be in an aqueous, or free, state during the electrical measurement of the bulk specimen later in this study and should be measured as so in the HWE method.

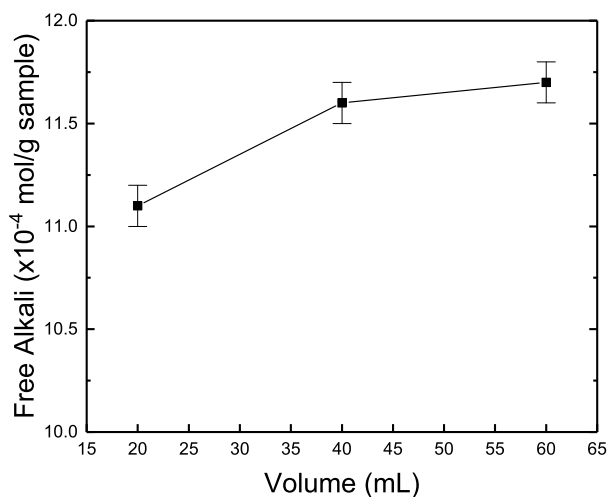


Figure 3.7: Free alkali measured for different volumes of water as a solvent. The leaching temperature was  $60^{\circ}\text{C}$  and the leaching time was 60 min. for this set of tests with a particle size passing a 90 micron sieve. Error bars denote variability associated with the titration method.

The influence of particle size and leaching time were also examined and the results are shown in Fig. 3.8. Samples that were crushed to a particle size less than  $90\ \mu\text{m}$  exhibit greater variability. This could be attributed to the fact that the entirety of a sample is extremely difficult to pulverize to such a fine particle size using only a mortar and pestle. Therefore the finer sample may not be as representative. With the  $90\text{-}150\ \mu\text{m}$  particle size samples, there appears to be only marginal increases in leaching past 20 min. From these results, it was determined that 20 min. of leaching is sufficient for a sample with particle sizes  $<150\ \mu\text{m}$ . This gradation also agrees with the espresso method [30] investigated next.

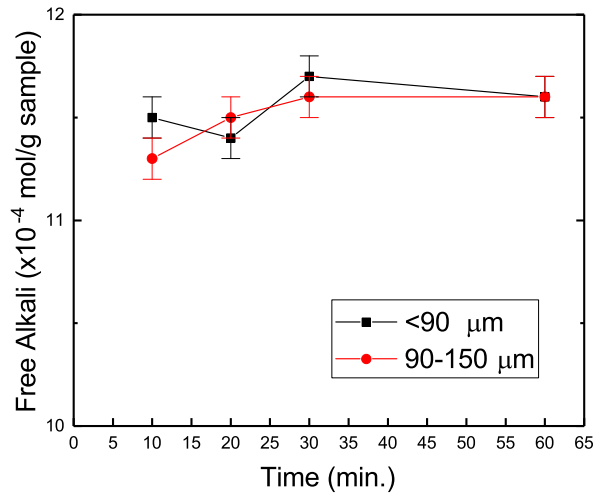


Figure 3.8: Free alkali measurement with different particle sizes and leaching durations. Leaching was performed in 60°C deionized water. Error bars denote variability associated with the titration method.

The GP HWE method designed specifically for geopolymers from the preceding trials was compared to an adaptation of the espresso method previously developed for OPC by Fournier et al. [30]. The titration technique was also compared to the use of ICP in this experiment. Both methods of measuring the alkali concentration, titration and ICP-OES, found the GP HWE method to yield slightly more alkalis with less variability observed in the titration results (Fig. 3.9). The titration method was observed to measure slightly more alkalis as well. This overestimation could be due to the choice of methyl orange as an indicator since the titration endpoint observed may be slightly past equilibrium [24].

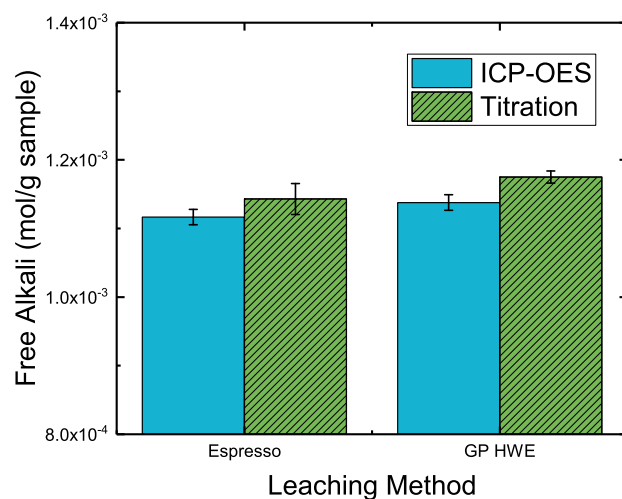


Figure 3.9: Comparison of ICP-OES and titration measurements of free alkalis using GP HWE and espresso methods.

Figure 3.10 shows the various trace elements leached from the geopolymer in each method as according to ICP-OES. The more rapid espresso method appears to effectively mitigate the leaching of Si and Al ions in addition to the free alkalis. This is a considerable advantage of the espresso method, and the lesser leaching of alkalis could also be considered advantageous in avoiding the leaching of otherwise bound alkalis. Minimal leaching of elements other than alkalis in the espresso method further supports the decision to use only the titration measurement in the remainder of this study. For these reasons the espresso method was selected to be used in the proceeding formation factor method.

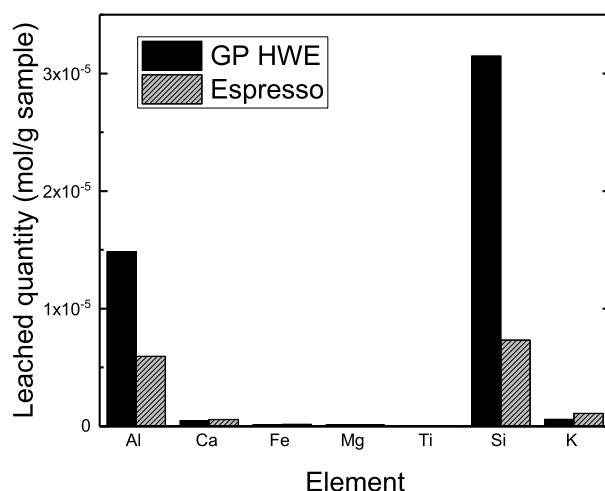


Figure 3.10: Trace elements quantified by ICP-OES for GP HWE and espresso leaching methods.

### 3.3.2 Formation factor measurement

In estimating the pore solution conductivity, the free alkalinity of each geopolymer type was determined using the espresso method. Figure 3.11 shows the different levels of free alkalinity observed between geopolymer types. Both mixtures used in this study included the same molar dosages of either sodium or potassium. As observed in previous studies [46], potassium exhibited greater levels of incorporation in the geopolymer matrix compared to sodium. The 80°C curing temperature may also lead to greater alkali incorporation when compared to the samples cured at 60°C, which would agree with previous studies [105]. However, the difference observed between the results of different curing temperatures is not significant.

According to the quality control method proposed by Allahverdi et al. [1], the free alkalinity demonstrates a direct correlation to the compressive strength of geopolymers. By this logic, the geopolymers examined here should yield the following ranking of strength from highest to lowest: K80, K60, Na80, Na60. However, the study by Rovanić suggests that 80°C curing should in fact decrease the strength of metakaolin based geopolymers compared to 60°C curing [72]. Furthermore, the work of Zhang et al. suggests

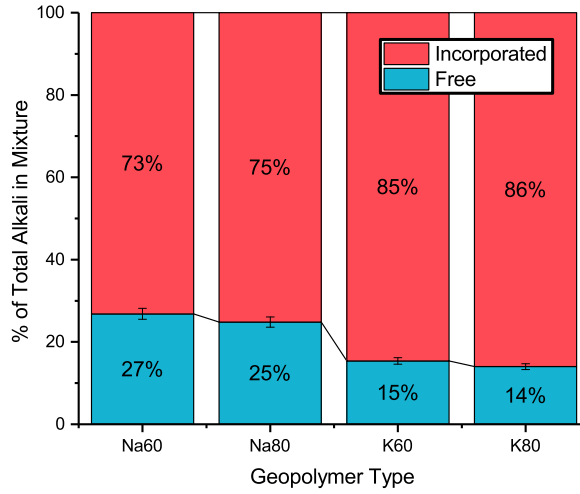


Figure 3.11: Free alkali content of geopolymers as determined by the espresso method.

that the use of sodium as an alkali cation can produce geopolymers of higher strength than potassium [103]. The free alkali content alone may not describe the quality of any given geopolymer.

The free alkalinity was used to calculate the formation factor, which can provide a more holistic understanding of the material microstructure [99]. Figure 3.12 displays the formation factors of each geopolymer type in a fully saturated state with the effects of alkali leaching and temperature accounted for as described in the methods section. The opposite trend is observed relative to the free alkali measurements, with the sodium geopolymers and 60°C curing temperature resulting in higher formation factors that indicate decreased connectivity of the porous network (i.e.  $\beta$ , Table 3.4).

Table 3.4: Summary of data from formation factor calculation.

Sample	$C_i$ (M)	$C_{avg}$ (M)	$\phi$	$F$	$\beta$
Na60	$1.36 \pm 0.07$	$0.62 \pm 0.05$	$0.44 \pm 0.04$	$55.04 \pm 5.51$	$0.0427 \pm 0.0070$
Na80	$1.26 \pm 0.00$	$0.49 \pm 0.04$	$0.49 \pm 0.03$	$43.23 \pm 2.96$	$0.0477 \pm 0.0007$
K60	$0.65 \pm 0.02$	$0.35 \pm 0.04$	$0.42 \pm 0.02$	$30.58 \pm 1.43$	$0.0778 \pm 0.0076$
K80	$0.55 \pm 0.01$	$0.26 \pm 0.02$	$0.42 \pm 0.02$	$23.03 \pm 1.03$	$0.1048 \pm 0.0083$

For reference, the formation factors calculated without correcting for the leaching of

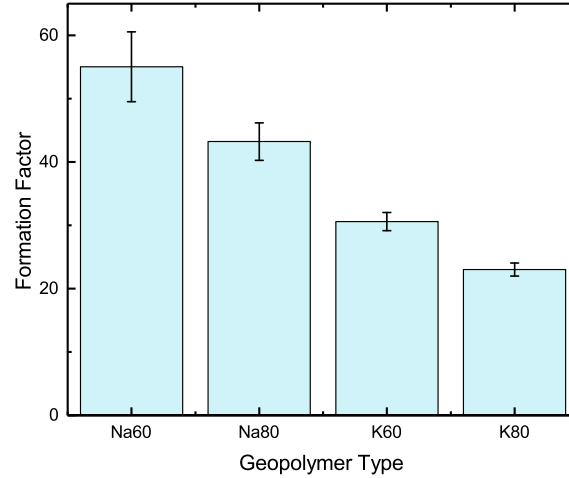


Figure 3.12: Formation factor measurements for fully saturated geopolymer pastes. Pore solution, leaching, and temperature were accounted for.

alkalis (i.e.  $C = C_i$ ) during saturation and storage is shown in Fig. 3.13. The formation factor nearly doubles for each of the samples, and the variability of results increases for the 60°C cured samples that contained higher free alkali contents. Spragg et al. previously demonstrated the significant effect that leaching can have on the formation factor measurement [82], which is also seen here in Fig. 3.13. This observation suggests that the method to account for alkali leaching presented in this study is highly effective.

Compared to the formation factor values reported for concrete in literature [99], the values calculated for the low-Ca geopolymers of this study are extremely low. This is easily attributed to the lack of aggregates in the paste samples used here, as well as the porosity that comprises at least 40% of the sample volume (Table 3.4). The formation factor reported for Indiana sandstone ( $F = 55.2 \pm 1.6$ ) is more comparable to the geopolymer results [82]. However, accounting for the approximate 12% pore volume of the sandstone yields a pore connectivity factor of  $\beta = 0.18$ , which is higher than the values of  $\beta$  shown in Table 3.4 for the geopolymers samples. The  $\beta$  values found for the geopolymers of this study are more similar to those reported for enhanced porosity concretes [58]. This comparison might suggest that the geopolymer microstructure is quite

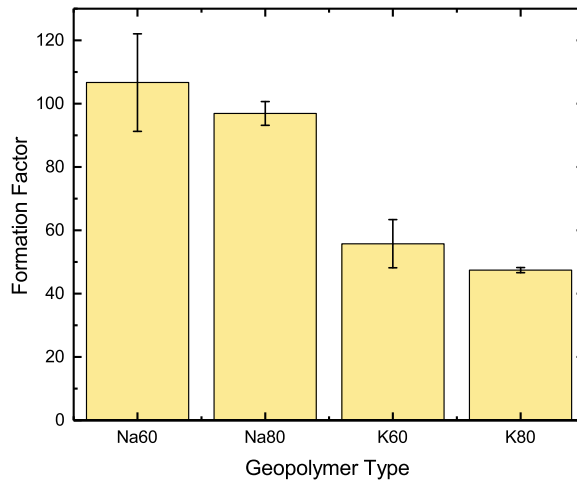


Figure 3.13: Formation factors calculated without accounting for alkali leaching during saturation and storage.

interconnected, but the scale of the pores is not necessarily comparable to that of enhanced porosity concrete. Further work is likely needed to provide more practical context and validation for the formation factor values determined in this study.

### 3.3.3 Complimentary characterization

#### UPV analysis

For comparison to the formation factor, UPV was used to assess the quality of each geopolymer type since it is also influenced by the porosity of the microstructure. UPV is also non-destructive in nature, which enables more precise results for a single sample than destructive mechanical testing since repeated readings can be taken. Denser microstructures, with more solid mass for the pulse waves to travel through, result in higher UPV values. A denser microstructure could also be assumed to increase the formation factor by decreasing the porosity or pore network connectivity. UPV measurements have been shown to correlate well with the compressive strengths of geopolymer concrete [62].

The UPV results shown in Fig. 3.14 corroborate well with the formation factor results.

These results also agree with the literature regarding the effect of curing temperatures and choice of sodium or potassium solutions on the strength of metakaolin based geopolymers [72, 103]. The results of the UPV analysis provide further evidence that the free alkali content alone cannot indicate the quality of a given geopolymer.

The greater variability seen for the Na80 samples is likely due to imperfections such as entrapped air voids in the cylinder sample as a result of limited workability during casting. The microstructure evaluated by the formation factor in thinner samples was not noticeably affected by these larger scale imperfections.

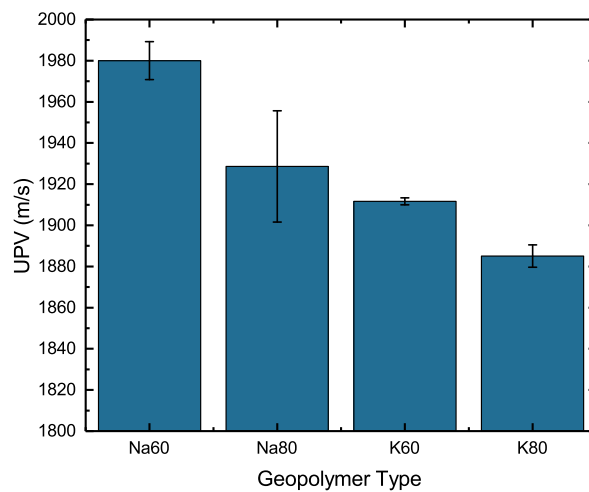


Figure 3.14: UPV measurements for in-situ geopolymer samples (sealed until preparation and testing).

### SEM characterization

Because the formation factor is a microstructural parameter, SEM microscopy should be able to qualitatively observe significant changes in the formation factor between samples. In the lower magnification images shown in Fig. 3.15, it is difficult to distinguish differences in the porous microstructures of each sample because of the variable fracture surface morphology. At this level, all of the samples display a similar granular texture. The sodium geopolymer samples appear to have more entrapped air bubbles than their

potassium counterparts possibly because of the difference in workability and flow during casting. When saturated, the entrapped voids would likely decrease the formation factor measurement. However, the formation factor of the sodium geopolymers was still found to be higher than the potassium geopolymers that appeared to have far less entrapped voids, Therefore, the influence of entrapped air bubbles may not have a significant effect on the formation factors measured in this study.

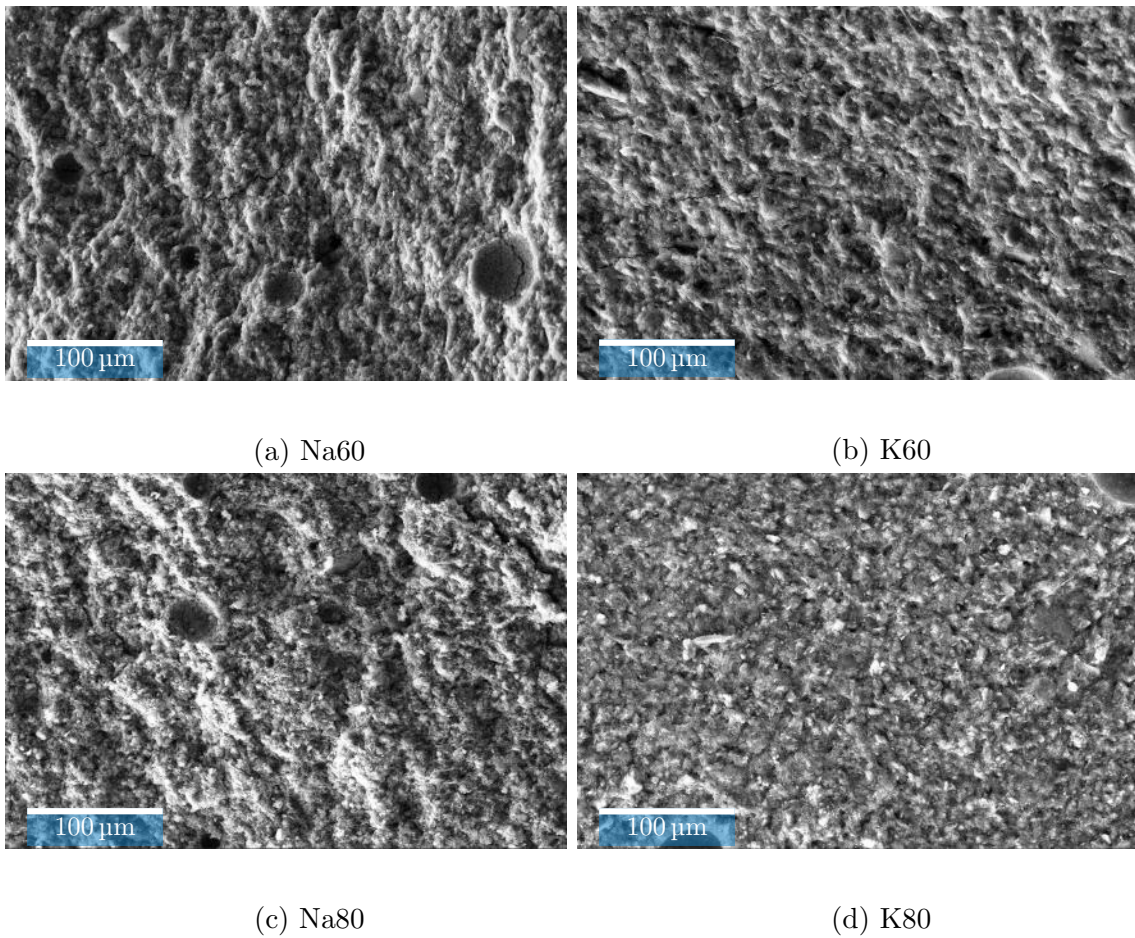


Figure 3.15: SEM micrographs of geopolymer fracture surfaces at 1,000x magnification.

When the microstructure is examined at 10,000x magnification, the sheet-like morphology of unreacted metakaolin particles becomes at least partially visible in all of the samples (Fig 3.16). Close examination of the images may also suggest that less dissolution occurred in the potassium geopolymers, which would agree with the reaction enthalpy measured previously (Fig. 3.2). However, no clear differences between the samples can be readily discerned. The fracture surface morphology may limit the interpretation of the images at this magnification as well.

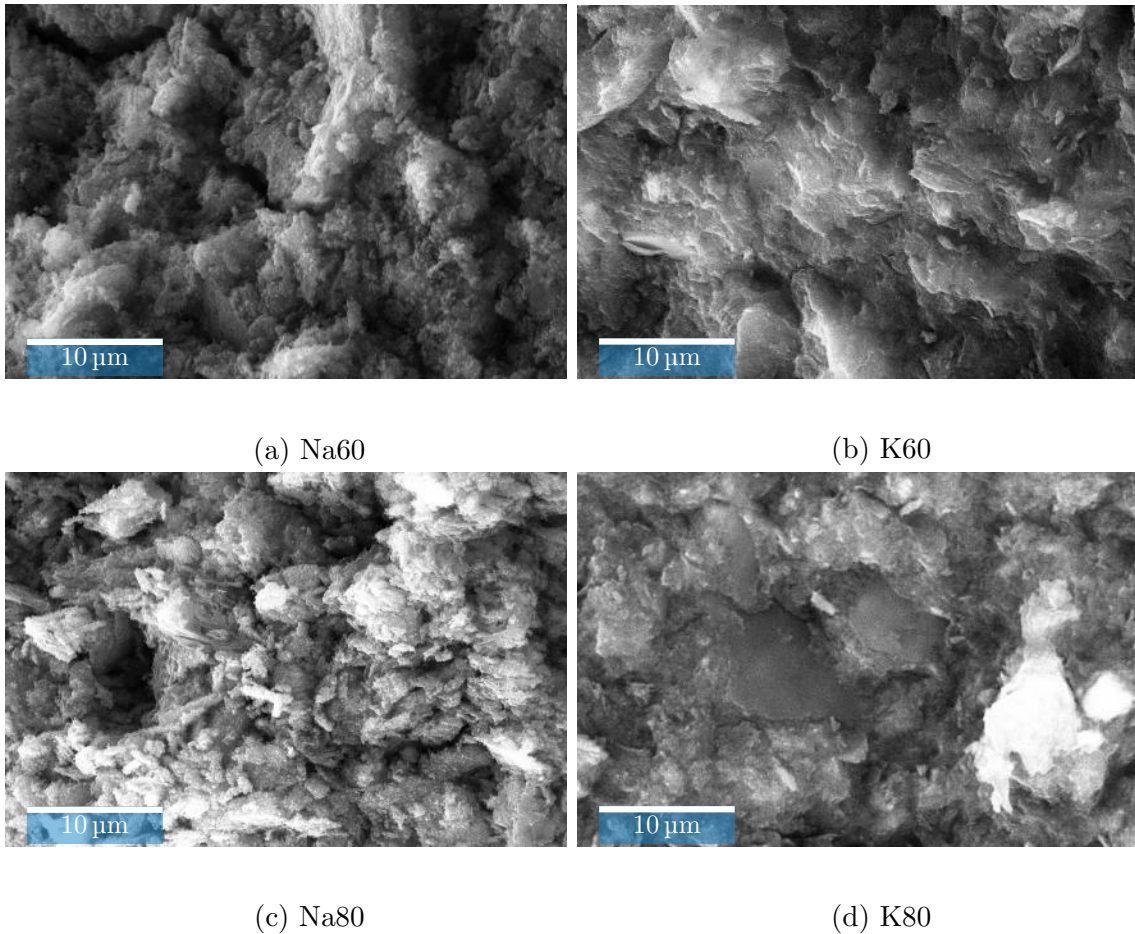


Figure 3.16: SEM micrographs of geopolymer fracture surfaces at 10,000x magnification.

The 100,000x magnification images shown in Fig. 3.17 reveal the micellar morphology that is characteristic of geopolymer reaction precipitates [7, 70]. There is a notable difference in precipitate size between the sodium and potassium geopolymers, which is confirmed by the quantitative image analysis reported in Fig. 3.18. The sodium geopolymers contain relatively large precipitates greater than 100 nm diameter. These precipitates are densely packed/agglomerated with minimal porosity observed between particles. In contrast, the potassium geopolymers display precipitates less than 100 nm across with frequent pore spaces between particles.

The difference between the nanoscale morphologies of the sodium and potassium geopolymers is shown at even higher magnification in Fig. 3.19. The additional porosity seen in the potassium geopolymer nanostructure is on the order of 10 - 50 nm. Moreover, previous transmission electron micrographs of geopolymers suggest that further nanoporosity may be present beyond the resolution of the SEM images obtained for the fracture surfaces in this study [47, 91]. Regardless, any interconnected nanoporosity would certainly influence the formation factor measurement. The increased nanoporosity observed for the potassium geopolymers relative to the sodium geopolymers in the SEM images directly correlates with the decrease in formation factor reported in Fig. 3.12 and Table 3.4.

It is difficult to interpret any significant change in the microstructures attributed to the different curing temperatures used, yet the precipitates of the 60°C samples may be slightly more agglomerated than the 80°C samples for the sodium geopolymer samples. The particle size distribution of the Na60 sample is skewed towards larger diameters since coalescent particles may have been measured as one. This finding would agree with the trend observed in the formation factor results. Although the difference between these samples quantified by the formation factor is not clearly represented in the SEM images, the SEM images do not necessarily disagree with the additional findings proposed by the formation factor measurements and supported in literature [72].

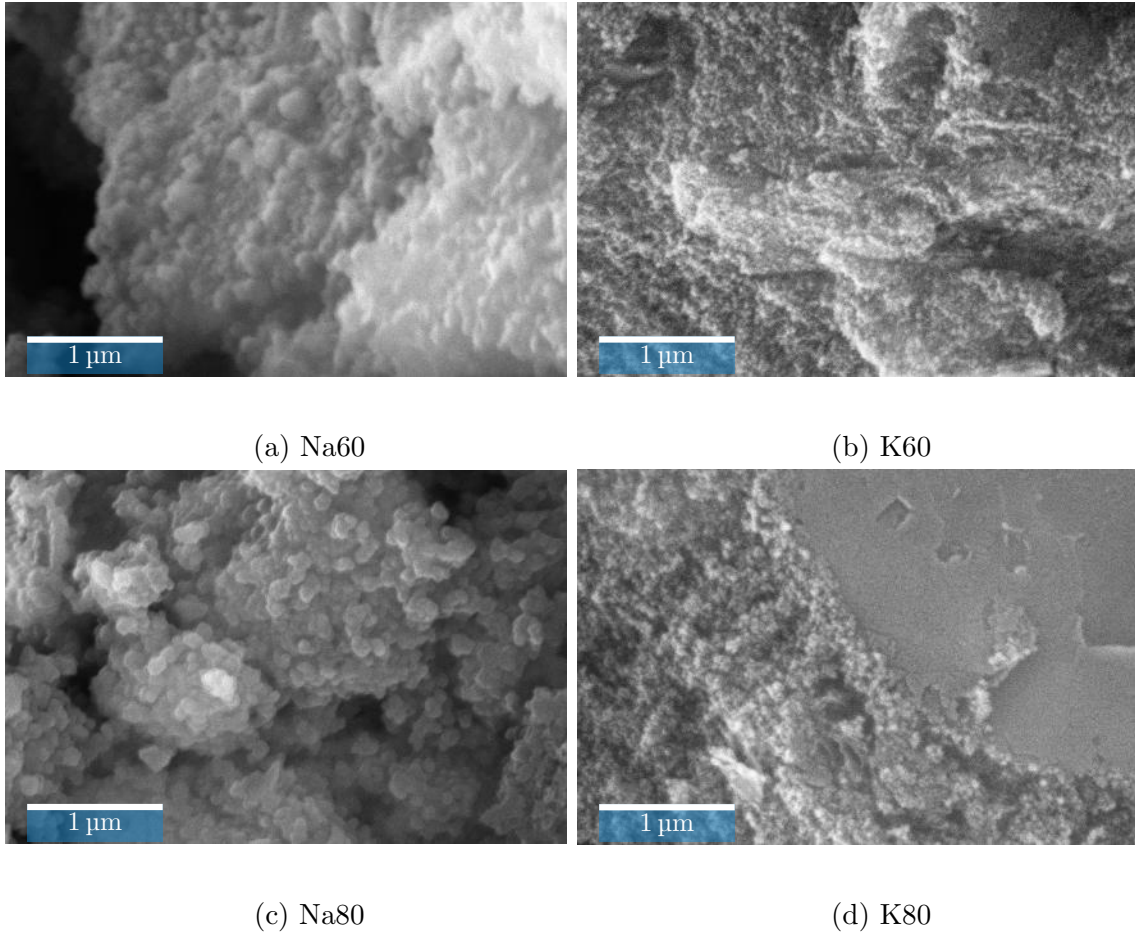


Figure 3.17: SEM micrographs of geopolymer fracture surfaces at 100,000x magnification.

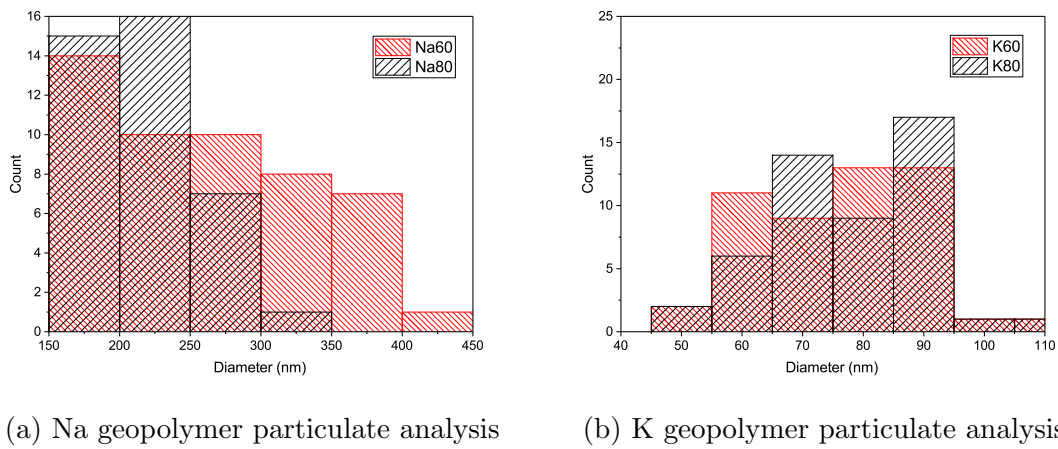
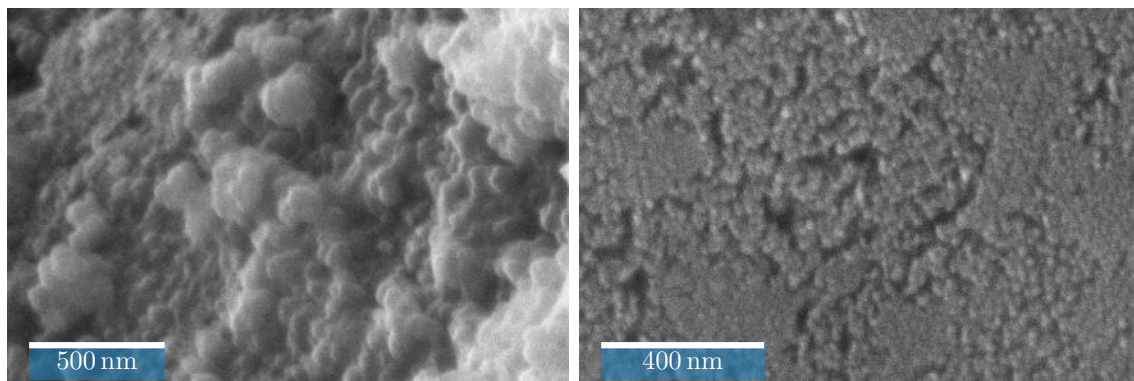


Figure 3.18: Histograms of the equivalent diameter of 50 particles in each image. The area of each particulate was measured in ImageJ using an oval geometry, which was then used to calculate the diameter assuming a circular geometry.



(a) Na60

(b) K60

Figure 3.19: High magnification SEM comparison of Na and K geopolymers.

### 3.4 Conclusions

The outcome of this study is a fully functional framework for formation factor measurement of geopolymers. The formation factor measurements corroborated well with both UPV measurements and the qualitative observations of the micro/nanostructure from SEM. This method has the immediate potential of quantitatively comparing the N-A-S-H or K-A-S-H microstructures of different geopolymers for the purpose of research and development. The method could also be more time and cost effective than the use of SEM in analyzing the microstructure of geopolymers with the possibility of greater nanoscale sensitivity.

Further validation is needed to determine the suitability of this method for accurately estimating the diffusion coefficient of either free alkalis from the geopolymer or chloride ions. Relating the results of this method to the overall durability and service life prediction of geopolymer concrete is also a subject for future work. The use of the espresso method for determining the pore solution conductivity is also worth investigating for OPC materials since it does not require preserved pore water contents and would make formation factor measurement more feasible for concrete specimens obtained from existing structures.

## CHAPTER 4

### THE EFFECT OF ELEVATED TEMPERATURE ON THE NANOSTRUCTURE OF A FLY ASH GEOPOLYMER

#### 4.1 Introduction

Geopolymers were previously characterized and popularized by Davidovits with the objective of commercializing a fire resistant textile [22], and many researchers have continued investigate the potential use of geopolymers for various applications. Rivera et al. recently demonstrated that superior thermal durability can be obtained for low-Ca geopolymer cements over ordinary portland cement (OPC) using X-ray computed microtomography ( $\mu$ CT) [71]. Furthermore, geopolymers are of interest as an extraterrestrial construction material [92]; an application that would also require resilience to a wide range of temperatures. The objective of the present study is to characterize the effect of elevated temperatures on the nanostructure of the fly ash geopolymer (FGP) concrete previously developed by Rivera et al [71].

##### 4.1.1 Geopolymer molecular structure

The molecular structure of geopolymers has been extensively characterized by solid-state nuclear magnetic resonance (NMR) studies [22, 26, 69, 73]. The reaction product in low-Ca geopolymers is an aluminosilicate framework of alternating silicon and aluminum tetrahedral units with a lack of long-range order [8, 69]. The alkali cations are generally thought to balance the charge of oxygen bridge sites between silicon and aluminum [22, 26, 69], act as network modifying agents at non-bridging oxygen (NBO) sites [25], and/or

remain weakly bonded in a concentrated pore solution [4, 8, 73, 79].

Syncrotron X-ray scattering pair distribution function (PDF) analysis confirms that the aluminosilicate matrix of a K-metakaolin geopolymer, similar to the K-FGP used in this study, is amorphous and contains chemically bound water in the form of potassium hydroxide [8]. Although the PDF method can determine the long-range atomic order, it is an average measurement of the structure and does not elucidate the chemical heterogeneity that has been observed on the nanoscale in FGPs using high-resolution nanoprobe x-ray fluorescence [69].

The recent use of atom probe tomography (APT) further elucidated the nanoscale heterogeneity of FGP [91]. Nanoscale distribution of Si and Al concentrations was resolved-disagreeing with the molecular model originally proposed by Davidovits, which consisted of uniform Si/Al ratios [22]. The morphology of high concentrations K clusters was also able to be visualized by using APT. The binding of K ions in the geopolymer matrix was previously proposed by Nguyen et al. [61], and agrees with the molecular model proposed for Na-geopolymers by Rowles et al. [73] shown in Fig. 4.1.

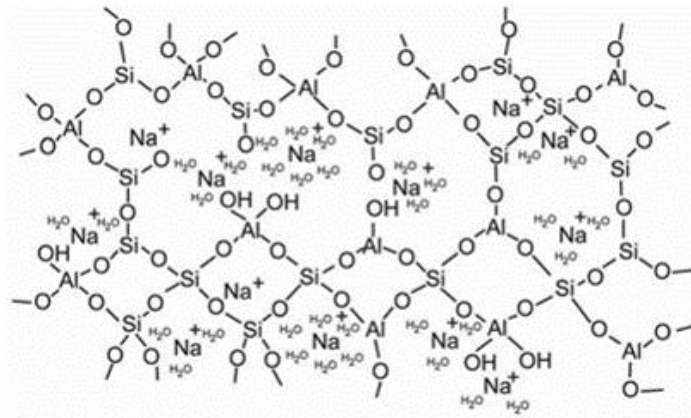


Figure 4.1: Schematic illustration Na-geopolymer molecular framework from [73]

Both X-ray and neutron scattering experiments report that temperatures below 300°C do not induce structural changes in the aluminosilicate molecular framework of geopolymers, since only dehydration occurs [8, 101]. While this is certainly true for the

overall structure probed by these methods, the nanoscale distributions of elements may be affected. In particular, the disordered and often hydrated environment of alkali cations (Fig. 4.1) is liable to evolve when the chemically bound water is evaporated. Moreover, this dehydration process was shown to increase the strength of the geopolymer as measured by nanoindentation [6].

#### 4.1.2 Atom probe tomography

Based on a previous study by Tuinukuafe et al. [91], further investigation using APT may help to elucidate the nanoscale changes that may occur in FGP during dehydration, particularly regarding the distribution of K ions. The APT process involves preparing a needle shaped specimen with an apex less than 100 nm in diameter using focused ion beam milling under a scanning electron microscope view (FIB-SEM) [42]. The SEM resolution in this process enables the larger heterogeneities of concrete such as unreacted cementitious products, aggregates, and porosity to be excluded from the extracted APT specimen.

The APT specimen is then placed in a local electrode atom probe (LEAP) where an ultra-fast laser pulse is used to excite the atoms at the apex of the specimen to incite field evaporation of the atoms towards a microchannel detector [42]. The time-of-flight (ToF) between the pulse and the detector impact is used to construct a ToF mass spectrum, from which the element present in the material can be ranged [42]. Using the ToF and the impact position of the microchannel detector, the ions of the specimen can be computationally reconstructed by making various geometric assumptions for the specimen and flight path [42]. Fig 4.2 shows an illustration of the APT process. The precision of the atomic reconstruction is difficult to estimate for amorphous materials like geopolymers since there is no crystalline lattice for reference. Therefore, complimentary techniques should be used to support any observations made in APT.

In this study, APT is utilized to examine the effect of elevated temperature on the nanoscale heterogeneity of an alkali aluminosilicate matrix comprising the reacted phase of

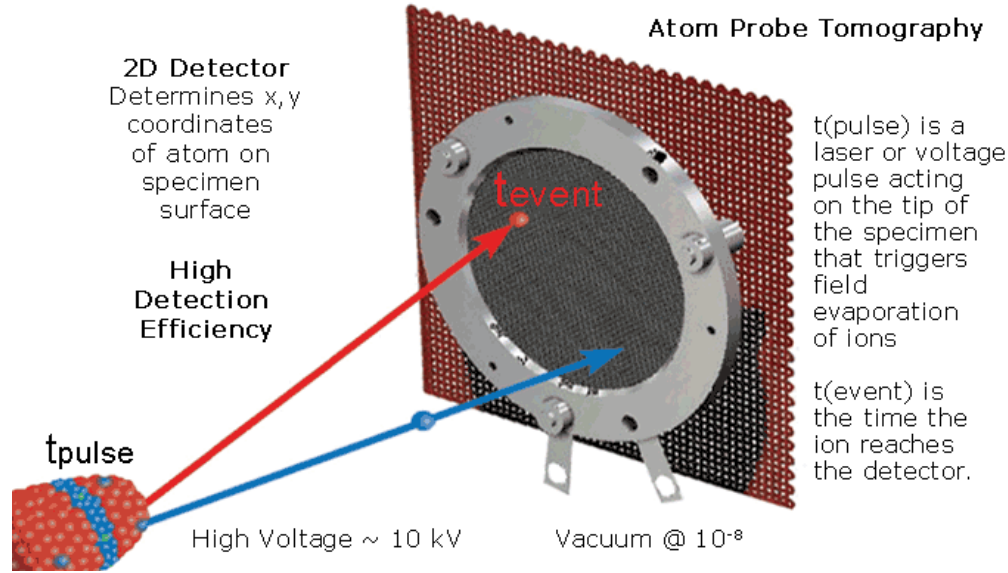


Figure 4.2: Schematic illustration of atom probe tomography technique (www.cameca.com).

a FGP. Complimentary leaching analysis to quantify the free alkalinity of the FGP after heating was also performed to support the APT findings. Statistical nanoindentation was used to evaluate the effect of temperature on the micromechanical properties of the FGP.

## 4.2 Methodology

The FGP specimens were cast previously by Rivera et al., where the methodology is described in full [71]. Table 4.1 shows the composition of the fly ash, which originated from the Bowen power plant (Euharlee, GA, USA). The activator solution was comprised of reagent grade potassium silicate and hydroxide. Following casting, the samples were sealed and cured at 23°C for 24 hours, then 40°C for 72 hours [71].

Table 4.1: Oxide composition of Bowen fly ash from XRF.

Oxide	SiO <sub>2</sub>	TiO <sub>2</sub>	Al <sub>2</sub> O <sub>3</sub>	Fe <sub>2</sub> O <sub>3</sub>	MgO	CaO	Na <sub>2</sub> O	K <sub>2</sub> O	P <sub>2</sub> O <sub>5</sub>	SO <sub>3</sub>	LOI
% wt.	53.74	1.4	28.26	6.66	0.91	1.38	0.35	2.1	0.26	0.08	3.58

In preparation for microscopy and nanoindentation, a small cylindrical core was sectioned from a larger 2x4 in. mortar specimen, and then cast in epoxy. The face of the

specimen was step-wise polished with 120, 400, 600, 800, and 1200 grit SiC paper followed by 6, 3, and 1  $\mu\text{m}$  diamond paste, and 0.3, and 0.05  $\mu\text{m}$  alumina suspensions in ethanol. Ethanol lubricant was used to mitigate possible leaching or reacting of FGP constituents [45]. The sample was rinsed and sonicated in ethanol following each polishing step as detailed in previous research [55].

#### **4.2.1 Atom probe tomography**

Atom probe samples were prepared using a FEI Quanta 200 3D Dual Beam FIB-SEM following the procedure outlined by Thompson et al. [89]. The SEM resolution available during this step allowed regions of dense reacted geopolymer paste to be identified in the heterogeneous FGP microstructure that often contains particles of unreacted fly ash [45]. The extracted samples were affixed to posts on a platinum APT sample coupon (36 post capacity) using platinum deposited in the FIB-SEM. The initial as-cast FGP atom probe tip specimens were sharpened using a TESCAN Lyra Dual Beam FIB-SEM using annual milling and a final 5 KeV “cleaning step”. APT was performed using a Cameca LEAP 5000XS at a temperature of 40K, a detection rate of 0.2%, and a laser voltage ranging from 30 to 50 pJ depending on tip geometry. The atom probe data was reconstructed and analyzed using the IVAS 3.8.0 software. Figures were reproduced in MATLAB for improved clarity.

Following the initial APT testing of several as-cast FGP specimens, the coupon containing the remainder of the APT specimens was subjected to the following heating regiment in atmosphere in an electric furnace: 30 minutes ramp heating to 200°C from 25°C, with no hold segment, and 30 minutes cooling to 25°C. The heat-exposed FGP APT specimens were then sharpened or re-sharpened before being tested in accordance with the LEAP procedure outlined above.

#### **4.2.2 Free alkalinity**

Previous experiments have demonstrated that the “espresso” hot water extraction (i.e. leaching) method originally proposed by Fournier et al. [30] is suitable for analyzing the

free alkalinity of geopolymers (Ch. 3). The espresso method used in this study was modified slightly to accommodate a smaller sample of cement mortar containing only fine quartz aggregate, rather than a larger sample from concrete containing coarse and fine aggregates of more variable mineralogy.

Samples were pulverized in a rotary mill, and near 2.0000 g of dried particles  $<150 \mu\text{m}$  were collected and weighed as  $w$ . The sample was then placed in a filter apparatus comprised of a buchner funnel with Whatman filter paper No. 1 and a vacuum line attached to the flask below. Prior to adding the sample, the filter paper was wetted with exactly 10 mL of deionized water. Deionized water was brought to a boil and then 80 mL was gradually poured over the sample in the filter apparatus. The volume of filtrate,  $V_f$ , was then measured (in mL) before precision pipetting at least a 5 mL aliquot,  $V_p$ , for titration to determine the alkali concentration. Titration was performed using 0.05 M HCl and methyl orange as an indicator as described in Ch. 3. The free alkali content,  $n$ , in mol/g of dry sample is calculated from titration by Eq. 4.1.

$$n = \frac{C_{HCl} \times V_a \times \frac{V_f}{V_p} \times \frac{1L}{1000mL}}{w} \quad (4.1)$$

This procedure was used to determine the free alkali content of FGP samples dried at  $60^\circ\text{C}$ , or soaked at  $200^\circ\text{C}$ ,  $400^\circ\text{C}$ ,  $600^\circ\text{C}$ ,  $800^\circ\text{C}$ , and  $1000^\circ\text{C}$  for 2 hrs.

### 4.2.3 Nanoindentation

The following nanonindentation procedure was used to characterize three specimens: an unheated FGP specimen, a specimen isothermally soaked at  $200^\circ\text{C}$  for two hours, and a core for a sample exposed to a butane flame for 10 minutes reaching  $650^\circ\text{C}$  in the previous study [71].

Nanoindentation was performed using an Agilent Technologies G200 Nanoindenter with a diamond Berkovich indenter tip. The Dynamic Contact Module II (DCM) load head was utilized for higher resolution of force. CSM indentation was performed with a harmonic

displacement target of 1 nm and a frequency of 75 Hz.

Indentations were conducted to a depth of 300 nm with 10  $\mu\text{m}$  indent spacing. Indent grids, 25 x 25, were performed for each sample, which covers a representative area for FGP materials according to previous multi-scale investigations [21].

The grid indentation data were then filtered for self-similarity as described in Ch. 2. Moduli values for the remaining indents were then calculated from the CSM data as an average between 100 and 200 nm, as done so in [21]. The data were then analyzed using the belief-based clustering approach based on maximum likelihood algorithms detailed in Ch. 2.

## 4.3 Results and Discussion

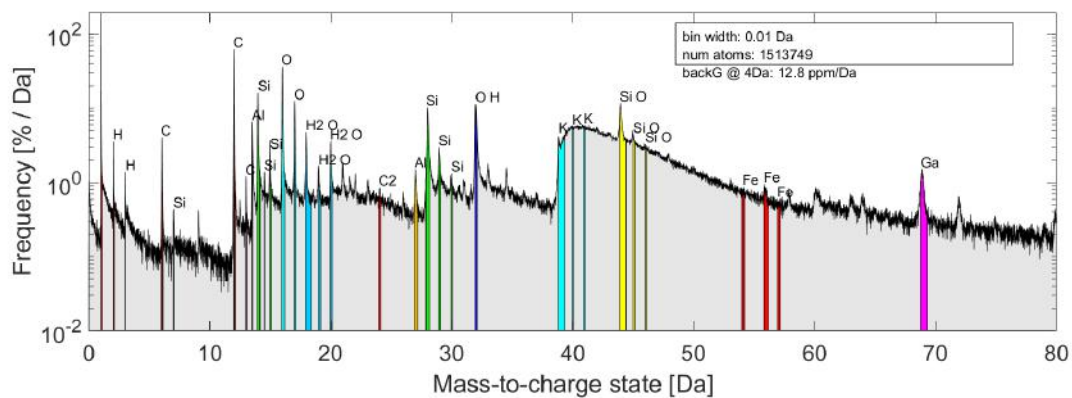
### 4.3.1 Atom probe tomography

Three successful APT sample runs of the unheated FGP were obtained and are referred to as R1-3. Three runs were also performed subsequently for the heated samples, denoted as R4-6. These selected samples were all found to represent reacted geopolymer phases based on their stoichiometry, which would be significantly different for unreacted fly ash phases [91]. Out of all of the APT tests on FGP samples (over ten including trials for configuring ideal run conditions), only one specimen was incidentally found to contain a nanoparticulate of unreacted fly ash and this sample was discussed in a prior publication [91]. This suggests that the FIB-SEM preparation procedure can reliably circumvent the larger heterogeneity of the FGP microstructure.

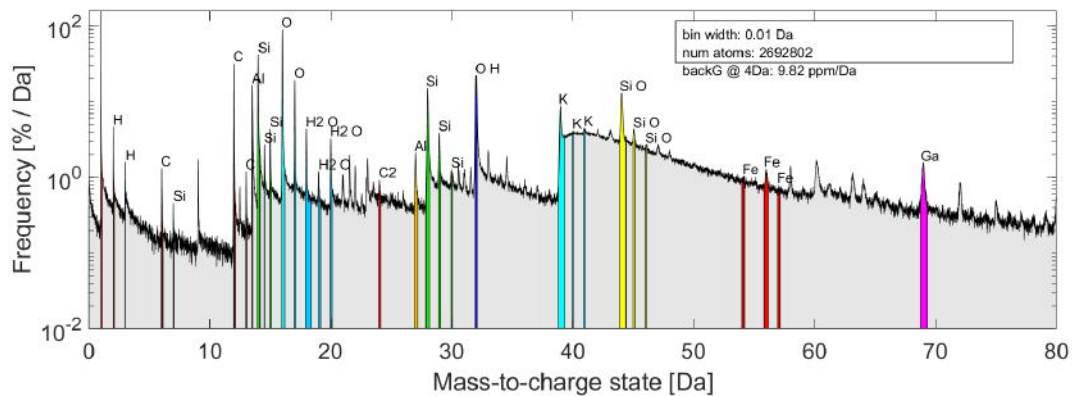
In an effort to eliminate possible variability between the geopolymer gel compositions [47] from influencing the results significantly, the remnants of the samples used in runs R1-3 following the heat treatment were attempted to be reused. The sample from R1 remained intact during the heat treatment process and was successfully resharpened and re-run as R4. The gel composition is less likely to change over the distance of less than 1  $\mu\text{m}$  between the locations of R1 and R4, compared to the runs performed on entirely

separate samples.

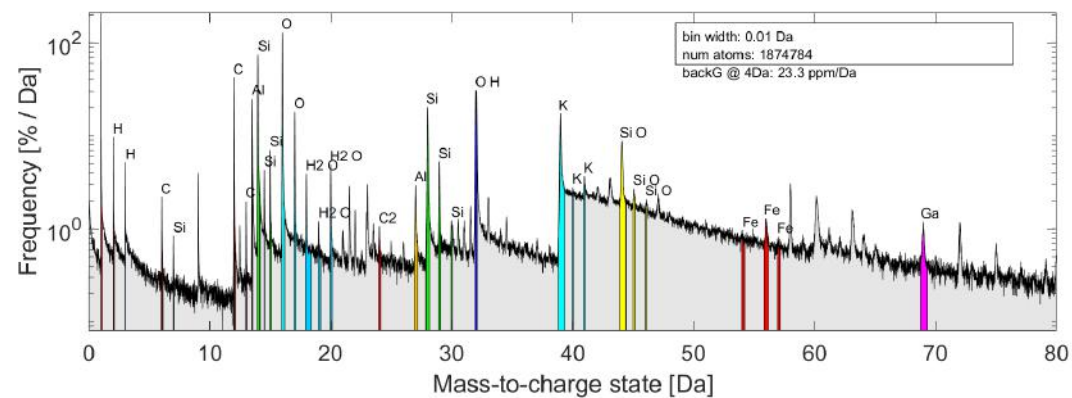
The ranged mass spectra used for 3D reconstruction of the unheated and heated APT data are shown in Fig. 4.3 and 4.4 respectively. The spectra of R1 and R2 show a slight hump after the peak at 39 Da assigned to K, which suggests that there was a heating artifact during the test run [42]. A wider flange tip angle was found to reduce the heating artifact observed in R1 and R2, providing a cleaner mass spectra for R3. Heating artifacts were not apparent in R4-6.



(a) R1

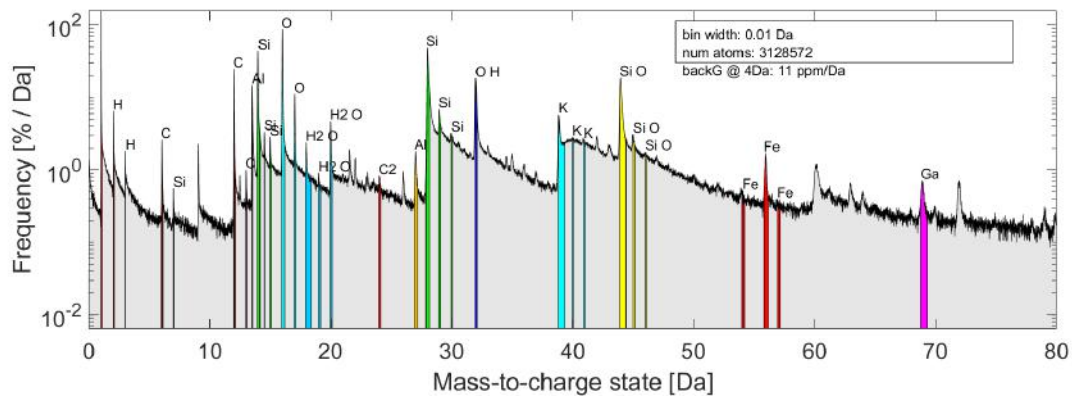


(b) R2

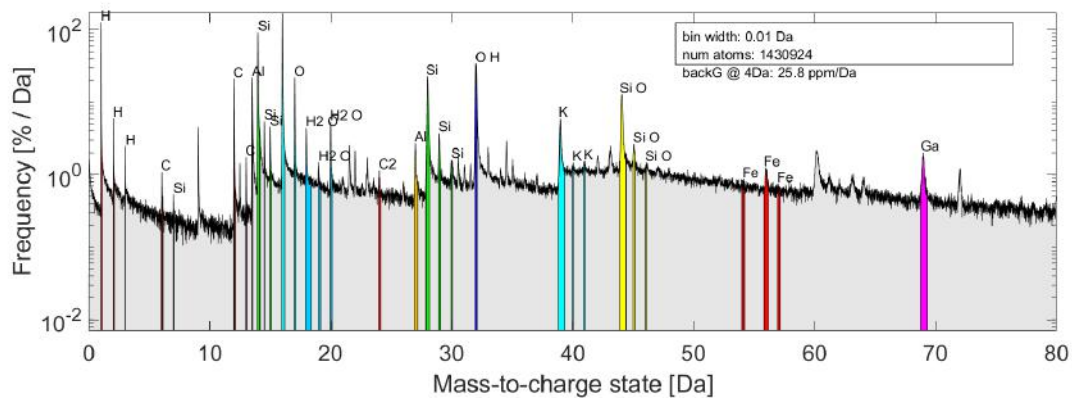


(c) R3

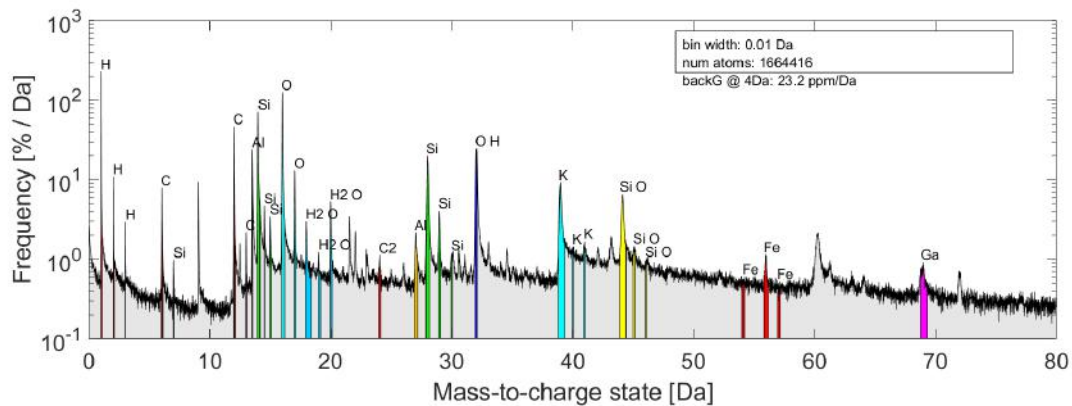
Figure 4.3: Mass spectra of unheated APT sample runs.



(a) R4



(b) R5



(c) R6

Figure 4.4: Mass spectra of heated APT sample runs.

To enable more quantitative analysis of the APT data, the 3D point cloud data was voxelized. The APT data volume was divided into 3 nm cubic voxels. This size voxel was found to provide a good balance between computation time and resolution. Smaller voxels might also contain an insufficient sampling of detected ions. The concentrations of Si, Al, and K in each voxel were calculated since these are the primary elements of the geopolymer gel (e.g. see Table 4.2).

Using the voxelized data, the distributions of K and Al concentrations throughout the samples can be evaluated in the histograms shown in Fig. 4.5. The histogram of K concentrations indicates that there is a difference between the K arrangements of the unheated and heated samples. The concentration of K in heated specimens appears to span 0-15% with a peak frequency between 2-5%. The K concentrations in the unheated samples is more broadly distributed up to 20% with most of the data lying above 5%. When the histogram of Al concentrations is examined, all of the samples indicate that Al concentrations are generally lower than 5%. This suggests that K ions may be more commonly in excess of Al in regions of the unheated samples.

To support this hypothesis, a histogram of the K/Al ratio of each voxel is also shown in Fig. 4.5. While the distribution of K/Al peaks around 1 for the heated samples, the unheated specimens are clearly skewed towards higher distributions. The predominant K/Al ratio of 1 in the heated specimens conforms to the theory that Si-Al tetrahedra bridge sites incorporate alkali cations in a charge balancing role [26]. The distribution of K/Al ratios in the heated samples sharply decreases around 3, suggesting that charge balancing is the primary role of K in these FGP samples with some deviation. From this it is inferred that in voxels where K/Al is greater than 3, that K is in excess. In other words, K is likely in an aqueous and disordered configuration above  $K/Al = 3$  in the voxelized APT data [27, 73].

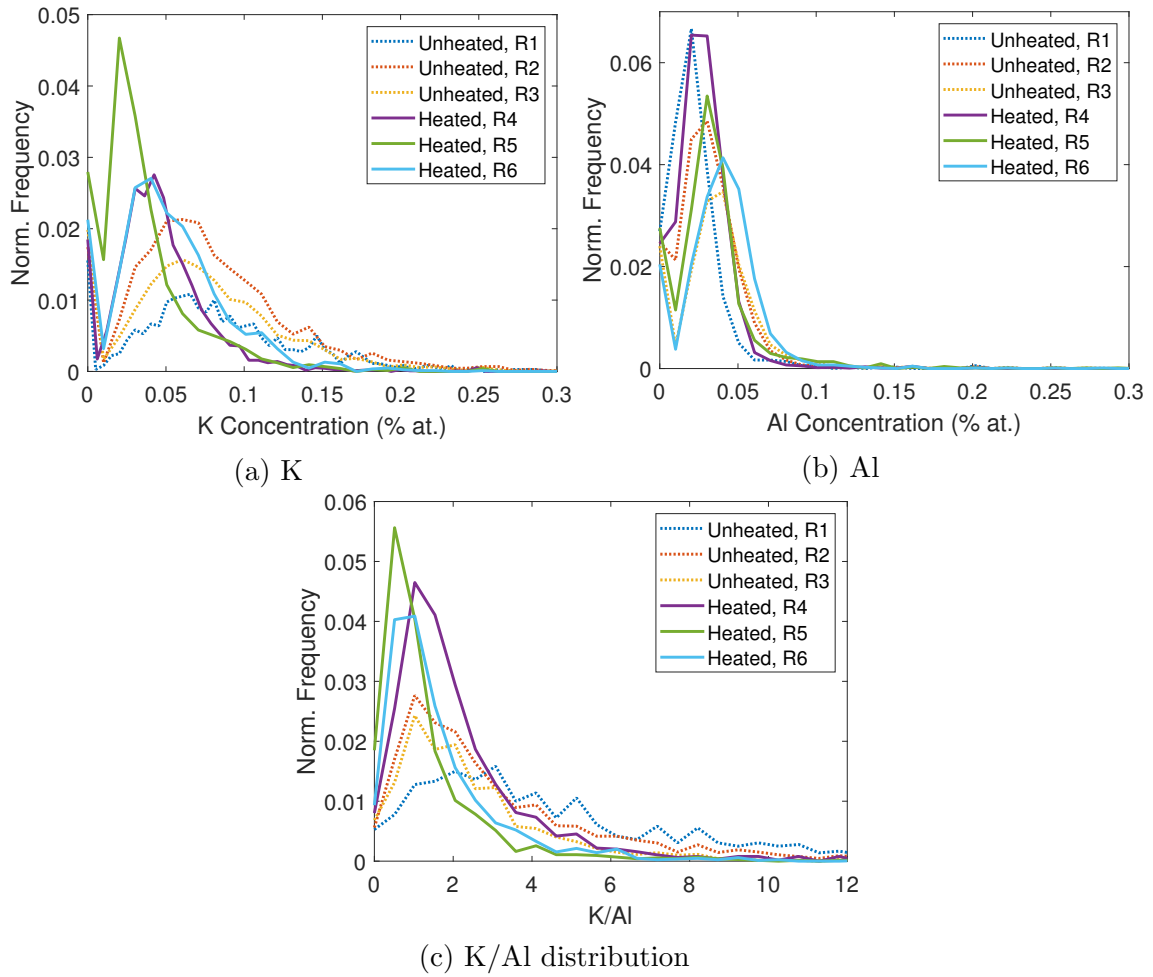
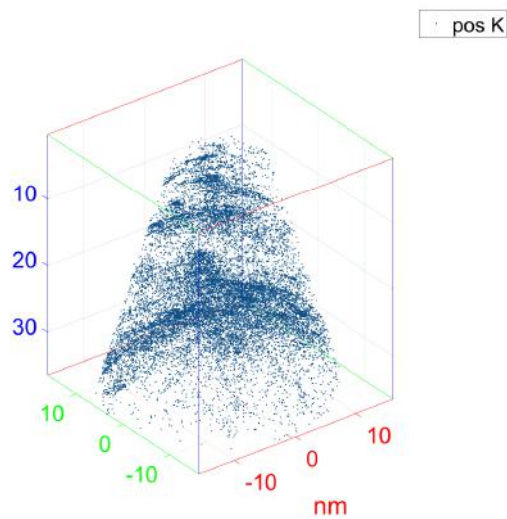
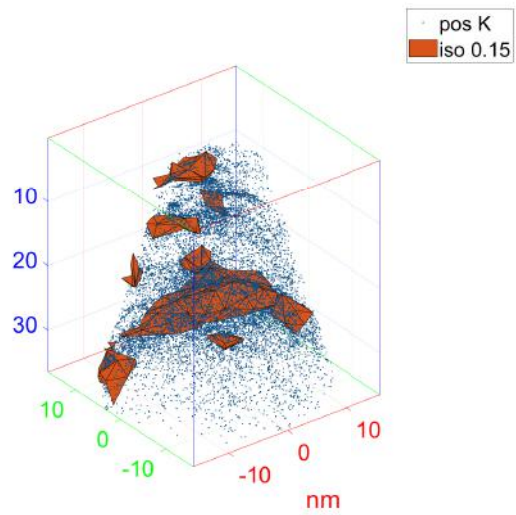


Figure 4.5: Histograms of K and Al concentrations throughout samples with a 3 nm voxel size.

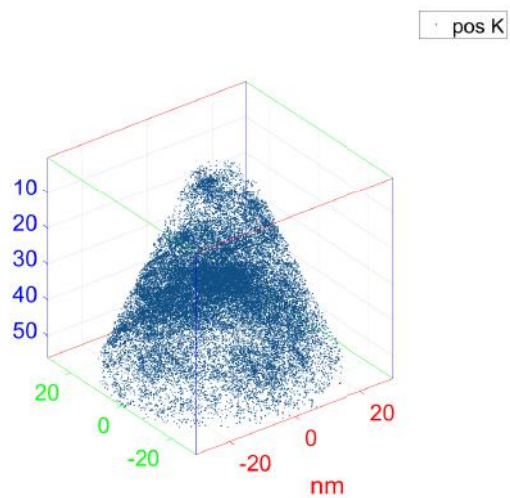
Based on the observation of Al concentrations generally below 5% and the conservative boundary of  $K/Al=3$  for excess K in the APT data, 15% was set as the threshold for isosurface analysis of the K concentrations throughout each sample. Figures 4.6 and 4.7 include the 3D reconstruction of the unheated APT sample data with only 40% of the detected K ions shown (for image clarity). The isosurfaces for regions with K concentrations above 15% are shown in a parallel figure for R1-3 (orange). The visibly denser clusters of K ions in the 3D APT point cloud data correlate well with the 15% isosurfaces identified through analyzing the voxelized data.



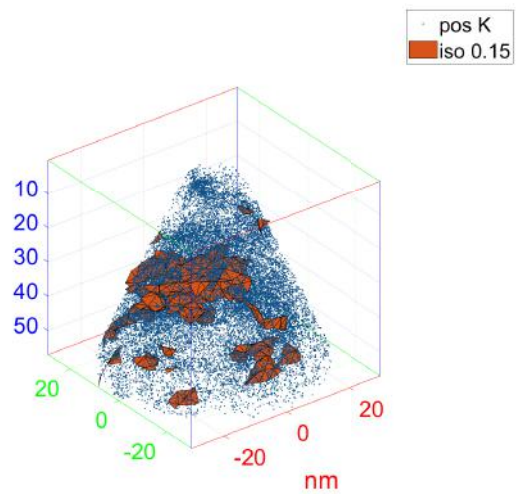
(a) R1 with K points only



(b) R1 with isosurfaces

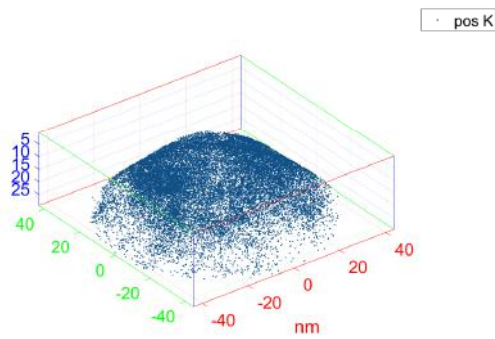


(c) R2 with K points only

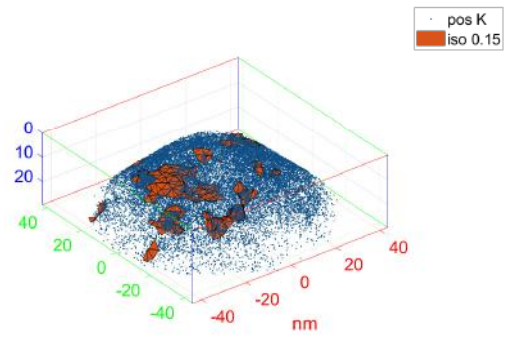


(d) R2 with isosurfaces

Figure 4.6: Cluster analysis of potassium in unheated samples.



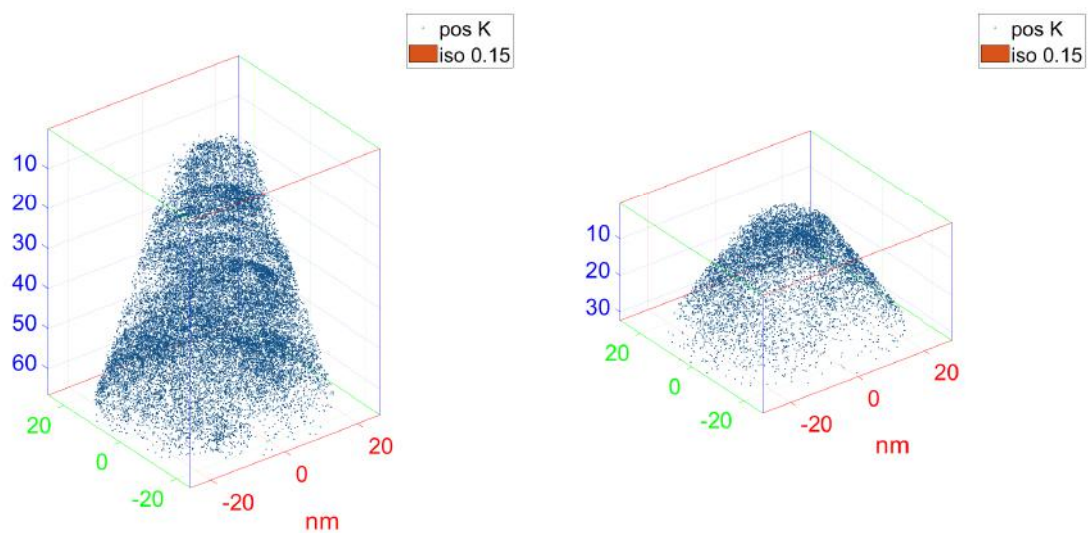
(a) R3 with K points only



(b) R3 with isosurfaces

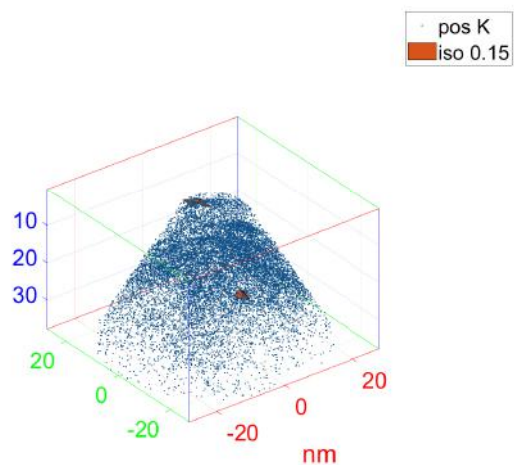
Figure 4.7: Cluster analysis of potassium in unheated samples.

The isosurface analysis for K concentrations above 15% was also performed for the heated APT samples. Fig. 4.8 shows the point cloud of 40% of the detected K ions along with the isosurfaces associated with concentrations above 15%. It is not necessary to show the images of only the K ions here, as they were in Fig. 4.6 and 4.7, since there are no substantial isosurfaces observed. The K ions appear to be evenly distributed throughout the heated samples without clustering. This indicates that there was negligible excess K in the heated samples.



(a) R4

(b) R5



(c) R6

Figure 4.8: Cluster analysis of potassium in heated samples.

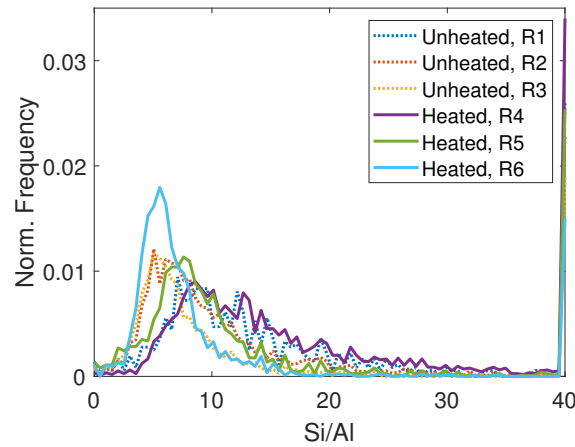
It seems possible that this difference between the unheated and heated samples could be due to the heating artifact observed in the mass spectra of the runs, rather than an actual material transformation. However, the observation of K clusters in R3 suggests that the clustering was not caused by the heating artifact observed in the mass spectra of R1

and R2. The heating artifact is likely associated with the presence of clusters though, since alkalis may not be strongly bonded in the geopolymer molecular framework [79]. Because of their weak bonds the K ions are liable to field evaporate in the LEAP with less energy than the aluminosilicate matrix requires. The weakly bonded K ions in the material may have in fact promoted the heating artifact by evaporating due to the residual heat of pulses designated for atoms in the layer above them (in the z-direction of the tip profile). If this theory is correct, then the heating artifact observed in the mass spectra of R1 and R2 provide further evidence for weakly bonded K ions in the unheated samples.

The cause of the lack of K clusters observed in the heated sample might also be associated with different Si/Al distributions in the samples. Prior NMR, neutron and X-ray scattering experiments all suggest that there is negligible structural changes in Si and Al coordination in geopolymers heated to 200°C or less [4, 8, 70, 101], so observing different Si/Al distributions in the APT would suggest differences in the sample composition simply due to variability in the microstructure. To address this, the histogram of Si/Al ratios for all of the voxelized datasets is shown in Fig. 4.9. As discussed in a prior publication [91], the Si/Al ratio varies between 1-30 as there may be regions of higher Al concentration agglomerated by a Si rich phase. The gradient between these possible phases is represented here in the histogram of Fig. 4.9. The broad peak frequencies of Si/Al of the samples all fall between 4-10 indicating some diversity between the samples. However, no appreciable trend is observed between the heated and unheated samples in the Si/Al histograms.

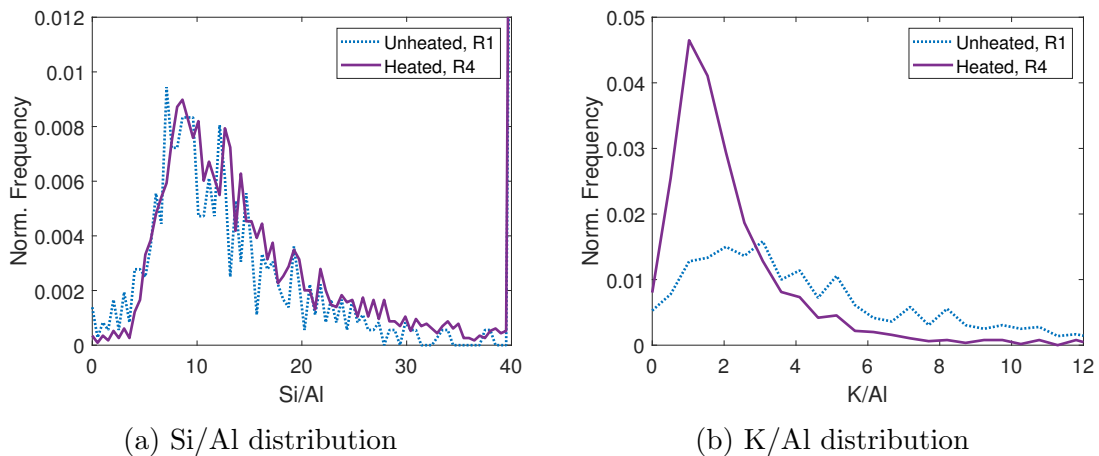
The similarity of Si/Al distributions in the heated and unheated samples is quite clear when comparing runs R1 and R4, which were performed on the same FIB extracted sample. The histograms of Si/Al and K/Al for R1 and R4 are shown in Fig. 4.10 to highlight their comparison. The alignment of Si/Al histograms for R1 and R4 indicates that the recovery of the sample after heat treatment successfully minimized the composition variability. With the Si/Al distribution remaining relatively constant between

these runs, the notable shift in the K/Al histogram of Fig. 4.10 is likely due to the heating procedure.



(a) Si/Al distribution

Figure 4.9: Histograms of K and Al concentrations throughout samples with a 3 nm voxel size.



(a) Si/Al distribution

(b) K/Al distribution

Figure 4.10: Histograms of K and Al concentrations throughout samples with a 3 nm voxel size.

Even with the other samples of varying Si/Al content, the dissipation of excess K clusters is consistent. This phenomenon can be explained by considering that outside of the high vacuum LEAP environment, the observed K clusters would likely be in a hydrated state [73]. These clusters would effectively represent the chemically bound water content of the geopolymer gel product (i.e. K-A-S-H) [8]. Upon heating to 200°C, the

water chemically bound in the form of KOH evaporates [8]. The evaporation process leads to percolation of the highly alkaline solution towards the surface of the material.

This would correspond to the migration of hydrated K ions towards the exterior of the APT specimens. Unfortunately, it was necessary to remove the exterior of the specimens during the re-polishing process in preparation for the post-heat APT tests. This loss of K ions during heating and re-polishing corroborates with the consistent reduction in overall K content between the unheated and heated samples (Tables 4.2).

The results of APT before and after heating to 200°C suggest that the heating process leads to the percolation of entrapped chemically bound water towards the surface of the material along with the excess K ions. This would increase the leachable alkali content of FGP samples exposed to 200°C.

Table 4.2: Count of ranged ions in each APT sample run with multi-atomic ions decomposed.

Element	R1		R2		R3		R4		R5		R6	
	Count	%	Count	%	Count	%	Count	%	Count	%	Count	%
H	61076	23.84%	85448	14.06%	61076	23.84%	109213	11.01%	65199	12.42%	94608	15.10%
Si	44359	17.32%	153420	25.25%	44359	17.32%	412283	41.57%	154607	29.46%	162772	25.98%
O	80978	31.61%	240894	39.64%	80978	31.61%	334955	33.77%	239408	45.62%	255954	40.85%
K	16408	6.41%	48793	8.03%	16408	6.41%	24403	2.46%	11937	2.27%	28878	4.61%
Ga	1867	0.73%	2773	0.46%	1867	0.73%	3095	0.31%	4653	0.89%	1059	0.17%
Al	8644	3.37%	37010	6.09%	8644	3.37%	44753	4.51%	26891	5.12%	40741	6.50%
Fe	620	0.24%	4389	0.72%	620	0.24%	7804	0.79%	3205	0.61%	2459	0.39%
Mg	753	0.29%	1950	0.32%	753	0.29%	3165	0.32%	1534	0.29%	2316	0.37%
C	29175	11.39%	21202	3.49%	29175	11.39%	30209	3.05%	10513	2.00%	29617	4.73%
Ca	3805	1.49%	4717	0.78%	3805	1.49%	10653	1.07%	4363	0.83%	5758	0.92%
Na	1007	0.39%	5116	0.84%	1007	0.39%	1681	0.17%	1640	0.31%	1779	0.28%

### 4.3.2 Free alkalinity

The espresso leaching procedure was used to quantify the free alkalinity of the FGP after exposure to various temperatures 200°C and higher. Here, free alkalinity is defined as that which is readily leachable (as in Ch. 3), not to be confused with the weakly bonded or disordered K [27] that may still be encapsulated in the nanostructure of the material according to APT. Fig. 4.11 shows the results of these leaching tests.

The exposure to 200°C significantly increases the free alkali content relative to the

FGP dried at 60°C (for consistency). This corroborates with the theory from APT that the drying of chemically bound water can lead to percolation of free alkalis, effectively increasing the leachable free alkali content. Furthermore, this agreement with the APT data supports the use of the espresso method since it does not seem to leach the excess K ions that are entrapped in the nanostructure as seen in APT and proposed in literature [61].

Temperatures well above 200°C are known to cause structural reorganization of Si and Al tetrahedra in the geopolymer matrix [8, 101]. These structural changes likely facilitate increased distribution and incorporation of K in the FGP rather than percolation since the samples were immediately immersed in the temperatures well above 200°C. The free alkalinity continually decreased for temperatures 400°C-1000°C, as the FGP gained structural order. The results of this experiment replicate and verify the findings from similar FGP leaching experiments performed by Skvara et al. [78].

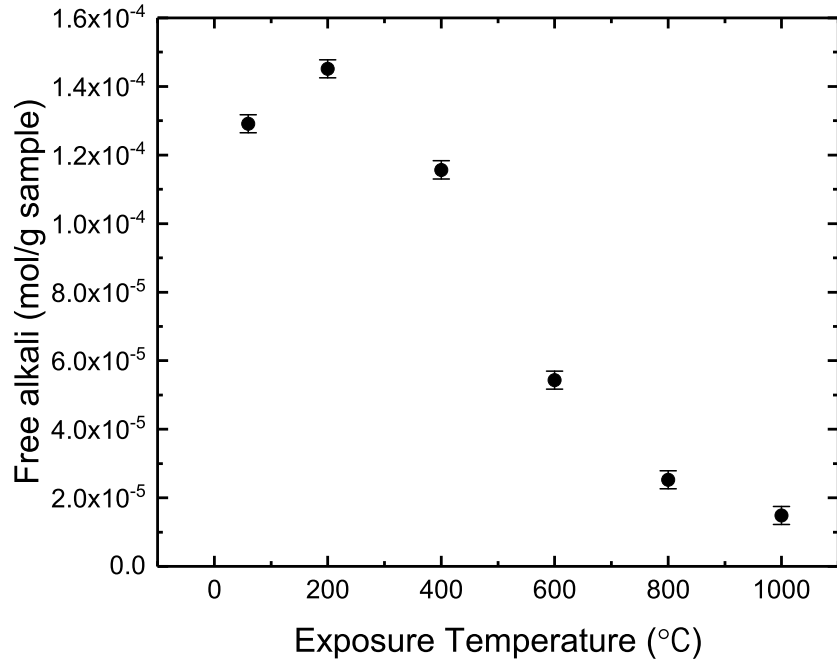


Figure 4.11: Free alkali content of the FGP after various temperature exposures. Error bars denote standard deviation of the method.

### 4.3.3 Nanoindentation

While APT and complimentary leaching experiments both suggest that chemical transformations take place in the geopolymer nanostructure upon heating, the associated effect on mechanical properties is unknown. Nanoindentation was employed to assess the effect of elevated temperatures on the micromechanical properties of the material. Grid indentation and statistical analysis can allow the properties of independent phases in the microstructure to be decoupled [16]. The most discernible phases present in the FGP microstructure are that of reacted geopolymer gel and unreacted fly ash, both of which were apparent in the optical microscope images of all the grid indent areas (see Appendix B).

Belief-based clustering was performed for the grid indentation data of each sample using a model order of  $k=2$ , corresponding to the two likely phases of unreacted and reacted mediums. The Bayesian information criterion (BIC) values reported for all three datasets suggest that assuming  $k=2$  is a probable assertion, although other model orders may also provide similar or slightly higher likelihood (Fig. 4.12-4.14a). The probability of other model orders being suggested for the GMM could be due to the widespread of data associated with the influence of unreacted fly ash.

Previous nanoindentation studies have noted that there can be pitfalls to using only the BIC value to determine or confirm a model order [88]. To supplement the BIC, a histogram of the experimental data was calculated for each sample using the automatic binning algorithm built in to MATLAB. The algorithm, based on Scott's rule, accounts for the sample size and may effectively "smooth" out any insignificant Gaussian distributions present in the data [75]. The histograms shown in Fig. 4.12-4.14b indicate that there are two main features in all of the data sets, one prominent peak between moduli values of 0-20 and a widespread tailing distribution above 25 GPa. Observations of these two features supports the assignment of  $k=2$ , likely corresponding to unreacted and reacted phases.

Fig. 4.12-4.14 show the k=2 clustering for each dataset, where it can be seen that the algorithm consistently groups data with moduli greater than 25 GPa, which have previously been associated with unreacted or partially reacted fly ash phases [21, 60], separately from the lower values that have previously been reported as reacted phases in geopolymer cements [21, 60]. From this evidence, it can be assumed that the assignment of k=2 corresponds to the broad distinction of unreacted or partially reacted phases and the fully reacted geopolymer gel phase for each sample in this study. This assumption yields a high posterior probability of clusters (Fig. 4.12-4.14d) and appears to agree with distribution of experimental data for all samples.

Table 4.3 summarizes the effective deconvolution of these phases obtained through the clustering algorithm. Cluster 1 is presumed to represent the reacted geopolymer phase with Cluster 2 representing indents influenced by the unreacted material. The mean value of Cluster 1 significantly increases from 8 GPa in the unheated sample to around 17 GPa for the samples heated at 200° in an oven or 650° via flame exposure [71]. However, it is possible that the reported moduli of each indent are influenced by the underlying constituents of the microstructure, especially porosity (Ch. 2).

Table 4.3: Summary of FGP nanoindentation data deconvolution. Mean ( $\mu$ ) and standard deviation ( $\sigma^2$ ) for moduli values reported in GPa.

Sample	Cluster:		1			2		
	Sample size, $N$		$\mu$	$\sigma^2$	$f_J$	$\mu$	$\sigma^2$	$f_J$
Unheated	173		8.30	2.53	0.63	40.76	20.58	0.37
200°C	179		16.84	3.48	0.79	46.74	20.35	0.21
650°C	157		17.07	4.47	0.56	59.38	21.12	0.44

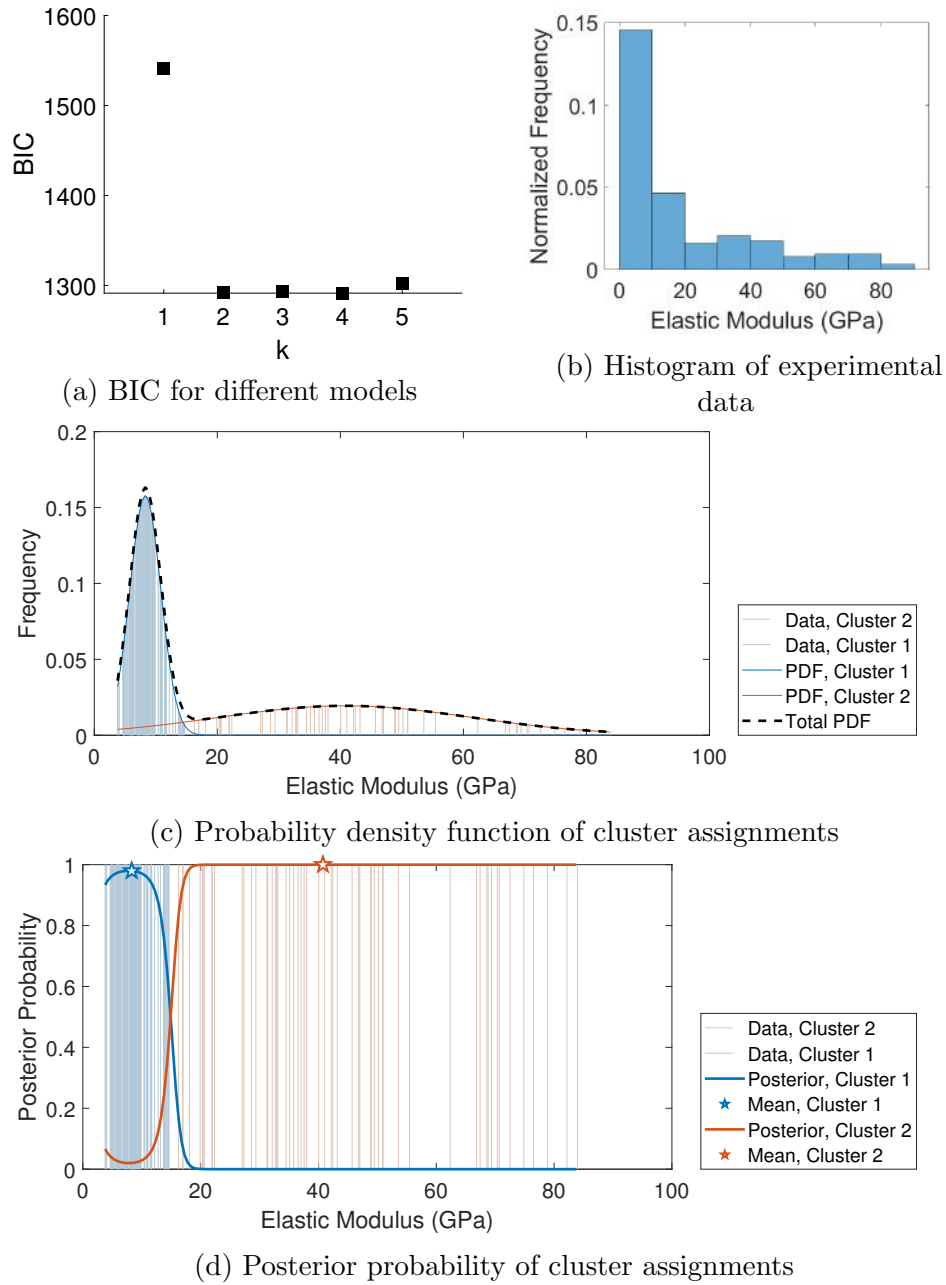


Figure 4.12: Grid indentation data analysis for the as-cast FGP sample. Vertical lines represent individual test results and may appear as solid fill where data are abundant.

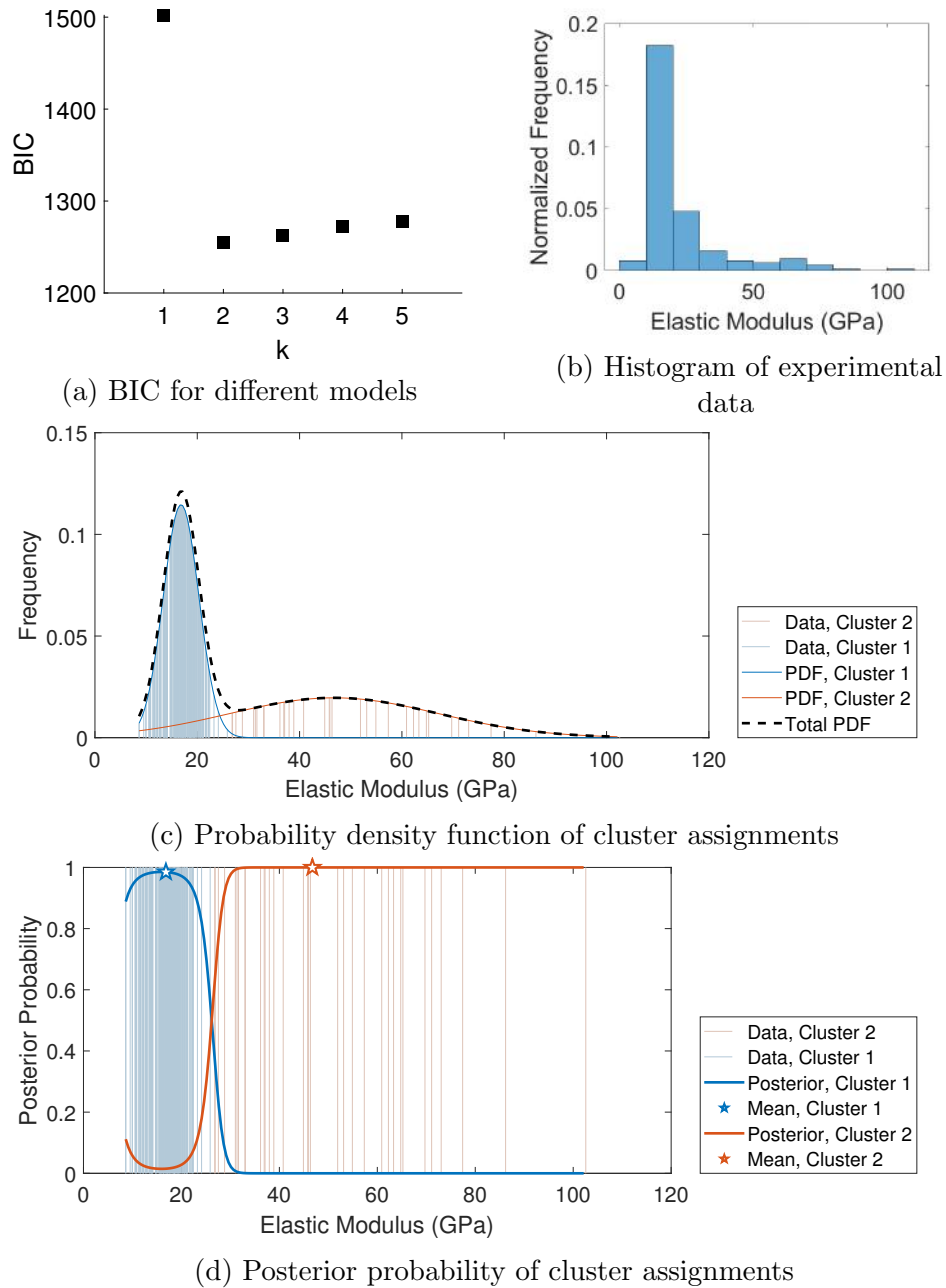


Figure 4.13: Grid indentation data analysis for FGP heated at 200° for 2 hrs. Vertical lines represent individual test results and may appear as solid fill where data are abundant.

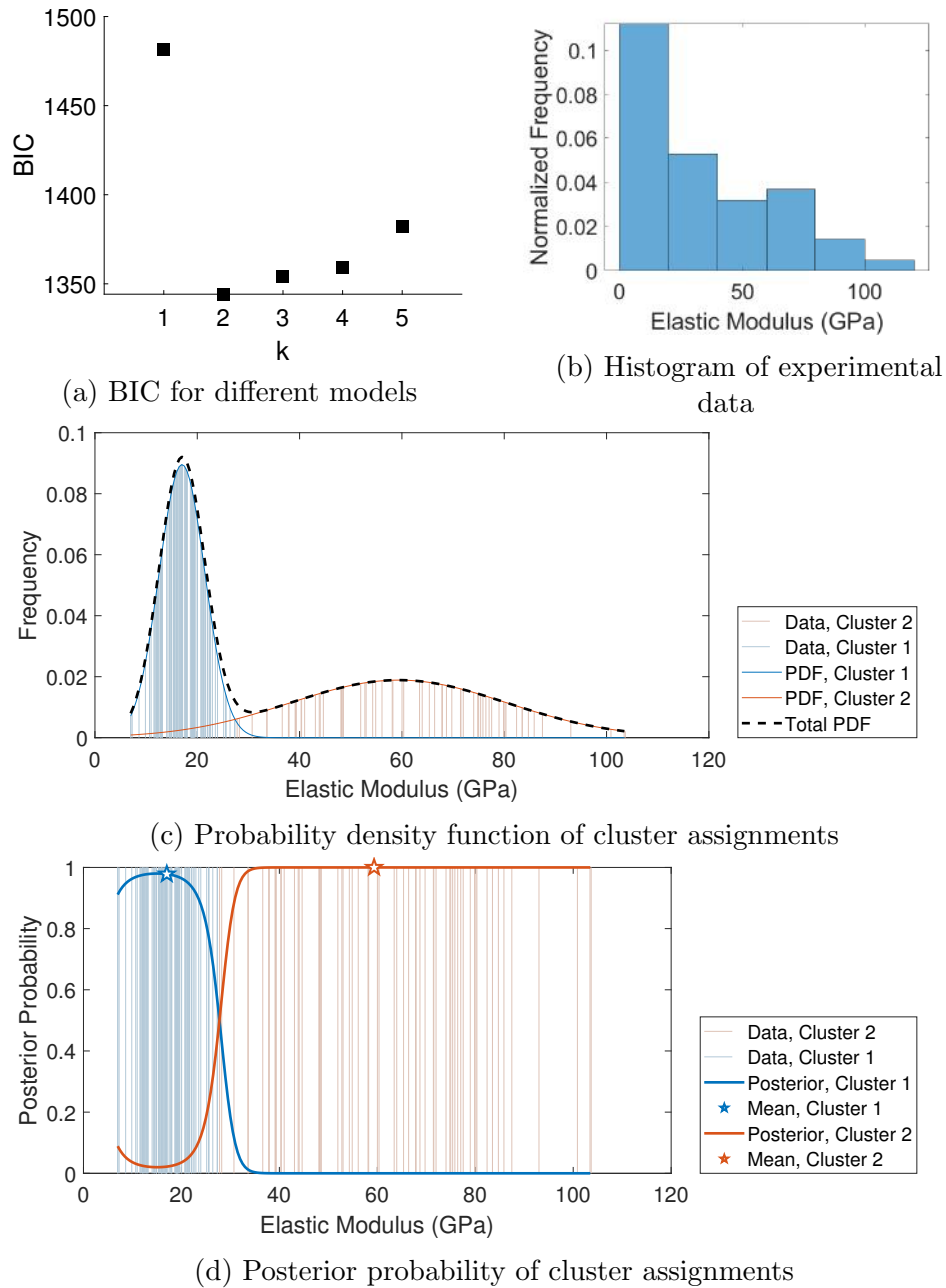


Figure 4.14: Grid indentation data analysis for FGP exposed to flame for 10 minutes as in [71], reaching 650°. Vertical lines represent individual test results and may appear as solid fill where data are abundant.

Fig. 4.15 shows the test data for randomly selected representative indents from the Cluster 1 of each sample. The representative tests suggest that the stiffness measured by CSM indentation is relatively constant in the region of interest between 100 nm and 200 nm, from which the moduli values were averaged, meaning that there is no strong influence of additional structural compliance for the indent and that continuity is generally preserved. Based on the representation of Fig. 4.15, the moduli and hardness values calculated using the continuum analysis of Oliver and Pharr [63] can be assumed to reliably represent the material properties of Cluster 1 more so than the influence of the microstructure (Ch. 2).

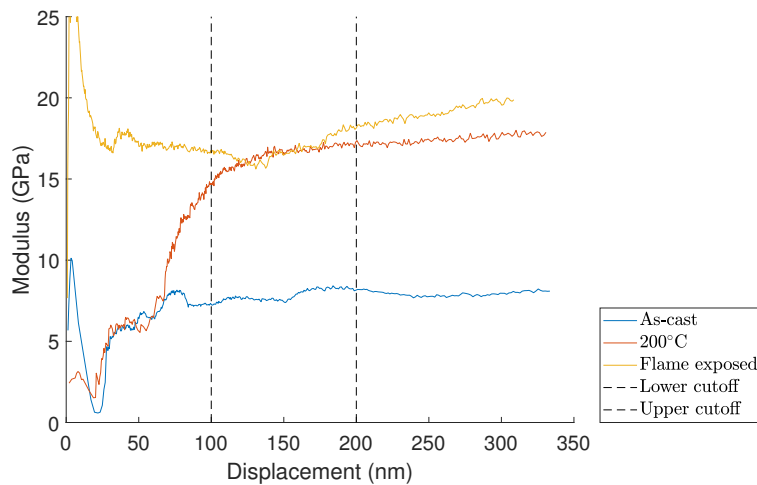


Figure 4.15: Indentation data for randomly selected tests from Cluster 1 (i.e. reacted phase) of each sample.

The increase in the geopolymer gel moduli after heating to 200°C corroborates with the results from Belena et al. [6] who observed the same phenomenon for grid indentation of heat exposed Na-metakaolin geopolymer. Belena et al. hypothesized that this increase was associated with the dehydration of the material. The complementary results from APT and the leaching experiments in the present study support this notion. In a mechanism similar to the effect of saturation on the results of bulk concrete specimens, the presence of chemically bound water in the nanostructure of the FGP may increase internal hydrostatic forces to ultimately reduce the micromechanical response examined by

nanoindentation.

Recent use of advanced NMR techniques by Walkley et al. concluded that alkali ions may not actually be required to charge balance the bridge site of Si-Al tetrahedra [98]. The charge balancing role may be a matter of convenience since such high concentrations of alkalis are often required to dissolve precursor materials in geopolymerization/alkali-activation. As the aluminosilicate precipitates form during the solidification of the geopolymer, it is energetically favorable for the alkali cations to assume a charge balancing role rather than migrate entirely to the pore solution [69]. In addition to the charge balancing ions, excess aqueous alkalis may be enclosed in the aluminosilicate matrix in nanoscale clusters as seen in the APT results of this study, which are supported by the leaching and nanoindentation experiments.

For a better understanding of the structure of these alkaline aluminosilicate materials, the geo“polymer” terminology and “N-A-S-H” and “K-A-S-H” abbreviations should be disregarded. Regarding the role of the alkalis, these materials are more accurately described as an aluminosilicate glass with caged alkali fluxing ions. Excess alkaline solution is confined to small clusters, ultimately promoting the nanoporosity of the material that has been observed in TEM images [7, 91]. This understanding agrees with the model set forth by Rowles et al. (Fig. 4.1) and can help guide further development of these materials. Though, the existing terminologies will likely remain in place for the sake of convenience.

#### 4.4 Conclusions

Novel use of APT before and after heat exposure to 200°C was performed in this study. The evaporation of chemically bound water was found to dissipate clusters of excess K that were previously entrapped in the nanostructure of the aluminosilicate framework. This proposed transformation was supported by the increased alkali leaching observed after exposure to 200°C. Statistical nanoindentation results corroborated with these findings, showing an increase in geopolymer gel strength associated with the dehydration process. Excess alkalis appear to play a detrimental role in the nanostructure of geopolymers. Future research should investigate alternative geopolymer manufacturing techniques to mitigate excess alkalis and chemically bound water in low-Ca geopolymers.

## CHAPTER 5

### EPILOGUE

In Ch. 2, the fundamentals of statistical nanoindentation were revisited. The outcome of this study is a refined method and understanding of the limitations. The results support the later use of statistical nanoindentation in Ch. 4 for fly ash geopolymer samples.

The second study (Ch. 3) proposed a novel framework for formation factor measurement of geopolymers. This could be a helpful tool in the development of geopolymer mix designs and their durability assessment or quality control in the future. The study offers insight into some fundamental aspects of formation factor measurement of portland cement concretes as well. In particular, the method presents a unique approach to estimating pore solution resistivity and accounting for alkali leaching.

The third investigation (Ch. 4) demonstrated the use of atom probe tomography (APT) for analyzing the atomistic morphology of fly ash geopolymer gel before and after heating to 200°C. The results suggested that alkali migration can occur on the nanoscale during dehydration due to the weakly bonded nature of aqueous alkalis. The APT findings were supported by the complimentary use of the free alkali leaching procedure demonstrated for geopolymers in Ch. 3 and a statistical nanoindentation method supported by Ch. 2. Future work based on the APT capabilities demonstrated in this study likely extends beyond the realm of infrastructure materials. APT could help characterize the amorphous structure of bio-compatible cements in the future.

## REFERENCES

- [1] Ali Allahverdi, Mostafa Vafaei, and Hojjatollah Maghsoodloorad. Quality control and assessment of geopolymer cements based on reacted and free alkalis. *Construction and Building Materials*, 153:274–283, 2017.
- [2] Hugues-Yanis Amanieu, Mohammad Aramfard, Daniele Rosato, Leonardo Batista, Ute Rabe, and Doru C. Lupascu. Mechanical properties of commercial  $\text{NiO}$  cathode under different states of charge. *Acta Materialia*, 89:153 – 162, 2015.
- [3] Hugues-Yanis Amanieu, Daniele Rosato, Marco Sebastiani, Federico Massimi, and Doru C Lupascu. Mechanical property measurements of heterogeneous materials by selective nanoindentation: Application to  $\text{NiO}$  cathode. *Materials Science and Engineering: A*, 593:92–102, 2014.
- [4] Valeria F.F. Barbosa and Kenneth J.D. MacKenzie. Synthesis and thermal behaviour of potassium silicate geopolymers. *Materials Letters*, 57(9-10):1477–1482, 2003.
- [5] RS Barneyback Jr and Sidney Diamond. Expression and analysis of pore fluids from hardened cement pastes and mortars. *Cement and Concrete Research*, 11(2):279–285, 1981.
- [6] I Belena and W Zhu. Nanoindentation Study of Na-Geopolymers Exposed to High Temperatures. *Nanotechnology in Construction 3, Proceedings*, pages 169–174, 2009.
- [7] Jonathan L. Bell, Patrick E. Driemeyer, and Waltraud M. Kriven. Formation of Ceramics from Metakaolin-Based Geopolymers. Part II: K-Based Geopolymer. *Journal of the American Ceramic Society*, 92(3):607–615, mar 2009.
- [8] Jonathan L Bell, Pankaj Sarin, Patrick E Driemeyer, Ryan P Haggerty, Peter J Chupas, and Waltraud M Kriven. X-Ray pair distribution function analysis of a metakaolin-based,  $\text{KAlSi}_2\text{O}_6 \cdot 5.5\text{H}_2\text{O}$  inorganic polymer (geopolymer). *J. Mater. Chem.*, 18(48):5974–5981, 2008.

- [9] Dale P Bentz. Three-dimensional computer simulation of portland cement hydration and microstructure development. *Journal of the American Ceramic Society*, 80(1):3–21, 1997.
- [10] Przemyslaw Biecek, Ewa Szczurek, Martin Vingron, Jerzy Tiuryn, et al. The r package bgmm: mixture modeling with uncertain knowledge. *Journal of Statistical Software*, 47(i03), 2012.
- [11] CA Botero, Emilio Jimenez-Piqué, R Martín, Tushar Kulkarni, Vinod K Sarin, and L Llanes. Nanoindentation and nanoscratch properties of mullite-based environmental barrier coatings: Influence of chemical composition—al/si ratio. *Surface and Coatings Technology*, 239:49–57, 2014.
- [12] Yiwen Bu and Jason Weiss. The influence of alkali content on the electrical resistivity and transport properties of cementitious materials. *Cement and Concrete Composites*, 51:49–58, aug 2014.
- [13] H Buckle, JH Westbrook, and H Conrad. The science of hardness testing and its research applications. *American Society for Metals*, pages 453–491, 1973.
- [14] Jeffrey J Chen, Luca Sorelli, Matthieu Vandamme, Franz-Josef Ulm, and Gilles Chanvillard. A coupled nanoindentation/sem-edx study on low water/cement ratio portland cement paste: evidence for c–s–h/ca (oh) 2 nanocomposites. *Journal of the American Ceramic Society*, 93(5):1484–1493, 2010.
- [15] Georgios Constantinides. *Invariant mechanical properties of calcium-silicate-hydrates (CHS) in cement-based materials: instrumented nanoindentation and microporomechanical modeling*. PhD thesis, Massachusetts Institute of Technology, 2006.
- [16] Georgios Constantinides, KS Ravi Chandran, F-J Ulm, and KJ Van Vliet. Grid indentation analysis of composite microstructure and mechanics: Principles and validation. *Materials Science and Engineering: A*, 430(1-2):189–202, 2006.
- [17] Georgios Constantinides, F-J Ulm, and Krystyn Van Vliet. On the use of nanoindentation for cementitious materials. *Materials and structures*, 36(3):191–196, 2003.
- [18] Georgios Constantinides and Franz-Josef Ulm. The nanogranular nature of c–s–h. *Journal of the Mechanics and Physics of Solids*, 55(1):64–90, 2007.

- [19] AR Cooper Jr and LE Eaton. Compaction behavior of several ceramic powders. *Journal of the American Ceramic Society*, 45(3):97–101, 1962.
- [20] Alex T Coyle, Robert P Spragg, Prannoy Suraneni, Armen N Amirkhanian, and William J Weiss. Comparison of Linear Temperature Corrections and Activation Energy Temperature Corrections for Electrical Resistivity Measurements of Concrete. *Advances in Civil Engineering Materials*, 7(1):20170135, 2018.
- [21] Sumanta Das, Pu Yang, Sudhanshu S Singh, James CE Mertens, Xianghui Xiao, Nikhilesh Chawla, and Narayanan Neithalath. Effective properties of a fly ash geopolymer: Synergistic application of x-ray synchrotron tomography, nanoindentation, and homogenization models. *Cement and Concrete Research*, 78:252–262, 2015.
- [22] J Davidovits. Geopolymers. *Journal of Thermal Analysis*, 37(8):1633–1656, 1991.
- [23] D Davydov, M Jirásek, and L Kopecký. Critical aspects of nano-indentation technique in application to hardened cement paste. *Cement and Concrete Research*, 41(1):20–29, 2011.
- [24] Donald J DeCoste, Steven S Zumdahl, and Susan A Zumdahl. Chemistry (ap edition), 2017.
- [25] D Dimas, I. Giannopoulou, and D. Papias. Polymerization in sodium silicate solutions: A fundamental process in geopolymerization technology. *Journal of Materials Science*, 44(14):3719–3730, 2009.
- [26] P. Duxson, A. Fernández-Jiménez, J. L. Provis, G. C. Lukey, A. Palomo, and J. S J Van Deventer. Geopolymer technology: The current state of the art. *Journal of Materials Science*, 42(9):2917–2933, 2007.
- [27] P. Duxson, J. L. Provis, G. C. Lukey, J. S.J. Van Deventer, F. Separovic, and Z. H. Gan. <sup>39</sup>K NMR of free potassium in geopolymers. *Industrial and Engineering Chemistry Research*, 45(26):9208–9210, 2006.
- [28] ASTM E2546-15. Standard practice for instrumented indentation testing. Technical report, ASTM, 2015.

- [29] Reinhard X Fischer, Hartmut Schneider, and Martin Schmucker. Crystal structure of al-rich mullite. *American Mineralogist*, 79(9-10):983–990, 1994.
- [30] Benoit Fournier, Leandro Sanchez, José Duchesne, and Steve Goyette. Evaluation of the Available Alkali Content in Concrete Through a Modified Hot-Water Extraction Method. *15th International conference on Alkali aggregate Reaction*, page 10 p., 2016.
- [31] Chris Fraley and Adrian E Raftery. Model-based clustering, discriminant analysis, and density estimation. *Journal of the American statistical Association*, 97(458):611–631, 2002.
- [32] Edward J. Garboczi. Permeability, diffusivity, and microstructural parameters: A critical review. *Cement and Concrete Research*, 1990.
- [33] RJ Gilliam, JW Graydon, DW Kirk, and SJ Thorpe. A review of specific conductivities of potassium hydroxide solutions for various concentrations and temperatures. *International Journal of Hydrogen Energy*, 32(3):359–364, 2007.
- [34] C-J Haecker, EJ Garboczi, JW Bullard, RB Bohn, Z Sun, Surendra P Shah, and T Voigt. Modeling the linear elastic properties of portland cement paste. *Cement and Concrete Research*, 35(10):1948–1960, 2005.
- [35] Andrew Heath, Kevin Paine, and Marcelle McManus. Minimising the global warming potential of clay based geopolymers. *Journal of Cleaner Production*, 78:75–83, 2014.
- [36] Eric D Hintsala, Ude Hangen, and Douglas D Stauffer. High-throughput nanoindentation for statistical and spatial property determination. *JOM*, 70(4):494–503, 2018.
- [37] Chuanlin Hu, Yueyi Gao, Yamei Zhang, and Zongjin Li. Statistical nanoindentation technique in application to hardened cement pastes: influences of material microstructure and analysis method. *Construction and Building Materials*, 113:306–316, 2016.
- [38] Chuanlin Hu, Shun Yao, Fubing Zou, Shuai Nie, Zhichao Liu, and Fazhou Wang. Insights into the influencing factors on the micro-mechanical properties of calcium-silicate-hydrate gel. *Journal of the American Ceramic Society*, 102(4):1942–1952, 2019.

- [39] Joseph E Jakes, Charles R Frihart, James F Beecher, Robert J Moon, and DS Stone. Experimental method to account for structural compliance in nanoindentation measurements. *Journal of Materials Research*, 23(4):1113–1127, 2008.
- [40] DL Joslin and WC Oliver. A new method for analyzing data from continuous depth-sensing microindentation tests. *Journal of Materials Research*, 5(1):123–126, 1990.
- [41] JA Knapp, DM Follstaedt, SM Myers, JC Barbour, and TA Friedmann. Finite-element modeling of nanoindentation. *Journal of Applied Physics*, 85(3):1460–1474, 1999.
- [42] David J. Larson, Ty J. Prosa, Robert M. Ulfig, Brian P. Geiser, and Thomas F. Kelly. *Local Electrode Atom Probe Tomography*. 2013.
- [43] Hassel Ledbetter, Sudook Kim, Davor Balzar, Scott Crudele, and Waltraud Kriven. Elastic properties of mullite. *Journal of the American Ceramic Society*, 81(4):1025–1028, 1998.
- [44] Xiaodong Li and Bharat Bhushan. A review of nanoindentation continuous stiffness measurement technique and its applications. *Materials characterization*, 48(1):11–36, 2002.
- [45] Redmond R Lloyd, John L Provis, and Jannie S J Van Deventer. Microscopy and microanalysis of inorganic polymer cements. 1: Remnant fly ash particles. *Journal of Materials Science*, 44(2):608–619, 2009.
- [46] Redmond R Lloyd, John L Provis, and Jannie S J Van Deventer. Pore solution composition and alkali diffusion in inorganic polymer cement. *Cement and Concrete Research*, 40:1386–1392, 2010.
- [47] Redmond R Lloyd, John L Provis, and Jannie S.J. Van Deventer. Microscopy and microanalysis of inorganic polymer cements. 2: The gel binder. *Journal of Materials Science*, 44(2):620–631, 2009.
- [48] Zhiyu Luo, Wengui Li, Kejin Wang, and Surendra P Shah. Research progress in advanced nanomechanical characterization of cement-based materials. *Cement and Concrete Composites*, 94:277–295, 2018.

- [49] Pietro Lura, Pavel Trtik, and Beat Münch. Validity of recent approaches for statistical nanoindentation of cement pastes. *Cement and Concrete Composites*, 33(4):457–465, 2011.
- [50] Jaroslav Melar, Guillaume Renaudin, Fabrice Leroux, Adeline Hardy-Dessources, Jean-Marie Nedelec, Christine Taviot-Gueho, Elodie Petit, Prune Steins, Arnaud Poulesquen, and Fabien Frizon. The Porous Network and its Interface inside Geopolymers as a Function of Alkali Cation and Aging. *The Journal of Physical Chemistry C*, 119(31):17619–17632, aug 2015.
- [51] Mahalia Miller, Christopher Bobko, Matthieu Vandamme, and Franz-Josef Ulm. Surface roughness criteria for cement paste nanoindentation. *Cement and Concrete Research*, 38(4):467–476, 2008.
- [52] Bing Hui Mo, He Zhu, Xue Min Cui, Yan He, and Si Yu Gong. Effect of curing temperature on geopolymerization of metakaolin-based geopolymers. *Applied Clay Science*, 99:144–148, 2014.
- [53] Paramita Mondal, Surendra P Shah, and Laurence Marks. A reliable technique to determine the local mechanical properties at the nanoscale for cementitious materials. *Cement and Concrete Research*, 37(10):1440–1444, 2007.
- [54] Mehdi Khanzadeh Moradillo, Chunyu Qiao, Burkan Isgor, Steven Reese, and W. Jason Weiss. Relating Formation Factor of Concrete to Water Absorption. *ACI Materials Journal*, (115), 2018.
- [55] Robert D Moser, Paul G Allison, and Mei Qiang Chandler. Characterization of impact damage in ultra-high performance concrete using spatially correlated nanoindentation/sem/edx. *Journal of materials engineering and performance*, 22(12):3902–3908, 2013.
- [56] Muhammad Zeeshan Mughal, Riccardo Moscatelli, Hugues-Yanis Amanieu, and Marco Sebastiani. Effect of lithiation on micro-scale fracture toughness of  $\text{Li}_x\text{Mn}_2\text{O}_4$  cathode. *Scripta Materialia*, 116:62–66, 2016.
- [57] Muhammad Zeeshan Mughal, Riccardo Moscatelli, and Marco Sebastiani. Load displacement and high speed nanoindentation data set at different state of charge (soc) for spinel  $\text{Li}_x\text{Mn}_2\text{O}_4$  cathodes. *Data in brief*, 8:203–206, 2016.

- [58] Narayanan Neithalath, Jason Weiss, and Jan Olek. Characterizing Enhanced Porosity Concrete using electrical impedance to predict acoustic and hydraulic performance. 2006.
- [59] Jiří Němeček, Vlastimil Králík, and Jaroslav Vondřejc. Micromechanical analysis of heterogeneous structural materials. *Cement and Concrete Composites*, 36:85–92, 2013.
- [60] Jiří Němeček, Vít Šmilauer, and Lubomír Kopecký. Nanoindentation characteristics of alkali-activated aluminosilicate materials. *Cement and Concrete Composites*, 33(2):163–170, 2011.
- [61] Anh Duong Nguyen and František Škvára. The influence of ambient pH on fly ash-based geopolymer. *Cement and Concrete Composites*, 72:275–283, 2016.
- [62] Amin Noushini and Arnaud Castel. The effect of heat-curing on transport properties of low-calcium fly ash-based geopolymer concrete. *Construction and Building Materials*, 112:464–477, 2016.
- [63] Warren Carl Oliver and George Mathews Pharr. An improved technique for determining hardness and elastic modulus using load and displacement sensing indentation experiments. *Journal of materials research*, 7(6):1564–1583, 1992.
- [64] Jorge Osio-Norgaard, Juan Pablo Gevaudan, and Wil V Srubar III. A review of chloride transport in alkali-activated cement paste, mortar, and concrete. *Construction and Building Materials*, 186:191–206, 2018.
- [65] Willi Pabst and EVA Gregorová. Elastic properties of silica polymorphs—a review. *Ceramics-Silikaty*, 57(3):167–184, 2013.
- [66] Sungwoo Park and Mohammad Pour-Ghaz. What is the role of water in the geopolymerization of metakaolin? *Construction and Building Materials*, 182:360–370, 2018.
- [67] G. Plusquellec, M. R. Geiker, J. Lindgård, J. Duchesne, B. Fournier, and K. De Weerd. Determination of the pH and the free alkali metal content in the pore solution of concrete: Review and experimental comparison. *Cement and Concrete Research*, 96:13–26, jun 2017.

- [68] Raphaëlle Pouhet and Martin Cyr. Carbonation in the pore solution of metakaolin-based geopolymer. *Cement and Concrete Research*, 88:227–235, 2016.
- [69] John L Provis. Geopolymers and other alkali activated materials: why, how, and what? *Materials and Structures*, 47(1-2):11–25, 2014.
- [70] Hubert Rahier, Jan Wastiels, Monique Biesemans, Rudolph Willem, Guy Van Assche, and Bruno Van Mele. Reaction mechanism, kinetics and high temperature transformations of geopolymers. *Journal of Materials Science*, 42(9):2982–2996, 2007.
- [71] O. G. Rivera, W. R. Long, C. A. Weiss, R. D. Moser, B. A. Williams, K. Torres-Cancel, E. R. Gore, and P. G. Allison. Effect of elevated temperature on alkali-activated geopolymeric binders compared to portland cement-based binders. *Cement and Concrete Research*, 90:43–51, 2016.
- [72] Pavel Rovnaník. Effect of curing temperature on the development of hard structure of metakaolin-based geopolymer. 2010.
- [73] M. R. Rowles, John V. Hanna, K. J. Pike, M. E. Smith, and B. H. O’Connor.  $^{29}\text{Si}$ ,  $^{27}\text{Al}$ ,  $^1\text{H}$  and  $^{23}\text{Na}$  MAS NMR study of the bonding character in aluminosilicate inorganic polymers. *Applied Magnetic Resonance*, 32(4):663–689, 2007.
- [74] Gideon Schwarz et al. Estimating the dimension of a model. *The annals of statistics*, 6(2):461–464, 1978.
- [75] David W Scott. On optimal and data-based histograms. *Biometrika*, 66(3):605–610, 1979.
- [76] M Sebastiani, R Moscatelli, F Ridi, P Baglioni, and F Carassiti. High-resolution high-speed nanoindentation mapping of cement pastes: unravelling the effect of microstructure on the mechanical properties of hydrated phases. *Materials & Design*, 97:372–380, 2016.
- [77] V. V. Shcherbakov and Yu. M. Artemkina. Electrical conductivity in alkali metal hydroxide-water systems. *Russian Journal of Inorganic Chemistry*, 55(6):967–969, 2010.

- [78] František Škvára, Lubomír Kopecký, Lenka Myšková, V. Í T Šmilauer, Lucie Alberovská, and Lenka Vinšová. Aluminosilicate polymers - Influence of elevated temperatures, efflorescence. *Ceramics - Silikaty*, 53(4):276–282, 2009.
- [79] František Škvára, Vít Šmilauer, Petr Hlaváček, Lubomír Kopecký, and Zuzana Cílová. A weak alkali bond in (N, K)-A-S-H gels: Evidence from leaching and modeling. *Ceramics - Silikaty*, 56(4):374–382, 2012.
- [80] K A Snyder, X Feng, B D Keen, and T O Mason. Estimating the electrical conductivity of cement paste pore solutions from OH-, K+and Na+concentrations. *Cement and Concrete Research*, 33(6):793–798, 2003.
- [81] Kenneth A Snyder. The relationship between the formation factor and the diffusion coefficient of porous materials saturated with concentrated electrolytes: Theoretical and experimental considerations. *Concrete Science and Engineering*, 3(9):216–224, 2001.
- [82] R. Spragg, S. Jones, Y. Bu, Y. Lu, D. Bentz, K. Snyder, and J. Weiss. Leaching of conductive species: Implications to measurements of electrical resistivity. *Cement and Concrete Composites*, 2017.
- [83] Robert Spragg, Chiara Villani, Ken Snyder, Dale Bentz, Jeffrey Bullard, and Jason Weiss. Factors That Influence Electrical Resistivity Measurements in Cementitious Systems. *Transportation Research Record: Journal of the Transportation Research Board*, 2342(2342):90–98, 2013.
- [84] Robert Paul Spragg. *DEVELOPMENT OF PERFORMANCE RELATED SPECIFICATIONS THAT INCLUDE FORMATION FACTOR*. PhD thesis, Purdue University, 2017.
- [85] DS Stone, KB Yoder, and WD Sproul. Hardness and elastic modulus of tin based on continuous indentation technique and new correlation. *Journal of Vacuum Science & Technology A: Vacuum, Surfaces, and Films*, 9(4):2543–2547, 1991.
- [86] KK Strelov and ID Kashcheev. Phase diagram of the system al<sub>2</sub>o<sub>3</sub>-sio<sub>2</sub>. *Refractories*, 36(8):244–246, 1995.
- [87] Paul D Tennis and Hamlin M Jennings. A model for two types of calcium silicate hydrate in the microstructure of portland cement pastes. *Cement and concrete research*, 30(6):855–863, 2000.

- [88] RJ Thomas, Berhan Seium Gebregziabiher, Adom Giffin, and Sulapha Peethamparan. Micromechanical properties of alkali-activated slag cement binders. *Cement and Concrete Composites*, 90:241–256, 2018.
- [89] K Thompson, D Lawrence, D J Larson, J D Olson, T F Kelly, and B Gorman. In situ site-specific specimen preparation for atom probe tomography. *Ultramicroscopy*, 107(2-3):131–139, 2007.
- [90] Pavel Trtik, Beat Münch, and Pietro Lura. A critical examination of statistical nanoindentation on model materials and hardened cement pastes based on virtual experiments. *Cement and Concrete Composites*, 31(10):705–714, 2009.
- [91] Atolo Tuinukuafe, Tyler Kaub, Charles A Weiss Jr, Paul G Allison, Gregory B Thompson, and Armen Amirkhonian. Atom probe tomography of an alkali activated fly ash concrete. *Cement and Concrete Research*, 121:37–41, 2019.
- [92] Kai tuo Wang, Patrick N Lemougna, Qing Tang, Wei Li, and Xue min Cui. Lunar regolith can allow the synthesis of cement materials with near-zero water consumption. *Gondwana Research*, 44:1–6, 2017.
- [93] Franz-Josef Ulm, Matthieu Vandamme, Chris Bobko, Jose Alberto Ortega, Kuangshin Tai, and Christine Ortiz. Statistical indentation techniques for hydrated nanocomposites: concrete, bone, and shale. *Journal of the American Ceramic Society*, 90(9):2677–2692, 2007.
- [94] Franz-Josef Ulm, Matthieu Vandamme, Hamlin M Jennings, James Vanzo, Michelle Bentivegna, Konrad J Krakowiak, Georgios Constantinides, Christopher P Bobko, and Krystyn J Van Vliet. Does microstructure matter for statistical nanoindentation techniques? *Cement and Concrete Composites*, 32(1):92–99, 2010.
- [95] Jannie S J Van Deventer, John L Provis, and Peter Duxson. Technical and commercial progress in the adoption of geopolymers. *Minerals Engineering*, 29:89–104, 2012.
- [96] Karine Velez, Sandrine Maximilien, Denis Damidot, Gilbert Fantozzi, and Francois Sorrentino. Determination by nanoindentation of elastic modulus and hardness of pure constituents of Portland cement clinker. *Cement and Concrete Research*, 31(4):555–561, 2001.

- [97] Maritza GJ Veprek-Heijman and Stan Veprek. The deformation of the substrate during indentation into superhard coatings: Bückle’s rule revised. *Surface and Coatings Technology*, 284:206–214, 2015.
- [98] B Walkley and J L Provis. Molecular structure of alkali-activated cements as determined by solid state  $^{27}\text{Al}$  and  $^{23}\text{Na}$  MQMAS NMR. In *37th Cement and Concrete Science Conference*, number April 2018, 2017.
- [99] W Jason Weiss, Robert P Spragg, O Burkan Isgor, M Tyler Ley, and Thomas Van Dam. Toward Performance Specifications for Concrete: Linking Resistivity, RCPT and Diffusion Predictions Using the Formation Factor for Use in Specification. In *High Tech Concrete: Where Technology and Engineering Meet*, volume 1. 2018.
- [100] Claire E. White, John L. Provis, Anna Llobet, Thomas Proffen, and Jannie S. J. van Deventer. Evolution of Local Structure in Geopolymer Gels: An In Situ Neutron Pair Distribution Function Analysis. *Journal of the American Ceramic Society*, 94(10):3532–3539, oct 2011.
- [101] Claire E. White, John L. Provis, Thomas Proffen, and Jannie S.J. Van Deventerz. The effects of temperature on the local structure of metakaolin-based geopolymer binder: A neutron pair distribution function investigation. *Journal of the American Ceramic Society*, 93(10):3486–3492, oct 2010.
- [102] William Wilson, Luca Sorelli, and Arezki Tagnit-Hamou. Automated coupling of nanoindentation and quantitative energy-dispersive spectroscopy (ni-qeds): A comprehensive method to disclose the micro-chemo-mechanical properties of cement pastes. *Cement and Concrete Research*, 103:49–65, 2018.
- [103] Fan Zhang, Liying Zhang, Ming Liu, Chenzhong Mu, Yen Nan Liang, and Xiao Hu. Role of alkali cation in compressive strength of metakaolin based geopolymers. *Ceramics International*, 43(4):3811–3817, 2017.
- [104] Zuhua Zhang, John L. Provis, Xue Ma, Andrew Reid, and Hao Wang. Efflorescence and subflorescence induced microstructural and mechanical evolution in fly ash-based geopolymers. *Cement and Concrete Composites*, 92:165–177, sep 2018.
- [105] Zuhua Zhang, John L Provis, Andrew Reid, and Hao Wang. Fly ash-based geopolymers: The relationship between composition, pore structure and efflorescence. *Cement and Concrete Research*, 64:30–41, 2014.

- [106] Wenzhong Zhu, John J Hughes, Nenad Bicanic, and Chris J Pearce.  
Nanoindentation mapping of mechanical properties of cement paste and natural rocks. *Materials characterization*, 58(11-12):1189–1198, 2007.

## APPENDIX A

### CODE FOR INDENTATION DATA ANALYSIS

```
1 %% Import NI data from spreadsheet
2
3 clear all;
4 close all;
5 clc;
6
7 %formatted for excel file output from NanoSuite (Agilent)
8
9 %not very efficient, may take ~15min for 400 tests(sheets) on avg. laptop
10
11 %make sure there are NO unwanted sheets
12 %(i.e. blank "Sheet 1"- usually first sheet:P)
13 % SERIOUSLY, DELETE "SHEET 1" in the Excel file
14
15 % also double check that the output is correct
16 %% import entire file as cell
17 [~,sheet_name]=xlsfinfo('C:\Users\atolo\Desktop\NI matlab\AAFA csm grid1.xlsx');
18 for k=1:numel(sheet_name)
19
20     data{k}=xlsread('C:\Users\atolo\Desktop\NI matlab\AAFA csm grid1.xlsx',sheet_name{k})
21
22     % fill tagged tests with tasty NaN
23     empties = cellfun('isempty',data);
```

```

24     data(empties) = {[NaN NaN NaN NaN NaN NaN]};
25 end
26
27 %% Create cells for desired variables from each test
28 %make cells for displacement, stiffness, load, modulus and hardness from
29 %each indentation test
30
31 numtests = numel(sheet_name)-3; %excludes three summary sheets
32 d = cell(1,numtests); %disp
33 l = cell(1,numtests); %load
34 s = cell(1,numtests); %stiffness
35 H = cell(1,numtests); %hardness
36 M = cell(1,numtests); %e modulus
37
38
39     for k=4:numel(sheet_name)
40
41         d{k} = data{1,k}(:,1);
42         d=d(~cellfun('isempty',d)); % removes non-test tabs
43
44         l{k} = data{1,k}(:,2);
45         l=l(~cellfun('isempty',l));
46
47         s{k} = data{1,k}(:,4);
48         s=s(~cellfun('isempty',s));
49
50         H{k} = data{1,k}(:,5);
51         H=H(~cellfun('isempty',H));
52
53         M{k} = data{1,k}(:,6);
54         M=M(~cellfun('isempty',M));
55     end
56

```

```

57  %% output workspace for decon
58
59  save AAFA1.mat d l s H M numtests
60
61  %% Nanoindentation continuity filter
62
63  % this script preprocesses grid indentation data for statistical decon
64  % similar to the procedure from Amanieu et al. 2014
65
66  clear all;
67  close all;
68  clc;
69
70  %% Import the data
71
72  filename = 'AAFA200_' %ouput will use this
73
74  load 'AAFA200.mat'
75
76  %% Filter Phase 1 – Self-similarity
77
78  % Check lineairity of L vs. h^2 for old times sake
79  % More efficient than parabolic approach from Amanieu
80
81  % make new cells for filtered results
82  d1 = cell(1,numtests); %disp
83  l1 = cell(1,numtests); %load
84  s1 = cell(1,numtests); %stiffness
85  H1 = cell(1,numtests); %hardness
86  M1 = cell(1,numtests); %e modulus
87
88  for k = 1:numtests
89

```

```

90 D2 = d{k}.^2;
91 y = l{k};
92
93 % regress
94 X = [ones(length(D2),1) D2];
95 b = X\y;
96 ycalc = X*b;
97 % coef of determination
98 Rsq = 1 - sum((y - ycalc).^2)/sum((y - mean(y)).^2);
99
100 %needs to be VERY linear
101 if Rsq>0.996 % but what is linear enough?  \-(o-O)-/
102
103     d1{k} = d{k};
104
105     l1{k} = l{k};
106
107     s1{k} = s{k};
108
109     H1{k} = H{k};
110
111     M1{k} = M{k};
112
113 else
114
115     d1{k} = NaN(length(d{k}),1);
116
117     l1{k} = NaN(length(l{k}),1);
118
119     s1{k} = NaN(length(s{k}),1);
120
121     H1{k} = NaN(length(H{k}),1);
122

```

```

123     M1{k} = NaN(length(M{k}),1);
124
125 end
126
127 end
128
129
130 %% Filter Phase 2 – Structural Compliance, Cs
131
132 % set min and max depth for indexing ROI
133 dMin = 100; % nm, or whatever export units are used
134 dMax = 200; %Note: may need to decrease noise tolerance for larger ranges
135
136 % make new cells for indexed results
137 do = cell(1,numtests); %disp
138 lo = cell(1,numtests); %load
139 so = cell(1,numtests); %stiffness
140 Ho = cell(1,numtests); %hardness
141 Mo = cell(1,numtests); %e modulus
142
143 % make new cells for refiltered results
144 d2 = cell(1,numtests); %disp
145 l2 = cell(1,numtests); %load
146 s2 = cell(1,numtests); %stiffness
147 H2 = cell(1,numtests); %hardness
148 M2 = cell(1,numtests); %e modulus
149
150 lsys = cell(1,numtests);
151 j = cell(1,numtests);
152 Cs = cell(1,numtests); %struct. compliance
153
154 figure;
155 for i = 1:numtests

```

```

156
157     if isnan(d1{i}) % exclude the tagged tests
158
159         d2{i} = NaN;
160
161         l2{i} = NaN;
162
163         s2{i} = NaN;
164
165         H2{i} = NaN;
166
167         M2{i} = NaN;
168
169     else
170
171
172         % index the desired depth range
173         ind = d1{i}>dMin & d{i}<dMax;
174         % extract for each test
175         do{i} = d1{i}(ind);
176         lo{i} = l1{i}(ind);
177         so{i} = s1{i}(ind);
178         Ho{i} = H1{i}(ind);
179         Mo{i} = M1{i}(ind);
180
181         % "SYS" plot axes
182         lsys{i} = (1000*lo{i}).^0.5; %N^1/2
183         j{i} = lsys{i}./so{i};
184
185         % regress
186         Z = [ones(length(lsys{i}),1) lsys{i}];
187         b1 = Z\j{i};
188         ycalc1 = Z*b1;

```

```

189
190     % coef of determination
191     Rsq = 1 - sum((j{i} - ycalcl).^2)/sum((j{i} - mean(j{i})).^2);
192     % slope = compliance
193     Cs{i} = abs(b1(2,1));
194
195     if Cs{i} < 4e-6 % empirically det. from Si by Amanieu
196
197         if Rsq > 0.5 % allow for some noise
198
199             d2{i} = do{i};
200
201             l2{i} = lo{i};
202
203             s2{i} = so{i};
204
205             H2{i} = Ho{i};
206
207             M2{i} = Mo{i};
208
209             % OPTIONAL
210             plot(lsys{i}, j{i})
211             hold on
212
213         else
214
215             d2{i} = NaN;
216
217             l2{i} = NaN;
218
219             s2{i} = NaN;
220
221             H2{i} = NaN;

```

```

222
223         M2{i} = NaN;
224
225     end
226     else
227
228         d2{i} = NaN;
229
230         l2{i} = NaN;
231
232         s2{i} = NaN;
233
234         H2{i} = NaN;
235
236         M2{i} = NaN;
237     end
238 end
239 end
240
241 ylabel('Load^{1/2}/S (m/N^{1/2})')
242 xlabel('Load^{1/2} (N^{1/2})')
243 set(gca, 'FontSize', 14)
244
245 %% Summarize modulus and hardness values for valid tests
246
247
248 for j=1:numtests
249
250     Mf1(j, :) = mean(Mo{j}); %after filter 1
251
252     Hf1(j, :) = mean(Ho{j});
253
254 end

```

```

255
256 for j=1:numtests
257
258     Mf2(j,:) = mean(M2{j}); %after filter 2
259
260     Hf2(j,:) = mean(H2{j});
261
262 end
263
264 %Mf1(337,:) = NaN; % exclude single outlier if necessary
265
266 %% check efficiency
267
268 nnz(~isnan(Mf1))/400
269 nnz(~isnan(Mf1))
270 nnz(~isnan(Mf2))/400
271 nnz(~isnan(Mf2))
272
273 %% output for decon and plotting
274
275 % only M and H for decon
276 file1 = [filename 'MandH.mat'];
277 save(file1, 'Mf1', 'Mf2', 'Hf1', 'Hf2')
278
279 % everything
280 file2 = [filename 'filtered.mat'];
281 save(file2)
282
283 %% count yield
284
285 % nnz(~isnan(vec))
286
287

```

```

288 %% Statistical deconvolution/clustering of NI results
289
290 clear all;
291 close all;
292 clc;
293
294 %% import data for M and/or H
295
296 load AAFA200_MandH.mat
297
298 m = Mf1;
299 % h = Hf1;
300
301 X = m; %pick m and/or h
302
303 filename = 'AAFA200_k2_';
304
305 K = 2; %number of phases/order of model
306 %% GMM Determination
307
308 k = 1:5;
309 nK = numel(k);
310 Sigma = {'full'};
311 nSigma = numel(Sigma);
312 SharedCovariance = {false};
313 SCtext = {'false'};
314 nSC = numel(SharedCovariance);
315 RegularizationValue = 0.01;
316 options = statset('MaxIter',10000);
317
318 % Fit the GMMs using all parameter combination. Compute the AIC and BIC
319 % for each fit. Track the terminal convergence status of each fit.
320

```

```

321 % Preallocation
322 gm = cell(nK,nSigma,nSC);
323 aic = zeros(nK,nSigma,nSC);
324 bic = zeros(nK,nSigma,nSC);
325 converged = false(nK,nSigma,nSC);
326
327 % Fit all models
328 for m = 1:nSC;
329     for j = 1:nSigma;
330         for i = 1:nK;
331             rng(1)
332             gm{i,j,m} = fitgmdist(X,k(i),...
333                 'CovarianceType',Sigma{j},...
334                 'SharedCovariance',SharedCovariance{m},...
335                 'RegularizationValue',RegularizationValue,...
336                 'Options',options);
337             aic(i,j,m) = gm{i,j,m}.AIC;
338             bic(i,j,m) = gm{i,j,m}.BIC;
339             converged(i,j,m) = gm{i,j,m}.Converged;
340         end
341     end
342 end
343
344 allConverge = (sum(converged(:)) == nK*nSigma*nSC)
345
346 % |gm| is a cell array containing all of the fitted |gmdistribution| model
347 % objects.
348 %% BIC Check
349
350 % Plot separate bar charts to compare the AIC and BIC among all fits. Group
351 % the bars by _k_.
352 % figure;
353 % bar(reshape(aic,nK,nSigma*nSC));

```

```

354 % title('AIC For Various $k$ and $\Sigma$ Choices','Interpreter','latex');
355 % xlabel('$k$','Interpreter','Latex');
356 % ylabel('AIC');
357 % legend({'Diagonal-shared','Full-shared','Diagonal-unshared',...
358 %       'Full-unshared'});
359
360 f1=figure;
361
362 Xbic = [1 2 3 4 5];
363
364 sz = 200;
365 scatter(Xbic,bic,sz,'k','s','filled');
366
367 xlabel('k');
368 ylabel('BIC');
369
370 xlim([0 i+1]);
371 xticks(Xbic);
372 xticklabels({'1','2','3','4','5'});
373 set(gca,'FontSize',20)
374
375 % % save fig
376 figname = [filename 'BIC'];
377
378 saveas(f1,[figname '.png']);
379 saveas(f1,[figname '.eps']);
380
381 %% Deconvolution
382
383 % Cluster the training data using the best fitting model.
384
385 % Remember, different crystal orientations may warrant additional
386 % phases/clusters.

```

```

387
388 rng(3);
389 gmBest = gm{K,1,1}; % input correct/desired number of phases in 1st index
390 clusterX = cluster(gmBest,X);
391 kGMM = gmBest.NumComponents;
392 fj = gmBest.ComponentProportion; % "volume fraction"
393
394 x1=cell(1,kGMM);
395 y1=cell(1,kGMM);
396
397 XX = [min(X):0.5:max(X)];
398 Pjo = zeros(1,length(XX));
399
400 f2=figure('Renderer','painters','Position',[1 1 1000 400]);
401 for c=1:kGMM;
402
403 % index clusters
404     ind= clusterX==c;
405     x1{c}=X(ind);
406
407 % theoretical total and phase pdfs
408 dev{c} = sqrt(gmBest.Sigma(:,:,c)); %std deviation
409 mu{c} = gmBest.mu(c,:); %mean
410 % dev{c} = std(x1{c}); %std deviation
411 % mu{c} = mean(x1{c}); %mean
412
413 pij{c} = normpdf(XX,mu{c},dev{c}); % theo. pdf
414 exp{c} = normpdf(x1{c},mu{c},dev{c}); % height for experimental data stems
415
416 % plot pdfs
417 formatspec = "\\mu-{%d}= %.2f, \\sigma -{%d}= %.2f";
418 pdftxt = sprintf(formatspec,c,mu{c},c,dev{c});
419 pi = plot(XX,pij{c},'DisplayName',pdftxt);

```

```

420 hold on
421
422 % include experimental data points
423 morespec = "Experimental Data-{%d}, f_{J}= %.2f";
424 exptxt = sprintf(morespec,c,fj(:,c));
425 Color = pi.Color*0.9 + -0.7*(pi.Color - 1);
426 pu=stem(x1{c},exp{c}, 'Color',Color, 'LineWidth',0.25, 'Marker', 'none', 'DisplayName',exptxt);
427
428 uistack(pu, 'down', c);
429
430 Pj = Pjo + pij{c};
431 Pjo = Pj;
432 end
433
434 % Cumulative pdf
435 cumtxt = ['Total PDF'];
436 cum=plot(XX,Pj, 'k', 'LineWidth',2, 'LineStyle', '--', 'DisplayName', cumtxt);
437 uistack(cum, 'top');
438 xlabel('Elastic Modulus (GPa)');
439 ylabel('Frequency');
440
441 % %the histogrammy goes too
442 % Htxt = ['Experimental histogram'];
443 % bin=histogram(X, 'Normalization', 'probability', 'FaceColor', 'w', 'DisplayName', Htxt)
444 % uistack(bin, 'bottom');
445
446 % ylim([0 0.1]);
447
448 legend show
449 legend('Location', 'southeastoutside')
450 set(gca, 'FontSize', 16)
451
452 % % save fig

```

```

453 figname2 = [filename 'PDF'];
454
455 saveas(f2,figname2, 'png');
456 saveas(f2,figname2, 'epsc');
457
458 %% Posterior probability plot
459
460 XXX = XX(:);
461
462 pij = posterior(gmBest,XXX);
463
464 f3=figure('Renderer', 'painters', 'Position',[1 1 1000 400]);
465 for c=1:kGMM;
466
467 exp{c} = posterior(gmBest,x1{c});
468 uno{c} = posterior(gmBest,mu{c});
469
470 % plot posterior
471 pispec = "Posterior-{"%d}";
472 pitxt = sprintf(pispec,c);
473 pi = plot(XXX,pij(:,c), 'LineWidth',2, 'DisplayName',pitxt);
474 hold on
475
476 % plot exp data
477 morespec2 = "Experimental Data-{"%d"}, f-{"J"}= %.2f";
478 exptxt2 = sprintf(morespec2,c,fj(:,c));
479 Color = pi.Color*0.9 + -0.7*(pi.Color - 1);
480 DATuh=stem(x1{c},ones(length(x1{c}),1), 'Color',Color, 'LineWidth',0.25, 'Marker', 'none', 'Disp
481
482 % plot the mean of the clusters
483 muspec = "\\mu-{"%d"}= %.2f";
484 mutxt =sprintf(muspec,c,mu{c});
485 sz=150;

```

```

486 mustar = scatter(mu{c}, (uno{c}(:,c)),sz, 'p', 'MarkerFaceColor','w', 'MarkerEdgeColor',pi.Col
487 bump=(kGMM-c);
488 drop=2*(c);
489 uistack(DATuh, 'top');
490 uistack(pi, 'up', bump);
491 uistack(mustar, 'up', bump);
492 uistack(DATuh, 'down', drop);
493 end
494
495 %ylim([0.5 1]);
496 xlabel('Elastic Modulus (GPa)');
497 ylabel('Posterior Probability');
498
499 legend show
500 legend('Location', 'southeastoutside')
501 set(gca, 'FontSize', 16)
502
503 % % save fig
504 figname3 = [filename 'Post'];
505
506 saveas(f3, figname3, 'png');
507 saveas(f3, figname3, 'eps');
508
509
510 %% stats
511
512 % MEAN = cell2mat(mu)
513 % STD = cell2mat(dev)
514 % fj
515 %
516 % nnz(~isnan(X))
517
518 %% histogram of exp data

```

```
519
520 f4=figure
521
522 histogram(X,'Normalization','probability')
523
524 % ylim([0 .2]);
525 % xlim([0 100]);
526 xlabel('Elastic Modulus (GPa)');
527 ylabel('Norm. Frequency');
528
529 set(gca,'FontSize',20)
530
531 % save fig
532 figname4 = [filename 'histo'];
533
534 saveas(f4,figname4, 'png');
535 saveas(f4,figname4, 'epsc');
```

## APPENDIX B

### GRID INDENTATION REGIONS OF FLY ASH GEOPOLYMER SAMPLES

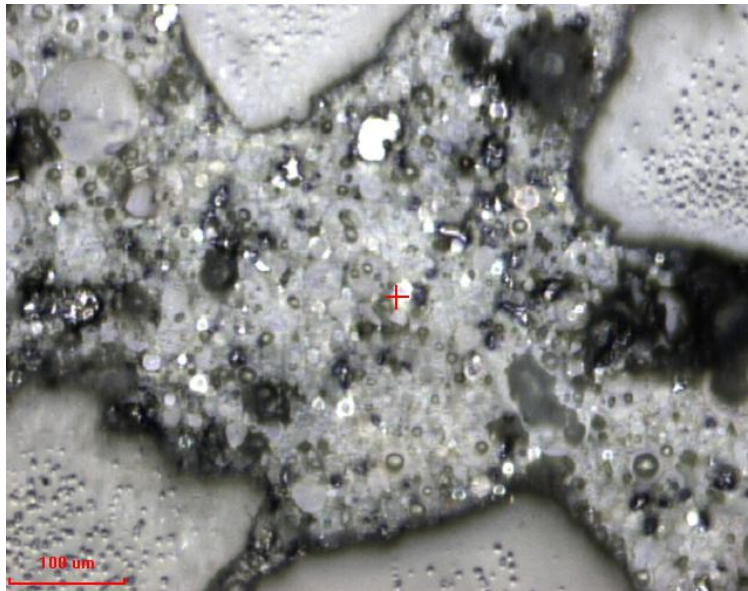


Figure B.1: Grid indentation region of unheated FGP. Cross hair marks center.

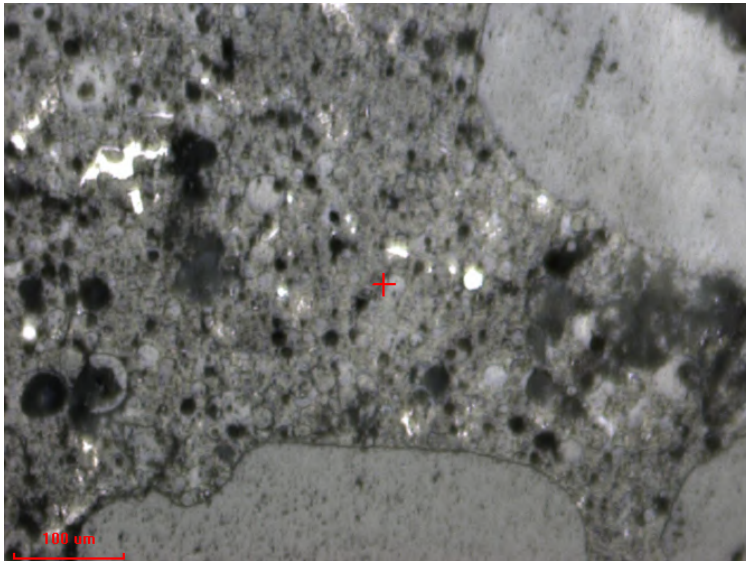


Figure B.2: Grid indentation region of 200°C heated FGP. Cross hair marks center.

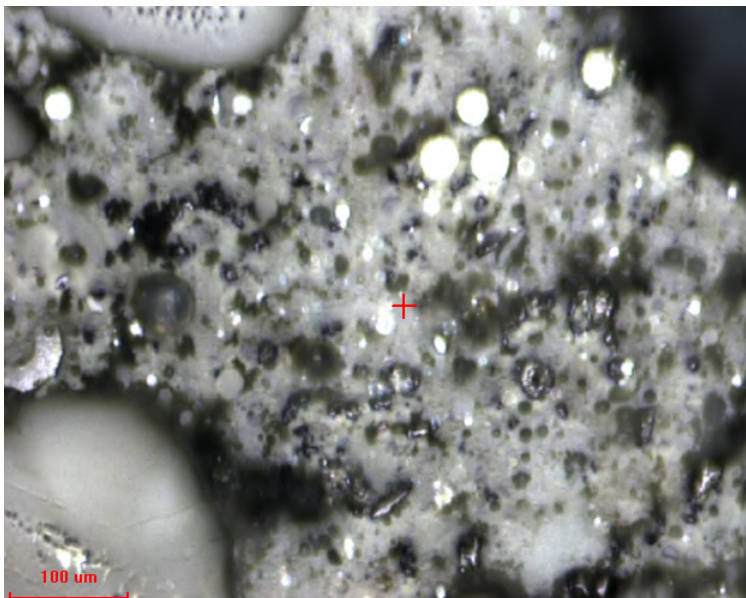


Figure B.3: Grid indentation region of flame heated FGP. Cross hair marks center.